Early whole-body mutant huntingtin lowering averts changes in proteins and lipids important for synapse function and white matter maintenance in the LacQ140 mouse model

Kai Shing[1*], Ellen Sapp[1*], Adel Boudi[1], Sophia Liu[1], Connor Seeley[1], Deanna Marchionini[2], Marian DiFiglia[1], and Kimberly B. Kegel-Gleason[1]

[1]Department of Neurology, Massachusetts General Hospital, Charlestown, MA 02129

[2]CHDI Management/CHDI Foundation, New York, NY 10001

*These authors contributed equally.

Corresponding Author: Kimberly B. Kegel-Gleason

Address: 114 16th Street, Room 2001

MassGeneral Institute for Neurodegeneration (MIND)

Charlestown, MA 02129

Phone: 617-724-8754

Email: kkegelgleason@mgh.harvard.edu

Keywords: Huntington's disease, striatum, lipidomics, transcriptomics, myelin, sphingolipid

ABSTRACT

Background: Expansion of a triplet repeat tract in exon1 of the HTT gene causes Huntington's disease (HD). The mutant HTT protein (mHTT) has numerous aberrant interactions with diverse, pleiomorphic effects. No disease modifying treatments exist but lowering mutant huntingtin (mHTT) by gene therapy is a promising approach to treat Huntington's disease (HD). It is not clear when lowering should be initiated, how much lowering is necessary and for what duration lowering should occur to achieve benefits. Furthermore, the effects of mHTT lowering on brain lipids have not been assessed.

Methods: Using a mHtt-inducible mouse model we analyzed whole body mHtt lowering initiated at different ages and sustained for different time-periods. Subcellular fractionation (density gradient ultracentrifugation), protein chemistry (gel filtration, western blot, and capillary electrophoresis immunoassay), liquid chromatography and mass spectrometry of lipids, and bioinformatic approaches were used to test effects of mHTT transcriptional lowering.

Results: mHTT protein in cytoplasmic and synaptic compartments of the caudate putamen, which is most affected in HD, was reduced 38-52%. Little or no lowering of mHTT occurred in nuclear and perinuclear regions where aggregates formed at 12 months of age. mHtt transcript repression partially or fully preserved select striatal proteins (SCN4B, PDE10A). Total lipids in striatum were reduced in LacQ140 mice at 9 months and preserved by early partial mHtt lowering. The reduction in total lipids was due in part to reductions in subclasses of ceramide (Cer), sphingomyelin (SM), and monogalactosyldiacylglycerol (MGDG), which are known to be important for white matter structure and function. Lipid subclasses phosphatidylinositol (PI), phosphatidylserine (PS), and bismethyl phosphatidic acid (BisMePA) were also changed in LacQ140 mice. Levels of all subclasses other than ceramide were preserved by early mHtt lowering. Pathway enrichment analysis of RNAseq data imply a transcriptional mechanism is responsible in part for changes in myelin lipids, and some but not all changes can be rescued by mHTT lowering.

Conclusions: Our findings suggest that early and sustained reduction in mHtt can prevent changes in levels of select striatal proteins and most lipids but a misfolded, degradation-resistant form of mHTT hampers some benefits in the long term.

46 **BACKGROUND**

47 Huntington's disease (HD) is a heritable neurodegenerative disease caused by a CAG expansion in the
48 huntingtin (*HTT*) gene. The protein product, huntingtin (HTT), is ubiquitously expressed but enriched in neurons [1,2]
49 and has been implicated in numerous molecular functions including vesicle trafficking, autophagy, transcription and
50 DNA repair (Reviewed by [3–5]). HTT has also been shown to have essential functions during development [6–11]. The CAG-
51 repeat expansion encodes a polyglutamine expansion in HTT, which causes protein accumulation and aggregation
52 and has pleiomorphic effects that contribute to HD pathology ranging from mitochondrial dysfunction,
53 transcriptional defects, cholesterol mishandling, altered palmitoylation, and metabolic changes from altered signaling
54 in the hypothalamus [12,13].

55 *HTT* transcription lowering strategies have become central to HD translational studies (reviewed by [14]).
56 Interventional trials have targeted total *HTT* (that is, normal and mutant *HTT*) using antisense oligonucleotides (ASOs)
57 (reviewed by [15]) or *HTT* pre-mRNA using an oral drug, branaplam (LMI070) [16]. In animal models (mice, sheep, and
58 nonhuman primates), additional strategies of gene therapy using transcriptional repressors to target expression from
59 the mutant allele [17] and modified interfering RNAs (RNAi) [18] or AAV expressing microRNAs (miRNAs) or short hairpin
60 RNAs (shRNAs) [19,20] to target RNA levels are actively being pursued [17,21–28].

61 Although lowering total *HTT* in humans was hoped to be generally safe [29], insufficient evidence currently
62 exists to make this conclusion. There is support for selective lowering of m*HTT* based on data in mice that show loss
63 of wild type (WT) *HTT* may affect neuronal function including synaptic connectivity [6,8,30,31].

64 Proteins known to change with HD progression may serve as useful readouts for investigating the efficacy of
65 HTT lowering. For instance, DARPP32 is enriched in striatal projection neurons and is progressively reduced in HD
66 patient postmortem brain and in mouse HD models [32]. The cAMP phosphodiesterase PDE10A is reduced early and
67 sustainably in HD striatum measured both by western blot and mass spectrometry [17,33,34] or ligand binding [17,35].
68 Microarray analysis in neurons derived from human stem cells [36], mass spectrometry and western blot analyses in
69 striatal synaptosomes [33] and immunofluorescence (IF) studies in mice [37] showed SCN4B is lowered in HD models.
70 ATP5A protein levels are altered in numerous mass spectrometry studies [33,38–40].

71 The intracellular location of HTT positions it to affect lipids in membranes. HTT normally associates with
72 membranes where it interacts directly with lipid bilayers [41]. Lipids comprise ~50% of the total dry weight in brain and

73 have diverse cellular roles as membrane structural components, signaling molecules, and sources of energy [42].
74 Disruptions to lipid composition/metabolism have been linked to disease [43]; thus, their study may provide insight into
75 disease mechanism or lead to discovery of new biomarkers. We and others have described alterations to lipid levels
76 in HD mouse models [44–48] and post-mortem HD brain tissue [49–51]. Specific glycerophospholipids showed differential
77 associations with mHTT [52] and mHTT can alter the biophysical properties of lipid bilayers [41,53] underscoring the
78 potential for direct consequences of the presence of mHTT on cellular lipids.
79 The effects of lowering total *Htt* or m*Htt* alone on striatal proteins and behavioral and psychiatric measures
80 have been investigated in HD mouse models after delivery of reagents to the striatum or lateral ventricle [17,54].
81 Biomarkers (mHTT levels and aggregation) that are responsive to total or m*Htt* lowering have been investigated in HD
82 mouse models [35,55,56]. However, the impact of lowering m*Htt* on lipids has not been examined. Here we used the
83 inducible HD knock-in mouse model, LacQ140, in which the expression of m*Htt* alone is regulated by adding or
84 withdrawing the lactose analog isopropyl b-D-1-thiogalactopyranoside (IPTG) in their drinking water [57–60], to study the
85 effects of m*Htt* lowering for different time periods on proteins known to be affected in HD models and using a survey
86 of lipids. We also tracked changes in levels of soluble and aggregated mHTT protein in different subcellular
87 compartments. The results show that early and sustained reduction in m*Htt* in this HD mouse model can delay select
88 protein changes and prevent numerous lipid derangements. Using a systems biology approach, we integrated our
89 lipidomic findings with a previously generated transcriptomic dataset, identifying dysregulation of pathways relating
90 to myelin and white matter including genes directly involved in biosynthetic pathways for lipids we found changed in
91 LacQ140 mice. An SDS-soluble misfolded form of mHTT persists, however, and benefits eventually dwindled.
92

93 **MATERIALS AND METHODS**

94 **Animals**

95 The *LacO*/*LacIR*-regulatable HD mouse model (LacQ140) was generated by crossing the $Htt^{LacQ140/+}$ mouse to the
96 $Tg^{ACTB\text{-}lacI*Scrb}$ mouse as previously described [58,59]. The default state of the LacQ140 mouse is global repression of m*Htt*
97 due to *Lac* Repressor binding to the *Lac* operators. The continuous administration of IPTG starting from E5 interrupts
98 the binding between the *Lac* repressor and operators, resulting in a de-repressed state, and maximal expression of
99 m*Htt* in LacQ140. All WT mice were $Htt^{LacO+/+}$; b-actin-$LacI^{R}$ tg. Mice were provided with enrichment (envirodry, play

100 tunnels, Bed-o'cobs and plastic bones) and housed uniform for genotype, gender, and treatment. Mice were fed *ad*
101 *libitum*. The lactose analog IPTG was provided in drinking water (at 10mM) which de-represses the *LacQ140* allele
102 and keeps normal m*Htt* expression. During embryonic development, m*Htt* expression levels were maintained at
103 normal levels by administering IPTG to pregnant dams starting at embryonic day 5 (E5). IPTG was administered never
104 (*mHtt* repressed), always (*mHtt* always expressed) or withdrawn at 2 or 8 months (*mHtt* expressed normally then
105 repressed at 2 or 8 months). The CAG repeat length range in $Htt^{LacO\text{-}Q140/+}$ mice was 143-157 with average of 148 and
106 median of 148 CAG.

107 **Sample preparation**

108 The striatum from one hemisphere for each mouse was homogenized in 750 µl 10mM HEPES pH7.2, 250mM sucrose,
109 1uM EDTA + protease inhibitor tablet (Roche Diagnostics GmbH, Mannheim, Germany) + 1mM NaF + 1mM Na3VO4.
110 A 150 µl aliquot of this crude homogenate was removed and protein concentration was determined using the
111 Bradford method (BioRad, Hercules, CA). Subcellular fractionation by density gradient ultracentrifugation using
112 Optiprep was performed on remaining 600 µl sample for the 6- and 12-month-old mice as previously described [47].

113 **Capillary immunoassay**

114 Equal amounts of protein from the crude homogenates were analyzed using the automated simple western system,
115 Wes (ProteinSimple, Bio-Techne, San Jose, CA), which utilizes a capillary-based immunoassay. The protocol described
116 in the manual was followed to detect HTT, GFAP and DARPP32 using 0.6 µg of sample. Quantitative analysis of
117 protein levels is done automatically using the Compass for Simple Western Software (ProteinSimple) on
118 electropherogram data. The peak area (using automatic "dropped line" option in software) of each protein of interest
119 was normalized to the peak area of the vinculin loading control. Figures show protein bands similar to traditional
120 western blots using "lane view" option in the Compass software to create a blot-like image from the
121 electropherogram data.

122 **Western blot analysis**

123 Equal amounts of protein from the crude homogenates were analyzed by western blot for levels of HTT and other
124 proteins of interest as previously described [33]. Briefly, 10 µg of protein were separated by SDS-PAGE, transferred to
125 nitrocellulose, and probed with primary antibody overnight. Nitrocellulose membranes were cut into horizonal strips

126 to maximize the number of antibodies that could be probed on one blot. Peroxidase labeled secondary antibodies
127 were used with the SuperSignal West Pico Chemiluminescent substrate (ThermoScientific, Rockford, IL, #34580) and
128 digital images were captured with a CCD camera (AlphaInnotech, Bayern, Germany). For western blot analysis of
129 subcellular fractions, equal volumes of each sample (15 µl) were separated by SDS-PAGE. Pixel intensity
130 quantification of the western blot signals on the digital images was determined using ImageJ software (NIH) by
131 manually circling each band and multiplying the area by the average signal intensity. The total signal intensity was
132 normalized to vinculin or GAPDH loading controls.

133 **Antibodies**

134 The following antibodies and dilutions were used in this study: Anti-HTT Ab1 (aa1-17,[1]) 1:50 for capillary
135 immunoassay and 1:2000 for western blot; anti-HTT EPR5526 (Abcam, Waltham, MA, ab109115, 1:2000 for western
136 blot); anti-polyQ MW1 (MilliporeSigma, Burlington, MA, MABN2427, 1:50 for capillary immunoassay); anti-polyQ
137 PHP3 (generous gift from Dr. Ali Khoshnan, 1:2000 for western blot); Anti-PDE10A (Abcam, Waltham, MA,
138 #ab177933, 1:2000 for western blot); Anti-DARPP32 (Abcam, #ab40801, 1:2000 for capillary immunoassay); Anti-
139 GFAP (MilliporeSigma, Burlington, MA, AB5804, 1:3000 for capillary immunoassay); Anti-GAPDH (MilliporeSigma,
140 Burlington, MA, #MAB374, 1:10000 for western blot); Anti-Sodium channel subunit beta-4 (Abcam, Waltham, MA,
141 #ab80539, 1:500 for western blot); Anti-vinculin (Sigma, St. Louis, MO, #V9131, 1:5000 for capillary immunoassay,
142 1:2000 for western blot); Anti-ATP5A (Abcam, Waltham, MA, #ab14748, 1:2000 for western blot); Anti-HTT MW8
143 (University of Iowa Developmental Studies Hybridoma Bank, 1:1000 for filter trap); Anti-HTT S830 (generous gift from
144 Dr. Gillian Bates, [61] 1:8000), HDAC1 (Abcam, Waltham, MA, ab32369-7, 1:4000).

145 **Filter trap assay**

146 Based on protocol described in [62,63], equal protein amounts for each sample (40 µg) were brought up to 50 µl volume
147 with PBS and 50 µl 4% SDS in PBS was added to each sample to make final concentration 2% SDS. A cellulose acetate
148 membrane was wet in 2% SDS/PBS and placed in dot blot apparatus. The 100 µl samples were added to each well
149 and pulled through the membrane with a vacuum then washed 3 times with 200 µl 2% SDS/PBS. The membrane was
150 removed from the apparatus, washed in Tris buffered saline + 0.1% Tween-20 (TBST) then processed for western blot

151 using MW8 or S830 antibodies. The total signal intensity of each dot was measured in ImageJ by circling the entire
152 dot and multiplying the area by the average signal intensity minus the background signal from an empty dot.

153 **Statistical analysis**

154 One-way ANOVA with Tukey's multiple comparison test was performed to determine significance between groups.
155 Asterisks on graphs show p values and are described in the figure legends.

156 **Lipid extraction**

157 Lipids were extracted using methyl tert-butyl ether (MTBE) as previously described and analyzed using ion switching
158 and molecular assignment as previously described [47,64,65]. Each age group was processed together. Crude
159 homogenates (100 µl) of dissected mouse striatum were transferred into 20 ml glass scintillation vials. 750 µl of HPLC
160 grade methanol was added to each sample, then vials were vortexed. 2.5 ml of MTBE was then added to each sample
161 and incubated on a platform shaker for 1 hour. After incubation, 625 µl of water was added to induce polar and non-
162 polar phase separation. The non-polar lipid containing (upper) phase was collected into a new vial, and the polar
163 (lower) phase was subsequently re-extracted with 1 ml of MTBE/methanol/water (10/3/2.5, v/v/v). Following re-
164 extraction, the lipid containing phases were combined and allowed to dry on a platform shaker, then further dried
165 with nitrogen gas. Extracted lipids were hand delivered to the Beth Israel Deaconess Medical Center Mass
166 Spectrometry Core Facility.

167 **Lipid Annotation**

168 Data for each timepoint was classified by LIPID MAPS category[66]: glycerophospholipids, glycerolipids, sphingolipids,
169 sterol lipids, fatty acyls, and prenol lipids were detected. Each category contains distinct subclasses as annotated
170 below. *Glycerophospholipids:* Phosphatidylcholine (PC), Phosphatidylethanolamine (PE), Phosphatidylserine (PS),
171 Phosphatidylinositol (PI), Methylphosphocholine (MePC), Phosphatidic acid (PA), Bis-methyl phosphatidic acid
172 (BisMePA), Dimethyl phosphatidylethanolamine (dMePE), Phosphatidylgylcerol (PG), Bis-methylphosphatidylserine
173 (BisMePS), Bis-methyl phosphatidyl ethanolamine (BisMePE), Cardiolipin (CL), Phosphatidylethanol (PEt), Biotinyl-
174 phosphoethanolamine (BiotinylPE), Phosphatidylmethanol (PMe), Phosphatidylinositol-bisphosphate (PIP2),
175 Phosphatidylinositol-monophosphate (PIP), Lysophosphatidylcholine (LPC), Lysophosphatidylethanolamine (LPE),
176 Lysophosphatidylserine (LPS), Lysophosphatidylinositol (LPI), Lysophosphosphatidylgylcerol (LPG), Lysodimethyl

177 phosphatidyl ethanolamine (LdMePE). *Glycerolipids:* Triglyceride (TG), Monogalactosyldiacylglycerol (MGDG),
178 Monogalactosylmonoacylglycerol (MGMG), Diglyceride (DG), Sulfoquinovosylmonoacylglycerol (SQMG),
179 Sulfoquinovosyldiacylglycerol (SQDG). *Sphingolipids:* Hexosylceramides (Hex1Cer), Simple Glc series (CerG1),
180 Sphingomyelin (SM), Ceramide (Cer), Ceramide phosphate (CerP), Sulfatide (ST), Sphingoid base (So), Sphingomyelin
181 phytosphingosine (phSM), Simple Glc series (CerG2GNAc1), Ceramide phosphorylethanolamine (CerPE), Sphingosine
182 (SPH), Dihexosylceramides (Hex2Cer). *Sterol lipids*: Cholesterol ester (ChE), Zymosterol (ZyE). *Fatty acyls:* Fatty acid
183 (FA), Acyl Carnitine (AcCa). *Prenol lipids:* Coenzyme (Co).
184 Individual lipid species were annotated according to sum composition of carbons and double bonds in the format
185 Lipid Subclass (total number of carbons: total number of double bonds). If distinct fatty acid chains could be
186 identified, they were annotated separated by an underscore (ex. PC 32:1, or PC (16:0_16:1). Using this approach, we
187 cannot determine the *sn*-1 or *sn*-2 positions of the fatty acid chains. Lipid species within the sphingolipid category
188 contain prefixes 'd' or 't' to denote di-hydroxy or tri-hydroxy bases. For example, SM(d18:1_23:0) contains 2 hydroxyl
189 groups. The Hex1Cer subclass is comprised of both glucosylceramide (GlcCer) and galactosylceramide (GalCer); the
190 orientation of one of the hydroxyl groups in Glc differs from in Gal, and thus cannot be resolved by these methods [67].
191 Plasmanyl lipid species (ether linked) are annotated by 'e' and plasmenyl/plasmalogen (vinyl ether linked) lipid
192 species are annotated by 'p' (ex. PC (36:5e) or PE (16:0p_20:4) [68].

193 **Lipidomics statistics and data visualization**

194 Heatmap and hierarchical clustering in Figure 4 were generated using Morpheus from the Broad Institute
195 (Cambridge, MA, https://software.broadinstitute.org/morpheus). Hierarchical clustering was performed across all
196 rows (lipid subclasses) using the one minus Pearson correlation distance metric. Rows determined to be the most
197 similar are merged first to produce clusters, working iteratively to merge rows into clusters. The dendrogram displays
198 the order of clustering with the most similar rows shown in closest proximity. Lipid expression values are assigned to
199 colors based on the minimum (blue, low relative expression) and maximum (red, high relative expression) values for
200 each independent row. Heatmap in Figures 4 & 5 was generated in R using the ComplexHeatmap package v2.16.0 [69].
201 Each column represents data from one animal. Statistical significance was determined by one-way analysis of
202 variance (ANOVA) with Tukey's multiple comparison test between treatment groups for lipid subclasses (6mo: N=36,

203 9mo: N=24, 12mo: N=29) or lipid species (6mo: N=800, 9mo: N=632, 12mo: N=735). The two-stage linear step-up
204 procedure of Benjamini, Krieger, and Yekutieli was applied to ANOVA p-values to control the false discovery rate
205 (FDR) with significance accepted at q<0.05 (Q=5%).

206 **RNA-sequencing analysis**

207 The raw counts matrix derived from striatal samples in the LacQ140 mouse model was accessed from Gene
208 Expression Omnibus (GEO GSE156236). The 6-month cohort included n=10 mice per group (WT, LacQ140,
209 LacQ140_2M, LacQ140_A) and the 12-month cohort included n=10 WT, n=9 LacQ140, n=9 LacQ140_8M, n=10
210 LacQ140_2M, and n=10 LacQ140_A. Analysis was performed using R v4.3.0 in the RStudio IDE (2023.03.0+386).
211 Transcripts with fewer than 10 total counts were removed from the analysis. Differential expression analysis was
212 performed using DESeq2 v1.40.1 [70]. P-values were computed with the Wald test and were corrected for multiple
213 testing using the Benjamini and Hochberg procedure [71]. Genes with a fold change greater than 20% in either direction
214 and with an adjusted p-value < 0.05 were considered differentially expressed. Functional enrichment analysis was
215 conducted using the ClusterProfiler package v4.8.1. Over-representation analysis was performed for upregulated or
216 downregulated DEGs with the enrichGO function (org.Mm.eg.db v3.17.0). Gene set enrichment analysis was
217 performed with the gseGO function using a ranked list of genes (Wald statistic) for each comparison (LacQ140 vs WT,
218 LacQ140_8M vs WT, LacQ140_2M vs WT, and LacQ140_A vs WT) at 6 and 12 months. Heatmaps were plotted using
219 ComplexHeatmap package v2.16.0 with rows representing individual animals and rows representing genes.

220

221 **RESULTS**

222 **Time course of mHTT protein lowering with regulated transcriptional repression using LacQ140 mouse striatum**

223 We used the inducible HD knock-in mouse model, LacQ140, in which the expression of m*Htt* throughout the
224 body was regulated by adding or withdrawing the lactose analog isopropyl b-D-1-thiogalactopyranoside (IPTG) in
225 drinking water using an established *Lac* operator/repressor system (**Fig. 1a**) [59,60]. We used the model to lower m*Htt*
226 from conception, starting at 2 or 8 months of age. To control for the effects of IPTG, WT mice also received IPTG
227 treatment over their lifetime. The striatum was examined at 6, 9, and 12 months of age (**Fig. 1b**). Antibodies against
228 varied epitopes within HTT detect different pools of normal and mutant HTT by immunofluorescence and

229 immunohistochemistry [1,72–75]. Numerous conformations (over 100 distinct classes) of purified HTT and mHTT have
230 been identified by electron microscopy in vitro [76]. Polyglutamine (polyQ) expansion induces confirmational changes
231 particular to mHTT detectible even after SDS-PAGE and/or western blot with several antibodies to regions in the
232 poly-Q region (MW1 [77,78] and 3B5H10 [79]) and in the adjacent polyproline region (PHP1-4 [80] and S830 [81]). To assess
233 lowering, full length HTT and mHTT proteins were detected by capillary immunoassay using anti-HTT antibody Ab1
234 targeting aa 1-17 and anti-polyQ antibody MW1 (**Fig. 2**), and by western blot using anti-HTT antibody EPR5526, and
235 anti-mHTT antibody PHP3, which recognizes an altered conformer of polyproline in mHTT [80] (**Fig. S1**).
236 Overall, results showed lowering of 35-52% of mHTT detected with Ab1, MW1 and PHP3 in 6- and 9-month
237 mice with transcriptional repression **(Fig. 2a, Fig. S1a)** and **(Fig. 2b, Fig. S1b)**. Although EPR5526 recognizes both WT
238 and mHTT, no significant lowering of mHTT protein was measured with mHtt gene repression using this antibody in
239 6-month mice. In the 12-month mice, mHTT was significantly reduced in LacQ140_A (51%) mice compared to
240 LacQ140 mice (**Fig. 2c)**. However, this was observed only in the capillary immunoassay using antibody Ab1 but not
241 with antibodies MW1, EPR5526, or PHP3 **(Fig. S1c)**. m*Htt* repression in the LacQ140_2M and LacQ140_8M mice
242 yielded no significant reduction of mHTT protein levels compared to LacQ140 mice using any antibody. These results
243 show that systemic regulated repression of m*Htt* transcription in LacQ140 mice results in partial lowering of mHTT
244 protein levels in the striatum (38-52%), but a soluble form of full-length mHTT remains as mice age.

245 **Effects of m*Htt* lowering on its distribution in different subcellular cytoplasmic compartments**

246 We next looked at the effects of m*Htt* repression on its protein levels in different subcellular compartments.
247 Density gradient fractionation and ultracentrifugation for subcellular fractionation of cytoplasmic components was
248 performed as shown in **Fig. S2a**. The schematic in **Fig. S2b** indicates representative proteins that are enriched in
249 different cytoplasmic compartments. In 6-month-old mice, the mHTT/WT HTT ratio was significantly lower in
250 LacQ140_2M mice in fractions 13 and 14 compared to LacQ140 mice (**Fig. S2c and d**). Similar results were observed
251 in 12-month-old mice, where the mHTT/WT HTT ratio in fractions 1, 3, 13, and 14 in LacQ140 mice was significantly
252 lower with m*Htt* repression for different periods of time compared to LacQ140 mice (**Fig. S2e and f**). There was no
253 change in the distribution of HTT and mHTT in the fractions between groups in 6-month-old mice **(Fig. S3a and b)** or

254 in 12-month-old mice **(Fig. S3c and d)**. Altogether, these results show that mHTT is lowered in cytoplasmic fractions
255 through 12 months.

256 **Effects of m*Htt* lowering on its distribution in crude nuclear fractions**

257 In 12-month-old LacQ140 mice, repressing m*Htt* transcription only partially reduced levels of mHTT protein in
258 crude homogenates (**Fig. 2c**) even though mHTT was efficiently lowered in the sub cytoplasmic compartments
259 contained in the S1 fraction (**Fig. S2f**). We speculated that mHTT may reside in other compartments where it is more
260 resistant to removal by transcript repression. To address this idea, we examined P1 fractions which contain nuclei,
261 ER, large perinuclear structures such as the recycling compartment, some mitochondria and autophagosomes [82]. HTT
262 was detected with antibody Ab1 in WT mice (2 alleles worth) and LacQ140 mice (1 allele worth) and mHTT (1 allele
263 worth) in LacQ140 mice at both 6 and 12 months (**Fig. 3a and b**). Significant lowering of mHTT protein was observed
264 in 6-month-old LacQ140_A but not LacQ140_2M mice using antibody Ab1 (**Fig. 3a**). In 12-month mice, repression of
265 the m*Htt* allele at any age or duration failed to lower mHTT protein levels in the P1 fraction (**Fig. 3b**).

266 We queried whether forms of mHTT with altered migration with SDS-PAGE could be detected in the P1
267 fractions using antibody S830, which has been reported by us and others to detect a smear using SDS-PAGE and
268 western blot [61,83]. At 12-months, HD mice showed an S830-positive smear above the HTT/mHTT bands which was not
269 lowered in the LacQ140_8M, LacQ140_2M, or LacQ140_A mice (**Fig. 3c**). Filter trap assay showed lowering of an SDS-
270 insoluble aggregated species (recognized by S830) in both crude homogenate and P1 fractions; slightly less lowering
271 of aggregated mHTT occurred in the P1 fraction when transcript repression was initiated at 2 or 8 months (**Fig. S4a**
272 **and b**). Altogether, these results show that a soluble species of mHTT in the P1 fraction is more resistant to lowering
273 after transcriptional repression.

274 **Effects of m*Htt* lowering on levels of GFAP, DARPP32, SCN4B, PDE10A, and ATP5A**

275 Prior studies in different mouse models of HD have shown that levels of some neuronal proteins are altered
276 in the mouse striatum, namely DARPP32, PDE10A, SCN4B, and ATP5A [32–34,37–40,84]. To assess levels of these proteins
277 and that of the astrocyte protein, glial acidic fibrillary protein (GFAP), in LacQ140 mice without and with m*Htt* gene
278 repression, crude homogenates from 6, 9, and 12-month-old mice were analyzed by capillary immunoassay or
279 western blot.

280 In agreement with previous studies in HD mouse models [17,33,34] striatum from the LacQ140 exhibited a
281 significant reduction in PDE10A at all ages examined. Early m*Htt* lowering starting at 2 months of age statistically
282 preserved PDE10A levels at 6 and 9 months (**Fig. S5a and b**), but the effect was lost by 12 months of age when
283 transcript repression was initiated at 2 or 8 months (**Fig. S5c**). Transcript repression initiated embryonically
284 (LacQ140_A) and examined at 6 and 12 months preserved PDE10A levels, although no protection was observed at 9
285 months. SCN4B expression was reduced in the striatum of LacQ140 at 6 and 9 months of age and levels were
286 preserved with early m*Htt* lowering (**Fig. S5a and b**). DARPP32 levels were significantly lower in LacQ140 compared
287 to WT mice at 9 months but not at 6 or 12 months, and there were no differences in levels of GFAP and ATP5A
288 between WT and LacQ140 at any age examined (**Fig. S6a-c**).

289 **Effects of m*Htt* lowering on lipids detected by mass spectrometry**

290 We surveyed for lipid changes in LacQ140 striatum compared to WT and the effects of lowering m*Htt* using
291 liquid chromatography and mass spectrometry (LC-MS) as previously described [47]. For each age, lipids were extracted
292 from crude homogenates of striatum from each treatment group/genotype and analyzed as a set. The total lipids per
293 group were compared. Our MS intensity measurements were relative measurements so only samples processed
294 together can be compared (i.e., by age group). The sum of lipids for each genotype and/or treatment group were
295 reported as a proportion of WT within each age group (**Fig. 4a-c**). No changes in total lipid were observed at 6
296 months or 12 months (**Fig. 4a and c**). However, at 9 months LacQ140 mice had significantly lower levels of total lipids
297 compared to WT or to LacQ140_A mice **(Fig. 4b**). A heat map and hierarchical clustering of lipid changes by subclass
298 at 9 months revealed two major groups where-in subclasses moved in the same direction even if all weren't
299 statistically significant (**Fig. 4d**). The top cluster delimited in blue shows subclasses that decreased in LacQ140 mice
300 compared to WT and were corrected by lowering. In contrast, the cluster marked in red shows subclasses that were
301 increased in LacQ140 mice compared to WT and were improved by m*Htt* lowering**.** Other subclasses marked in black
302 did not change. Summaries of lipid subclasses and number of species detected for each age group are in **Table 1,** and
303 an overview of changes in individual species across ages is shown in **Table 2**. Data and graphs for 6-month-old mice
304 subclasses and species can be found in **Fig. S7 & 8** and **Additional File 1**; 9-month-old mice in **Fig. S9 & 10** and
305 **Additional File 1**; and 12-month-old mice in **Fig. S11 & 12** and **Additional File 1**.

306 We assessed if there were more subtle alterations at the subclass or individual species level that did not
307 influence the overall lipid levels. In striatum of LacQ140 mice at 6-months-of-age, we detected a modest increase in
308 the subclass phosphatidylinositol (PI) compared to WT (**Fig. S7**). Individual species of PI (18:0_20:4, 16:0_22:6), and
309 phosphatidylserine PS (18:0_20:4, 22:6_22:6) were increased in LacQ140 mice compared to WT (**Fig. S8**). However,
310 no subclass or species changes survived correction using the Benjamini, Krieger, and Yekutieli procedure with a 5%
311 false discovery rate (FDR) of q <0.05, N=36 subclasses (**Table 1**) and N=800 species (**Additional File 1)**. Consistent with
312 our observations at 6 months, PS and PI were increased in 9-month-old LacQ140 mice compared to WT (**Fig. 5a and**
313 **b**). A limited number of species are modestly increased at 6 months, which progresses to more robust increases in
314 these glycerophospholipids at the subclass level at 9 months. A significant reduction in bismethyl phosphatidic acid
315 (BisMePA) also occurred (**Fig. 5c**). Functionally, PI is the precursor for PIPs which are important for protein kinase c
316 (PKC) signaling at the synapse [85] and can also act as important docking and activating molecules for membrane
317 associated proteins, including HTT [52]. PS is an abundant anionic glycerophospholipid necessary for activation of
318 several ion channels [86], fusion of neurotransmitter vesicles, regulation of AMPA signaling, and coordination of PKC,
319 Raf-1, and AKT signaling [87].
320 In contrast to the increases observed in glycerophospholipids, 9-month-old LacQ140 mice exhibit significant
321 reductions in the subclasses sphingomyelin (SM) and ceramide (Cer) (**Fig. 5d and e),** lipids central in sphingolipid
322 metabolism and important for myelination. Cer is the backbone for SM as well as more complex glycosphingolipids,
323 which are highly enriched in myelin [88]. Moreover, the low abundance glycerolipid monogalactosyldiacylglycerol
324 (MGDG) was strikingly reduced at 9 months (**Figure 5f**). MGDG regulates oligodendrocyte differentiation and is
325 considered a marker of myelination [89,90].
326 All subclasses (PI, PS, BisMePA, SM, Cer, MGDG) with changes between WT and LacQ140 had q values<0.05
327 (N=24 subclasses) (**Table 1; Fig. 4d**). Early lowering of m*Htt* (LacQ140_A) restored levels of each of these subclasses
328 except for Cer and lowering m*Htt* starting at 2 months (LacQ140_2M) was sufficient to correct levels of SM and
329 MGDG (**Fig. 5a-f**)**.** To assess the effects of m*Htt* lowering on the distinct lipid species that comprise each subclass,
330 lipid species were plotted in a heatmap **(Fig. 5g).** The broad changes at the subclass level can be attributed to large
331 numbers of individual lipid species changing within each subclass even if each species is not significantly different
332 (**Fig. 5g & Fig. S9**). Alternatively, subclasses can remain unchanged but still contain individual lipid species with

333 differences. For example, the subclass Hex1Cer was not significantly changed **(Fig. S9)**, but many individual species
334 were significantly altered in LacQ140 mice **(Fig. S10).** These species included 3 that were significantly decreased in
335 LacQ140 mice and normalized to WT levels with lowering of m*Htt*: Hex1Cer (d18:1_18:0), Hex1Cer (t18:0_18:0),
336 Hex1Cer (d18:1_25:1) **(Fig. S10).** Combined, these 3 species represent approximately 1% of total Hex1Cer detected.
337 Hex1Cer is comprised of galactosylceramide and glucosylceramide and cannot be distinguished by LC-MS/MS;
338 however, previous studies have determined that the majority of Hex1Cer in the brain is galactosylceramide, which is
339 highly enriched in myelin [67,91]. Galactosylceramides are major constituents of the myelin sheath and contribute to its
340 stabilization and maintenance [92].

341 In total, we identified 14 lipid species significantly altered between LacQ140 and WT mice using a stringent
342 FDR cutoff (FDR 5%/q<0.05, Benjamini, Krieger, and Yekutieli procedure, N=632 lipids) and all 14 showed
343 improvement with m*Htt* lowering at 9 months (**Fig. S10**). This included increases in PI (16:0_20:4) & PI (18:1_20:4)
344 and PS (18:0_20:4), PS (18:0_18:1) and PS (18:1_22:6). Lipid species decreased in LacQ140 mice and restored with
345 m*Htt* lowering included Hex1Cer species as detailed above, SM (d40:2), PE (16:0p_20:4) and MGDG (16:0_18:1) (**Fig.
346 5g, Fig. S10)**. Taken together, these results indicate a profound disruption of myelin lipids in LacQ140 mice, which is
347 attenuated with lowering of m*Htt.*

348 In the striatum of LacQ140 mice at 12 months, no significant differences at the subclass level were found
349 compared to WT (**Table 1; Fig. S11**) although 29 subclasses were measured. At the individual lipid species level, we
350 identified 26 lipid species significantly altered between LacQ140 and WT mice (FDR 5%/q<0.05, Benjamini, Krieger,
351 and Yekutieli procedure, N=735 lipids). (**Fig. S12**). Contrary to the reversal of lipid dysregulation observed at 9
352 months, the only lipid species that was responsive to lowering m*Htt* at 12 months was CerP (t40:3), which was
353 increased in LacQ140 and decreased with early m*Htt* lowering (LacQ140_A) (**Fig. S12**). Myelin enriched lipids,
354 including 6 species of Hex1Cer (d18:1_18:0, d:40:2, d18:2_22:0, d41:2, t18:0_22:1 & d18:1_22:1) and ST
355 (d18:1_22:1), decreased and were not improved with m*Htt* lowering (**Fig. S12**). Similarly, nine triacylglycerol (TG)
356 species, eight of which contain oleic acid (C18:1) were decreased in LacQ140 mice and unchanged with m*Htt*
357 lowering (**Fig. S12**). Overall, these results demonstrate that most individual lipid changes were no longer reversible by
358 12 months.

359 **Bioinformatic analysis of transcriptional alterations to lipid metabolism and myelination**

360 To determine if any of the lipid changes could be explained by altered transcription of genes regulating lipid-
361 related metabolic pathways, we re-analyzed the previously generated RNAseq dataset in the LacQ140 striatum (GEO
362 GSE156236). Differential expression analysis [70] detected 1360 upregulated and 1431 downregulated genes at 6
363 months and 1375 upregulated and 1654 downregulated genes at 12 months (FC>20%, adjusted p-value <0.05) **(Fig.**
364 **S13a).** Over-representation analysis against GO Biological Processes (GO BP) revealed that downregulated genes
365 were enriched in terms related to lipid metabolism and signaling as well as myelination. In 6-month LacQ140
366 downregulated genes, GO BP terms ensheathment of neurons (padj<0.01), axon ensheathment (padj<0.01),
367 myelination (padj<0.05), cellular lipid metabolic process (padj<0.05), lipid metabolic process (padj<0.05),
368 phospholipase C-activating G protein-coupled receptor signaling pathway (padj<0.05), response to lipid (padj<0.05)
369 were significantly over-represented **(Fig. 6a)**. In LacQ140 upregulated genes, there was no over-representation of
370 terms that could directly explain changes to lipid levels **(Additional File 2).**

371 Next, Gene Set Enrichment Analysis (GSEA) was conducted [93,94] to examine the impact of m*Htt* repression on
372 the enrichment profiles of terms related to lipid metabolism and myelination. At 6 months, 3 of the top 20 enriched
373 GO BP terms were related to myelination and all were negatively enriched: ensheathment of neurons, myelination,
374 and axon ensheathment **(Additional File 2)**. Further, every significantly enriched myelin or lipid related GO BP term
375 was negatively enriched in LacQ140 compared to WT (padj <0.05) (**Fig. 6b, Additional File 2)**. Repression of m*Htt* in
376 LacQ140_2M and LacQ140_A groups was sufficient to reverse the negative enrichment of many GO BP terms
377 including myelination/axon ensheathment/ensheathment of neurons, and sphingolipid/phospholipid metabolic
378 processes suggesting some beneficial impact of m*Htt* lowering (**Fig. 6b**).

379 Specifically, 6-month LacQ140 mice had reduced expression of genes encoding proteins involved in
380 oligodendrocyte development (*Akt2, Bcas1, Ptgds, Cldn11, Trf, Tcf7l2, Qki*), myelin structure and compaction (*Mbp,*
381 *Plp1, Tspan2, Mal*), and myelin lipid biosynthesis (*Ugt8a, Fa2h, Aspa*) (**Fig. 6c**). LacQ140 mice also exhibited
382 dysregulation of genes encoding enzymes including phospholipases (*Pla2g7, Pla2g4c, Pla2g4e, Plb1, Plcd3, Plcd4*),
383 phosphatases & kinases (*Plpp1, Plpp3, Plppr2, Inpp4b, Pik3c2b*), and regulators of phospholipid biosynthesis (*Gpat2,*
384 *Gpat3, Chpt1*) (**Fig. 6c**). Enzymes responsible for biosynthesis and metabolism of sphingolipids were altered in
385 LacQ140 mice: *Sptssb, Ormdl2, Gba2, Asah,* were downregulated and *Smpdl3b* was upregulated. Genes encoding

386 enzymes responsible for fatty acid elongation (*Elovl1, Elovl5, Elovl6*) were all downregulated (**Fig. 6c**). Of the DEGs
387 related to lipid metabolism and myelination 23 were reversed in LacQ140_2M mice, 23 were reversed in LacQ140_A
388 mice and 15 were reversed in both (padj < 0.05, FC > 20% opposite direction of LacQ140) (**Fig. 6c & Fig. S13b).**
389 Three of the nine GO BP terms significantly over-represented in 6-month LacQ140 downregulated genes
390 were also over-represented in 12-month downregulated genes: ensheathment of neurons (padj <0.01), axon
391 ensheathment (padj <0.01), myelination (padj <0.05), and phospholipase C-activating G protein-coupled receptor
392 signaling pathway (padj<0.01) (**Fig. 6d**). Similarly, GSEA showed that only a subset (8/22) of the GO BP terms related
393 to lipid metabolism or myelination were enriched at both timepoints (**Fig. 6e**). Terms including glycerophospholipid
394 metabolic process and glycerolipid metabolic processes showed improvement with lowering of m*Htt*, whereas terms
395 related to myelination remained negatively enriched with m*Htt* repression (**Fig. 6e**).
396 DEGs associated with myelin and lipid biosynthesis were both downregulated and upregulated in 12-month
397 LacQ140 mice. LacQ140 mice had reduced (*Cntnap1, Mal, Tspan2, Plp1, Mobp*) and increased (*Omg, Opalin*)
398 expression of genes encoding proteins involved in myelin structure and compaction (**Fig. 6f**). Similarly,
399 oligodendrocyte development related genes were both decreased (*Akt2, Cldn11, Myt1l*) and increased (*Prkcq, Olig1,*
400 *Sox11*). Genes related to myelin lipid biosynthesis (down: *Ugt8a, Fa2h, Selenoi*), phospholipid synthesis/metabolism
401 (up: *Chkb, Agpat2, Mboat2,* down: *Agpat1, Lpcat4*), phosphatases (up: *Plpp1, Plpp2, Plppr2,* down: *Plpp3, Plpp6,*
402 *Inpp5a*), phospholipases (up: *Pla2g4e,* down: *Plcb1, Plcb3, Plce1, Plcl1*) and sphingolipid synthesis/metabolism (up:
403 *Cers4, Smpdl3b, Acer3,* down: *Gba2, St3gal2, Smpd3, Sgpp2, Sgms1, A4galt, Fads3*) were differentially expressed in
404 both directions (**Fig. 6f)**. In 12-month LacQ140 mice, glycerolipid synthesis/metabolism genes (up: *Dgat1,* down:
405 *Dgat2, Dgat2l6, Lpin3, Dagla*) and DAG kinase genes (up: *Dgka, Dgkg,* down: *Dgkb, Dgki*) were differentially
406 expressed (**Fig. 6f**). Consistent with the enrichment results at this timepoint, fewer genes were reversed with
407 repression of m*Htt* (5 genes LacQ140_2M, 4 genes LacQ140_A) **(Fig. 6f & Fig. S13c)**.
408 Differentially expressed genes (DEGs) were also manually curated for genes that could directly impact levels
409 of PS, PI, sphingolipids, and glycerolipids. Phosphatidylserine synthase enzymes (*Ptdss1/Ptdss2*) [87] and rate limiting
410 enzymes for PI biosynthesis (CDP-Diacylglycerol Synthases: *Cds1/Cds2*) [95] were unchanged in 6- and 12-month
411 LacQ140 mice **(Additional Files 1 & 2)**. For glycerolipids, the only known enzymes that catalyze TG biosynthesis [96]

412 were increased (*Dgat1*) and decreased (*Dgat2*) at 12 months; mRNA levels remained unchanged with m*Htt*
413 repression **(Fig. 6f).**

414 Lipid changes might be explained by altered cellular composition of tissue. To address this possibility, we
415 surveyed for changes in transcript levels for cellular markers. No change in mRNA expression levels for the microglial
416 markers *Iba1* and *Cd68* or for the reactive astrocyte marker *Gfap* were observed that might indicate upregulation of
417 these cell types could account for the lipid changes. However, our transcriptional profiling did reveal an expression
418 signature consistent with altered oligodendrocyte development and alterations to myelin structure or compaction in
419 both 6- and 12-month-old mice **(Fig. 6c and f)**. UDP-galactose-ceramide galactosyltransferase (*Ugt8a*) is expressed in
420 oligodendrocytes where it catalyzes the formation of GalCer (Hex1Cer) from Cer; *Ugt8a* mRNA was decreased at both
421 6 and 12 months in the LacQ140 mice **(Fig. 6c & Fig. 7a).** Embryonic repression of m*Htt* and repression beginning at
422 2-months of age preserved *Ugt8a* mRNA measured at 6-months; however, the effect was lost by 12-months of age
423 **(Fig. 6c and f).** These mRNA results mirror our findings of Hex1Cer lipid levels measured using LC-MS in LacQ140
424 striatal lysates. GalCer and GlcCer are both members of the Hex1Cer subclass but cannot be distinguished by MS
425 since they are isomers with the same mass and charge [67]; the gene catalyzing the transfer of glucose to ceramide
426 (*Ugcg*) was not changed at the mRNA level, suggesting lower levels of Hex1Cer in LacQ140 mice are due to lower
427 levels of GalCer. Ugt8a can also transfer galactose to diacylglycerol to form the lipid MGDG [97] which we found was
428 decreased with m*Htt* expression and improved with m*Htt* lowering **(Fig. 5f and g).** In contrast, *Fa2h* mRNA was
429 reduced at 6 and 12-months but not improved with *mHtt* lowering **(Fig. 6c and f).** Fatty acid 2-hydroxylase, which is
430 encoded by *Fa2h,* modifies fatty acids substrates with a hydroxyl (-OH) group, producing 2-hydroxylated fatty acids
431 that are incorporated into myelin sphingolipids and provide stability[98] **(Fig. 7b and c)**. Overall, these data reveal
432 transcriptomic changes in key lipid metabolic and biosynthetic genes in LacQ140 striatum, which directly impact the
433 lipidomic profile. Critically, many of these lipidomic and transcriptomic alterations can be attenuated with lowering
434 of m*Htt*.

435

436 **DISCUSSION**

437 Here we used the LacQ140 inducible HD mouse model to initiate whole body m*Htt* reduction at different
438 ages and evaluate effects on proteins and lipids. Lowering mHTT protein by 38-52% in the LacQ140 caudate putamen,

439 starting from conception up to 12 months of age, was sufficient to prevent m*Htt* induced changes in the levels of
440 some proteins and some lipids. However, a resistant soluble species of the protein detected in older mice limited
441 long term benefit of m*Htt* lowering. Our lipid data show clear evidence of changes impacting myelin which
442 mechanistically is due in part to aberrant transcription as evidenced by differentially expressed genes regulating
443 some of the same lipids that were found altered. The correction of lipid changes we identified here correlates with
444 the behavioral changes measured previously in LacQ140 mice using a comprehensive set of unbiased, high-content
445 assays [59] in that behavior was closer to normal at 6 and 9 months with early mHTT lowering, but the protective effect
446 of lowering degraded by 12 months.

447 We identified forms of mHTT protein that were resistant to m*Htt* lowering detected by various HTT
448 antibodies. These resistant forms of mHTT identified by immunoblot may correspond to mHTT aggregates or foci
449 found to be resistant to lowering in LacQ140 mice using MSD and immunofluorescence methods [59]. Others have
450 described aggregated and soluble forms of mHTT that resist degradation in distinct cellular compartments, including
451 full length mHTT in the nucleus [17,99–101]. In the LacQ140 striatum, the SDS-soluble degradation-resistant form of full-
452 length mHTT, detected by us using antibodies S830, MW1 and EPR5526, resides in a perinuclear or nuclear
453 compartment which might correspond to the "juxtanuclear quality control compartment (JUNQ)" described by
454 Frydman and colleagues [102]. Accrual of misfolded mHTT in the nucleus likely contributes to transcriptional
455 interference and the eventual failure of prolonged benefits of modest mHTT lowering. Targeting these resistant
456 fractions of misfolded mHTT by a chaperone activity to aid in its degradation may be beneficial in combination with
457 gene therapy *HTT* lowering strategies.

458 We found that early, continuous partial lowering of mHTT protein for up to 12 months fully or partially
459 preserved PDE10A and SCN4B protein levels with initiation of lowering embryonically providing the highest benefits.
460 These data agree with previous findings showing preservation of *Pde10a* mRNA in the LacQ140 model after early
461 m*Htt* lowering [59] and preservation of the Pde10a PET signal in the Q175 model after striatal injection of AAV-HTT-ZFP
462 [17]. However, our data here indicate that the time points chosen for post-treatment analysis are important and that
463 changes do not follow a linear neurodegenerative trajectory in mice. The greatest number of protein and lipid
464 changes in LacQ140 mice occurred at 9 months, with few changes detected at 12 months. Similarly, Langfelder et al.
465 found a greater number of differentially expressed genes at 6 months compared to 10 months in zQ175 mice [39]. This

466 suggests that in the mouse brain, adverse responses to mHTT oscillate or go through waves of degeneration and
467 regeneration. Therefore, to appreciate any benefits afforded by m*Htt* lowering, frequent or continuous monitoring
468 should be conducted.

469 In this study, mass spectrometry of lipids identified numerous alterations in LacQ140 striatum, many of
470 which were prevented with modest m*Htt* lowering. To our surprise, lipidomic analysis showed that LacQ140 mice had
471 increased levels in species of glycerophospholipids PI and PS starting at 6 months and progressing to a significant
472 change in the PI and PS subclass level at 9 months. Proteomics in Q140 synaptosomes revealed changes in proteins
473 that regulate PI levels including PKC signaling and PIP2 hydrolysis, changes in two isoforms of DGKs, and alterations in
474 one of the rate-limiting enzymes in PI synthesis (CDS2) [33] all of which impact PI levels [95]. Transcriptomic profiling of
475 LacQ140 mice also showed a plethora of altered mRNA levels for enzymes that impact PI and PIPs **(Fig. 6c and f;**
476 **Additional Files 2 and 3**). Normally found on the inner leaflet of the plasma membrane, PS can be externalized by
477 apoptotic cells to signal for their demolition [103] and in neuronal synapses, externalized PS signals to microglia for
478 synaptic pruning [104].Microglial activation occurs in HD post-mortem brain [105] and increased pruning by microglia is
479 hypothesized to contribute to synaptic loss in R6/2 HD striatum [106] and in zQ175 and BACHD mice, as well as in HD
480 brain [107]. An overall increase in PS could inadvertently mark synapses or myelin [108] for engulfment by microglia. The
481 ratio of PS to PE impacts autophagy [109] which may in turn impair mHTT removal [110,111]. Both PI and PS are abundant in
482 astrocytes as well as neurons [112] so it is unclear which cell type(s) is producing the changes in these lipids. We cannot
483 rule out the possibility that lipid changes are due to altered cellular composition of the brain.

484 Changes in white matter detected through imaging are one of the first signs of disease in people with HD
485 (PwHD) [113–127]. Morphometric studies of postmortem HD brains showed reduced cross-sectional area of white matter
486 as well as gray matter atrophy [128,129]. In HD post-mortem brain tissue, a dramatic shift in the profile of various
487 sphingolipids including Cer, SM, hexosylceramides, and sulfatides occurred [51]. Here, we demonstrate in the striatum
488 of 9-month-old LacQ140 mice significant reductions (compared to WT mice) of relative levels of total lipids and the
489 lipid subclasses SM and Cer, and three individual species of Hex1Cer, all important for myelin [130]. Our data are in
490 alignment with data from R6/1 mice showing changes in cerebroside and sulfatide levels [131], from the R6/2 mouse
491 model showing reductions in components of the sphingolipid biosynthesis pathway [45], and findings in a transgenic
492 sheep model OVT73, similarly showing decreased levels of numerous species of SM [132]. A salient finding was a

493 profound reduction in LacQ140 striatum of the low abundance signaling lipid MGDG, which regulates
494 oligodendrocyte differentiation [89]. MGDG is considered a marker of myelination and stimulates PKC-alpha activity in
495 oligodendrocytes to support process formation [90]. We previously reported reduced levels of MGDG in subcellular
496 fractions of Q175/Q7 HD striatum at 2 and 6 months [47]. Crucially, in LacQ140 mice, lowering m*Htt* improved the loss
497 of SM and MGDG suggesting protection against white matter pathology.

498 Altered oligodendrocyte differentiation or survival due to direct effects of mHTT protein on transcription in
499 the nucleus may account for many of the lipid changes we observed. RNA transcripts of genes important for
500 oligodendrocyte differentiation and myelin sphingolipid biosynthesis were altered in LacQ140 mice. The transcription
501 factor *Tcf7l2*, which was lower at 6 months in LacQ140 mice, was recently implicated in altered myelin formation in
502 R6/2 and Q175 mice [133]. The basic helix-loop-helix transcription factor *Olig1*, which was increased at 12 months in
503 LacQ140 mice compared to WT, is important for commitment of cells to CNS oligodendrocyte identity [134]. Critically,
504 Lim et al. presented evidence showing abnormal oligodendrocyte maturation in multiple HD postmortem brain
505 regions, as well as R6/2 brain, with single-nucleus RNAseq showing changes in *OLIG1* and *OLIG2* [135]. Altered levels of
506 myelin transcripts were found in human embryonic stem cells differentiated along an oligodendrocyte pathway [136]
507 and an epigenic etiology for changes in myelin gene expression in human oligodendrocyte precursors that was
508 blocked by inactivation of m*HTT* allele was described [137].

509 Changes in particular enzyme levels that regulate lipid biosynthesis that were changed at the transcriptional
510 level in LacQ140 mice can have dire consequences and result directly in myelin defects. Both *Ugt8a* and *Fa2h* mRNA
511 were lower in the striatum of LacQ140 mice; *Ugt8a* mRNA levels were protected by m*Htt* lowering at 6 months, but
512 *Fa2h* mRNA was not. Work by others showed that mice deficient in the *Ugt8a* gene exhibited abnormal myelin
513 maturation and structure [138,139]. In humans, mutations in FA2H are associated with leukodystrophy and hereditary
514 spastic paraplegia type SPG35 [140,141] highlighting the importance of hydroxylated sphingolipids in myelin integrity.
515 Adult *Fa2h*-deficient mice have normal oligodendrocyte differentiation with normal appearing myelin that later
516 degenerates, showing "splitting of lammelae" by 18 months [142]. This is similar to the Ki140CAG mouse model [143]
517 where myelin appears to be quite normal into early adulthood, but then may start to degenerate with disease
518 progression.

519 Although transcriptional deregulation clearly impacts lipid modifying enzymes, levels of myelin-related lipids
520 could be caused by an interaction of mHTT with oligodendrocyte membranes or a be a consequence of Wallerian
521 degeneration of cortical-striatal axons of the neurons. Interestingly, the presence of SM increased permeabilization
522 of monolayers by mHTT *in vitro* [53], suggesting mHTT could have particular effects on myelin lipids. Crucially, mHTT
523 was localized within myelin sheaths using immunogold EM in 9-month-old Q175 striatum [80]. Moreover, mHTT can be
524 secreted by neurons in culture and in the brain as a soluble free form [144]. We speculate that mHTT could insert
525 directly into myelin bilayers to disrupt myelin architecture.
526 Observing white matter changes in animal models has been challenging. White matter loss was reported in
527 R6/1 mice [145], and changes in myelination have been described in Yac128 [146,147] and HdhQ250 mice [148], but
528 experiments designed to look for white matter changes in the Q150 HD mouse model showed brain atrophy but no
529 white matter abnormalities [149]. A recent imaging study of OVT73 sheep brain reported changes in diffusivity in the
530 internal capsule at 9-10 years, suggesting changes in white matter microstructure [150]. Our biochemical experiments
531 here show that mHTT effects on striatal lipid homeostasis in HD mouse models are complex. We and others have
532 reported lipidomic and metabolomic studies on knock-in Q140/Q140 HD mice at single time points [48] and Q111 HD
533 mice [44] but did not observe loss of lipids important for white matter. Curiously, the lipid differences in LacQ140 mice
534 measured at 9 months disappeared at 12 months suggesting that, even in the absence of m*Htt* lowering, the mouse
535 brain insulted with mHTT attempts to heal itself and succeeds at some level. Consistent with our lipidomic findings, a
536 longitudinal imaging study over 18 months showed transient changes in diffusivity/fractional anisotropy of corpus
537 collosum in Q140 mouse brain [143]. These results echo imaging data from presymptomatic PwHD suggesting
538 attempted remyelination [151]. Hence, if HD mouse models undergo a series of degeneration and regeneration cycles,
539 observations at one or two time points may be misleading. By 12 months, although changes at the lipid subclass level
540 were annulled in the LacQ140 mice, a detailed analysis of the individual lipid species comprising these subclasses
541 shows a shift in species within each subclass. The altered composition of subclasses may alter function, weaken HD
542 brains, or predispose them to further stress. In fact, the behavioral analyses of these mice which showed loss of
543 protection by mHTT lowering at 12 months [59] indicates that although levels of lipids by subclasses are restored at 12
544 months (with or without mHTT lowering), the changes in individual lipid species which compose each subclasses
545 correlate with behavioral degradation.

546 Not all lipid changes were reversed with m*Htt* lowering. Consistent with metabolic defects in HD, here we
547 report reduced levels of species of TG, glycerolipid molecules used for energy storage which can be metabolized by
548 mitochondria, in LacQ140 compared to WT. Of note, reductions in species of TG were not reversed by m*Htt* lowering.
549 Interestingly, the LacQ140 mice exhibited reciprocal changes in the two biosynthetic enzymes *Dgat1* and *Dgat2* at
550 the transcriptional level, suggesting the ability to store energy may arise in part from this variation.
551
552 **CONCLUSIONS**
553 Collectively, our studies advocate early lowering of m*HTT* for greatest benefit, and in this context, modest
554 lowering is sufficient to delay some protein and lipid changes. Furthermore, our work shows readily detectable but
555 transient changes in lipids highly enriched in myelin, consistent with possible white matter damage and regeneration
556 occurring in the LacQ140 mouse model.

557 **LIST OF ABBREVIATIONS**

558 HD: Huntington's disease

559 HTT: Huntingtin

560 ASOs: Antisense oligonucleotide

561 miRNA: MicroRNA

562 shRNA: Short hairpin RNA

563 DARPP32: Dopamine And CAMP-Regulated Neuronal Phosphoprotein 32

564 PDE10A: Phosphodiesterase 10A

565 SCN4B: Sodium Voltage-Gated Channel Beta Subunit 4

566 ATP5A: ATP Synthase F1 Subunit Alpha

567 PIP: Phosphatidylinositol phosphate

568 IPTG: Isopropyl b-D-1-thiogalactopyranoside

569 Poly-Q: Polyglutamine

570 GFAP: Glial fibrillary acidic protein

571 LC-MS: Liquid chromatography – mass spectrometry

572 PS: Phosphatidylserine

573 PI: Phosphatidylinositol

574 BisMePA: Bis-methyl phosphatidic acid

575 PKC: Protein kinase C

576 SM: Sphingomyelin

577 Cer: Ceramide

578 MGDG: Monogalactosyldiacylglycerol

579 Hex1Cer: Monohexosylceramide

580 GalCer: Galactosylceramide

581 GlcCer: Glucosylceramide

582 TG: Triacylglycerol

583 GO BP: Gene Ontology Biological Processes

584 GSEA: Gene Set Enrichment Analysis

585 Ugt8a: UDP-Galactose Ceramide Galactosyltransferase

586 Fa2h: Fatty acid 2-hydroxylase

587 **DECLARATIONS**

588 **Ethics approval and consent to participate**

589 Mice were housed at Psychogenics (Paramus, NJ) and all treatments and procedures were conducted with oversight
590 by Psychogenics Institutional Animal Care and Use Committee.

591 **Consent for publication**

592 Not applicable

593 **Availability of data and materials**

594 All datasets generated are included in this article and can be found in **Additional Files 1-5.** RNA-sequencing data
595 analyzed is available at Gene Expression Omnibus (GEO) accession number GSE156236.

596 **Competing interests**

597 KBK-G spouse owns less than 0.1% stock in the following companies: Advanced Microdevices, Aveo Pharmaceuticals,
598 Inc, Boston Scientific Corporation, Bristol-Myers Squibb Company, Cisco Systems, Inc., Fate Therapeutics, GE
599 Healthcare Life Sciences, Generex Biotechnology Corporation, Idera Pharmaceuticals, Inc., Nante Health,
600 Neurometrics, Inc., NuGenerex, Repligen Corporation, Sesen Bio, Inc., T2 Biosystems, and Vericel Corporation.
601 Other authors have no declarations of interest.

602 **Funding**

603 This work was funded by CHDI Foundation, Inc., a nonprofit biomedical research organization exclusively dedicated
604 to developing therapeutics that will substantially improve the lives of HD-affected individuals, the Dake family fund
605 to MD and KBK-G, and NIH 1S10RR023594S10 to MD.

606 **Authors' contributions**

607 KKG, MD, and DM conceived experimental plan and wrote manuscript. KS performed all lipidomics and
608 bioinformatics and wrote manuscript, ES performed protein chemistry analysis and wrote manuscript, AB aided in
609 the experimental plan and edited manuscript, CS and SL performed subcellular fractionations.

610 **Acknowledgements**

611 The authors would like to acknowledge the Dake family for their support.

612 **REFERENCES**

613 1. Difiglia, M. *et al.* Huntingtin Is a Cytoplasmic Protein Associated with Vesicles in Human and Rat Brain Neurons.
614 *Neuron* **14**, 1075–1081 (1995).
615 2. Sharp, A. H. *et al.* Widespread expression of Huntington's disease gene (IT15) protein product. *Neuron* **14**,
616 1065–74 (1995).
617 3. Caviston, J. P. & Holzbaur, E. L. F. Huntingtin as an essential integrator of intracellular vesicular trafficking.
618 *Trends in Cell Biology* **19**, 147–155 (2009).
619 4. Gao, R. *et al.* Mutant huntingtin impairs PNKP and ATXN3, disrupting DNA repair and transcription. *eLife* (2019)
620 doi:10.7554/eLife.42988.001.
621 5. Saudou, F. & Humbert, S. The Biology of Huntingtin. *Neuron* **89**, 910–926 (2016).
622 6. Barron, J. C., Hurley, E. P. & Parsons, M. P. Huntingtin and the Synapse. *Front Cell Neurosci* **15**, 689332 (2021).
623 7. Duyao, M. P. *et al.* Inactivation of the mouse Huntington's disease gene homolog Hdh. *Science* **269**, 407–10
624 (1995).
625 8. McKinstry, S. U. *et al.* Huntingtin is required for normal excitatory synapse development in cortical and striatal
626 circuits. *J Neurosci* **34**, 9455–72 (2014).
627 9. Nasir, J. *et al.* Targeted disruption of the Huntington's disease gene results in embryonic lethality and
628 behavioral and morphological changes in heterozygotes. *Cell* **81**, 811–23 (1995).
629 10. O'Kusky, J. R., Nasir, J., Cicchetti, F., Parent, A. & Hayden, M. R. Neuronal degeneration in the basal ganglia and
630 loss of pallido-subthalamic synapses in mice with targeted disruption of the Huntington's disease gene. *Brain*
631 *Res* **818**, 468–79 (1999).
632 11. Zeitlin, S., Liu2, J.-P., Chapman3, D. L., Papaioannou, V. E. & Efstratiadis, A. Increased apoptosis and early
633 embryonic lethality in mice nullizygou s for the Huntington 's disease gene homologu e. *Nature Genetics* **11**,
634 155–163 (1995).
635 12. Nopoulos, P. C. Huntington disease: a single-gene degenerative disorder of the striatum. *Dialogues Clin*
636 *Neurosci* **18**, 91–8 (2016).
637 13. Petersen, A. & Bjorkqvist, M. Hypothalamic-endocrine aspects in Huntington's disease. *Eur J Neurosci* **24**, 961–7
638 (2006).
639 14. Tabrizi, S. J., Ghosh, R. & Leavitt, B. R. Huntingtin Lowering Strategies for Disease Modification in Huntington's
640 Disease. *Neuron* **101**, 801–819 (2019).
641 15. Caron, N. S., Dorsey, E. R. & Hayden, M. R. Therapeutic approaches to huntington disease: From the bench to
642 the clinic. *Nature Reviews Drug Discovery* **17**, 729–750 (2018).
643 16. Keller, C. G. *et al.* An orally available, brain penetrant, small molecule lowers huntingtin levels by enhancing
644 pseudoexon inclusion. *Nature Communications* **13**, (2022).
645 17. Zeitler, B. *et al.* Allele-selective transcriptional repression of mutant HTT for the treatment of Huntington's
646 disease. *Nature Medicine* **25**, 1131–1142 (2019).
647 18. Alterman, J. F. *et al.* A divalent siRNA chemical scaffold for potent and sustained modulation of gene expression
648 throughout the central nervous system. *Nature Biotechnology* **37**, 884–894 (2019).
649 19. Keeler, A. M. *et al.* Cellular Analysis of Silencing the Huntington's Disease Gene Using AAV9 Mediated Delivery
650 of Artificial Micro RNA into the Striatum of Q140/Q140 Mice. *J Huntingtons Dis* **5**, 239–248 (2016).
651 20. McBride, J. L. *et al.* Preclinical safety of RNAi-mediated HTT suppression in the rhesus macaque as a potential
652 therapy for Huntington's disease. *Mol Ther* **19**, 2152–62 (2011).
653 21. Boudreau, R. L. *et al.* Nonallele-specific silencing of mutant and wild-type huntingtin demonstrates therapeutic
654 efficacy in Huntington's disease mice. *Mol Ther* **17**, 1053–63 (2009).
655 22. Datson, N. A. *et al.* The expanded CAG repeat in the huntingtin gene as target for therapeutic RNA modulation
656 throughout the HD mouse brain. *PLoS One* **12**, e0171127 (2017).
657 23. DiFiglia, M. *et al.* Therapeutic silencing of mutant huntingtin with siRNA attenuates striatal and cortical
658 neuropathology and behavioral deficits. *Proc Natl Acad Sci U S A* **104**, 17204–9 (2007).
659 24. Drouet, V. *et al.* Sustained effects of nonallele-specific Huntingtin silencing. *Ann Neurol* **65**, 276–85 (2009).
660 25. Kordasiewicz, H. B. *et al.* Sustained Therapeutic Reversal of Huntington's Disease by Transient Repression of
661 Huntingtin Synthesis. *Neuron* **74**, 1031–1044 (2012).
662 26. Rodriguez-Lebron, E., Denovan-Wright, E. M., Nash, K., Lewin, A. S. & Mandel, R. J. Intrastriatal rAAV-mediated
663 delivery of anti-huntingtin shRNAs induces partial reversal of disease progression in R6/1 Huntington's disease
664 transgenic mice. *Mol Ther* **12**, 618–33 (2005).

665 27. Stanek, L. M. *et al.* Antisense oligonucleotide-mediated correction of transcriptional dysregulation is correlated
666 with behavioral benefits in the YAC128 mouse model of Huntington's disease. *J Huntingtons Dis* **2**, 217–28
667 (2013).
668 28. Stanek, L. M. *et al.* Silencing mutant huntingtin by adeno-associated virus-mediated RNA interference
669 ameliorates disease manifestations in the YAC128 mouse model of Huntington's disease. *Hum Gene Ther* **25**,
670 461–74 (2014).
671 29. Leavitt, B. R., Kordasiewicz, H. B. & Schobel, S. A. Huntingtin-Lowering Therapies for Huntington Disease: A
672 Review of the Evidence of Potential Benefits and Risks. *JAMA Neurol* **77**, 764–772 (2020).
673 30. Dragatsis, I., Levine, M. S. & Zeitlin, S. Inactivation of Hdh in the brain and testis results in progressive
674 neurodegeneration and sterility in mice. *Nature Genetics* **26**, 300–306 (2000).
675 31. Mehler, M. F. *et al.* Loss-of-Huntingtin in Medial and Lateral Ganglionic Lineages Differentially Disrupts Regional
676 Interneuron and Projection Neuron Subtypes and Promotes Huntington's Disease-Associated Behavioral,
677 Cellular, and Pathological Hallmarks. *J Neurosci* **39**, 1892–1909 (2019).
678 32. Bibb, J. A. *et al.* Severe deficiencies in dopamine signaling in presymptomatic Huntington's disease mice. *Proc*
679 *Natl Acad Sci U S A* **97**, 6809–14 (2000).
680 33. Sapp, E. *et al.* Protein changes in synaptosomes of Huntington's disease knock-in mice are dependent on age
681 and brain region. *Neurobiology of Disease* **141**, (2020).
682 34. Skotte, N. H. *et al.* Integrative Characterization of the R6/2 Mouse Model of Huntington's Disease Reveals
683 Dysfunctional Astrocyte Metabolism. *Cell Reports* **23**, 2211–2224 (2018).
684 35. Bertoglio, D. *et al.* Development of a ligand for in vivo imaging of mutant huntingtin in Huntington's disease.
685 *Science Translational Medicine* **14**, 3682 (2022).
686 36. Mehta, S. R. *et al.* Human Huntington's Disease iPSC-Derived Cortical Neurons Display Altered Transcriptomics,
687 Morphology, and Maturation. *Cell Rep* **25**, 1081-1096 e6 (2018).
688 37. Oyama, F. *et al.* Sodium channel beta4 subunit: down-regulation and possible involvement in neuritic
689 degeneration in Huntington's disease transgenic mice. *J Neurochem* **98**, 518–29 (2006).
690 38. Agrawal, S. & Fox, J. H. Novel proteomic changes in brain mitochondria provide insights into mitochondrial
691 dysfunction in mouse models of Huntington's disease. *Mitochondrion* **47**, 318–329 (2019).
692 39. Langfelder, P. *et al.* Integrated genomics and proteomics define huntingtin CAG length-dependent networks in
693 mice. *Nature Neuroscience* **19**, 623–633 (2016).
694 40. McQuade, L. R. *et al.* Proteomics of Huntington's disease-affected human embryonic stem cells reveals an
695 evolving pathology involving mitochondrial dysfunction and metabolic disturbances. *J Proteome Res* **13**, 5648–
696 59 (2014).
697 41. Kegel, K. B. *et al.* Polyglutamine expansion in huntingtin increases its insertion into lipid bilayers. *Biochemical*
698 *and Biophysical Research Communications* **387**, 472–475 (2009).
699 42. Hyuk Yoon, J. *et al.* Brain lipidomics: From functional landscape to clinical significance. *Science Advances* **8**, 9317
700 (2022).
701 43. Harayama, T. & Riezman, H. Understanding the diversity of membrane lipid composition. *Nature Reviews*
702 *Molecular Cell Biology* **19**, 281–296 (2018).
703 44. Carroll, J. B. *et al.* HdhQ111 mice exhibit tissue specific metabolite profiles that include striatal lipid
704 accumulation. *PLoS ONE* **10**, (2015).
705 45. Di Pardo, A. *et al.* De novo synthesis of sphingolipids is defective in experimental models of Huntington's
706 disease. *Frontiers in Neuroscience* **11**, (2017).
707 46. Farzana, F. *et al.* Longitudinal spatial mapping of lipid metabolites reveals pre-symptomatic changes in the
708 hippocampi of Huntington's disease transgenic mice. *Neurobiology of Disease* **176**, 105933 (2023).
709 47. Iuliano, M. *et al.* Disposition of Proteins and Lipids in Synaptic Membrane Compartments Is Altered in Q175/Q7
710 Huntington's Disease Mouse Striatum. *Frontiers in Synaptic Neuroscience* **13**, (2021).
711 48. Vodicka, P. *et al.* Mass Spectrometry Analysis of Wild-Type and Knock-in Q140/Q140 Huntington's Disease
712 Mouse Brains Reveals Changes in Glycerophospholipids Including Alterations in Phosphatidic Acid and Lyso-
713 Phosphatidic Acid. *Journal of Huntington's Disease* **4**, 187–201 (2015).
714 49. Hunter, M., Demarais, N. J., Faull, R. L. M., Grey, A. C. & Curtis, M. A. Subventricular zone lipidomic architecture
715 loss in Huntington's disease. *Journal of Neurochemistry* **146**, 613–630 (2018).

716 50. Hunter, M., Demarais, N. J., Faull, R. L. M., Grey, A. C. & Curtis, M. A. An imaging mass spectrometry atlas of
717 lipids in the human neurologically normal and Huntington's disease caudate nucleus. *Journal of Neurochemistry*
718 **157**, 2158–2172 (2021).
719 51. Phillips, G. *et al.* The long and the short of Huntington's disease: how the sphingolipid profile is shifted in the
720 caudate of advanced clinical cases. *Brain Communications* **4**, (2022).
721 52. Kegel, K. B. *et al.* Polyglutamine expansion in huntingtin alters its interaction with phospholipids. *Journal of*
722 *Neurochemistry* **110**, 1585–1597 (2009).
723 53. Chaibva, M. *et al.* Sphingomyelin and GM1 Influence Huntingtin Binding to, Disruptionof, and Aggregation on
724 Lipid Membranes. *ACS Omega* **3**, 273–285 (2018).
725 54. Southwell, A. L. *et al.* Huntingtin suppression restores cognitive function in a mouse model of Huntington's
726 disease. *Science Translational Medicine* **10**, 3959 (2018).
727 55. Caron, N. S. *et al.* Cerebrospinal fluid mutant huntingtin is a biomarker for huntingtin lowering in the striatum of
728 Huntington disease mice. *Neurobiology of Disease* **166**, (2022).
729 56. Southwell, A. L. *et al.* Ultrasensitive measurement of huntingtin protein in cerebrospinal fluid demonstrates
730 increase with Huntington disease stage and decrease following brain huntingtin suppression. *Sci Rep* **5**, 12166
731 (2015).
732 57. Coffey, S. R. *et al.* Huntingtin lowering reduces somatic instability at CAG-expanded loci. *bioRxiv* (2020)
733 doi:10.1101/2020.07.23.218347.
734 58. Cronin, C. A., Gluba, W. & Scrable, H. The lac operator-repressor system is functional in the mouse. *Genes Dev*
735 **15**, 1506–17 (2001).
736 59. Marchionini, D. M. *et al.* Benefits of global mutant huntingtin lowering diminish over time in a Huntington's
737 disease mouse model. *JCI Insight* **7**, (2022).
738 60. Scrable, H. Say when: reversible control of gene expression in the mouse by lac. *Semin Cell Dev Biol* **13**, 109–19
739 (2002).
740 61. Landles, C. *et al.* Proteolysis of mutant huntingtin produces an exon 1 fragment that accumulates as an
741 aggregated protein in neuronal nuclei in Huntington disease. *J Biol Chem* **285**, 8808–23 (2010).
742 62. Scherzinger, E. *et al.* Huntingtin-encoded polyglutamine expansions form amyloid-like protein aggregates in
743 vitro and in vivo. *Cell* **90**, 549–58 (1997).
744 63. Weiss, A. *et al.* Sensitive biochemical aggregate detection reveals aggregation onset before symptom
745 development in cellular and murine models of Huntington's disease. *J Neurochem* **104**, 846–58 (2008).
746 64. Breitkopf, S. B. *et al.* A relative quantitative positive/negative ion switching method for untargeted lipidomics
747 via high resolution LC-MS/MS from any biological source. *Metabolomics* **13**, (2017).
748 65. Matyash, V., Liebisch, G., Kurzchalia, T. V., Shevchenko, A. & Schwudke, D. Lipid extraction by methyl-terf-butyl
749 ether for high-throughput lipidomics. *Journal of Lipid Research* **49**, 1137–1146 (2008).
750 66. Liebisch, G. *et al.* Update on LIPID MAPS classification, nomenclature, and shorthand notation for MS-derived
751 lipid structures. *Journal of Lipid Research* **61**, 1539–1555 (2020).
752 67. Reza, S., Ugorski, M. & Suchański, J. Glucosylceramide and galactosylceramide, small glycosphingolipids with
753 significant impact on health and disease. *Glycobiology* **31**, 1416–1434 (2021).
754 68. Koelmel, J. P., Ulmer, C. Z., Jones, C. M., Yost, R. A. & Bowden, J. A. Common cases of improper lipid annotation
755 using high-resolution tandem mass spectrometry data and corresponding limitations in biological
756 interpretation. *Biochimica et Biophysica Acta - Molecular and Cell Biology of Lipids* **1862**, 766–770 (2017).
757 69. Gu, Z. Complex heatmap visualization. *iMeta* (2022) doi:10.1002/imt2.43.
758 70. Love, M. I., Huber, W. & Anders, S. Moderated estimation of fold change and dispersion for RNA-seq data with
759 DESeq2. *Genome Biology* **15**, 550 (2014).
760 71. Benjamini, Y. & Hochberg, Y. Controlling the False Discovery Rate: A Practical and Powerful Approach to
761 Multiple Testing. *Journal of the Royal Statistical Society: Series B (Methodological)* **57**, 289–300 (1995).
762 72. Kegel, K. B. *et al.* Huntingtin is present in the nucleus, interacts with the transcriptional corepressor C-terminal
763 binding protein, and represses transcription. *J Biol Chem* **277**, 7466–76 (2002).
764 73. Sapp, E. *et al.* Huntingtin Localization in Brains of Normal and Huntington's Disease Patients. *Annals of*
765 *Neurology* **42**, 604–612 (1997).
766 74. Tousley, A. *et al.* Huntingtin associates with the actin cytoskeleton and alpha-actinin isoforms to influence
767 stimulus dependent morphology changes. *PLoS One* **14**, e0212337 (2019).

768 75. Trettel, F. Dominant phenotypes produced by the HD mutation in STHdhQ111 striatal cells. *Human Molecular*
769 *Genetics* **9**, 2799–2809 (2000).
770 76. Seong, I. S. *et al.* Huntingtin facilitates polycomb repressive complex 2. *Human Molecular Genetics* **19**, 573–583
771 (2010).
772 77. Ko, J., Ou, S. & Patterson, P. H. New anti-huntingtin monoclonal antibodies: implications for huntingtin
773 conformation and its binding proteins. *Brain Res Bull* **56**, 319–329 (2001).
774 78. Legleiter, J. *et al.* Monoclonal Antibodies Recognize Distinct Conformational Epitopes Formed by Polyglutamine
775 in a Mutant Huntingtin Fragment *. *Journal of Biological Chemistry* **284**, 21647–21658 (2009).
776 79. Miller, J. *et al.* Identifying polyglutamine protein species in situ that best predict neurodegeneration. *Nature*
777 *Chemical Biology* **7**, 925–934 (2011).
778 80. Ko, J. *et al.* Identification of distinct conformations associated with monomers and fibril assemblies of mutant
779 huntingtin. *Human Molecular Genetics* **27**, 2330–2343 (2018).
780 81. Sathasivam, K. *et al.* Identical oligomeric and fibrillar structures captured from the brains of R6/2 and knock-in
781 mouse models of Huntington's disease. *Human Molecular Genetics* **19**, 65–78 (2010).
782 82. Kegel, K. B. *et al.* Huntingtin Expression Stimulates Endosomal-Lysosomal Activity, Endosome Tubulation, and
783 Autophagy. *Journal of Neuroscience* (2000).
784 83. Vodicka, P. *et al.* Assessment of chloroquine treatment for modulating autophagy flux in brain of WT and HD
785 mice. *J Huntingtons Dis* **3**, 159–74 (2014).
786 84. Gu, M. *et al.* Mitochondrial defect in Huntington's disease caudate nucleus. *Ann Neurol* **39**, 385–9 (1996).
787 85. Berridge, M. J. The Inositol Trisphosphate/Calcium Signaling Pathway in Health and Disease. *Physiological*
788 *Reviews* **96**, 1261–1296 (2016).
789 86. Hirt, U. A. & Leist, M. Rapid, noninflammatory and PS-dependent phagocytic clearance of necrotic cells. *Cell*
790 *Death Differ* **10**, 1156–1164 (2003).
791 87. Kim, H.-Y., Huang, B. X. & Spector, A. A. Phosphatidylserine in the brain: Metabolism and function. *Progress in*
792 *Lipid Research* **56**, 1–18 (2014).
793 88. Chrast, R., Saher, G., Nave, K. A. & Verheijen, M. H. G. Lipid metabolism in myelinating glial cells: Lessons from
794 human inherited disorders and mouse models. *Journal of Lipid Research* **52**, 419–434 (2011).
795 89. Inoue, T., Deshmukh, D. S. & Pieringer, R. A. The Association of the Galactosyl Diglycerides of Brain with
796 Myelination. *Journal of Biological Chemistry* **246**, 5688–5694 (1971).
797 90. Schmidt-Schultz, T. & Althaus, H. H. Monogalactosyl Diglyceride, a Marker for Myelination, Activates
798 Oligodendroglial Protein Kinase C. *Journal of Neurochemistry* **62**, 1578–1585 (1994).
799 91. Vanier, M. T. & Svennerholm, L. Chemical pathology of Krabbe's disease. III. Ceramide-hexosides and
800 gangliosides of brain. *Acta Paediatr Scand* **64**, 641–648 (1975).
801 92. Schmitt, S., Cantuti Castelvetri, L. & Simons, M. Metabolism and functions of lipids in myelin. *Biochimica et*
802 *Biophysica Acta - Molecular and Cell Biology of Lipids* **1851**, 999–1005 (2015).
803 93. Subramanian, A. *et al.* Gene set enrichment analysis: A knowledge-based approach for interpreting genome-
804 wide expression profiles. *Proceedings of the National Academy of Sciences* (2005).
805 94. Wu, T. *et al.* clusterProfiler 4.0: A universal enrichment tool for interpreting omics data. *The Innovation* **2**,
806 (2021).
807 95. Blunsom, N. J. & Cockcroft, S. CDP-Diacylglycerol Synthases (CDS): Gateway to Phosphatidylinositol and
808 Cardiolipin Synthesis. *Frontiers in Cell and Developmental Biology* **8**, (2020).
809 96. Harris, C. A. *et al.* DGAT enzymes are required for triacylglycerol synthesis and lipid droplets in adipocytes [S].
810 *Journal of Lipid Research* **52**, 657–667 (2011).
811 97. van der Bijl, P., Strous, G. J., Lopes-Cardozo, M., Thomas-Oates, J. & van Meer, G. Synthesis of non-hydroxy-
812 galactosylceramides and galactosyldiglycerides by hydroxy-ceramide galactosyltransferase. *Biochem J* **317**, 589–
813 597 (1996).
814 98. Alderson, N. L., Maldonado, E. N., Kern, M. J., Bhat, N. R. & Hama, H. FA2H-dependent fatty acid 2-
815 hydroxylation in postnatal mouse brain. *Journal of Lipid Research* **47**, 2772–2780 (2006).
816 99. Diaz-Hernandez, M. *et al.* Full motor recovery despite striatal neuron loss and formation of irreversible amyloid-
817 like inclusions in a conditional mouse model of Huntington's disease. *J Neurosci* **25**, 9773–81 (2005).
818 100. Fox, L. M. *et al.* Huntington's Disease Pathogenesis Is Modified In Vivo by Alfy/Wdfy3 and Selective
819 Macroautophagy. *Neuron* **105**, 813-821.e6 (2020).

101. Wheeler, V. C. Long glutamine tracts cause nuclear localization of a novel form of huntingtin in medium spiny striatal neurons in HdhQ92 and HdhQ111 knock-in mice. *Human Molecular Genetics* **9**, 503–513 (2000).
102. Kaganovich, D., Kopito, R. & Frydman, J. Misfolded proteins partition between two distinct quality control compartments. *Nature* **454**, 1088–95 (2008).
103. Williamson, P. & Schlegel, R. A. Transbilayer phospholipid movement and the clearance of apoptotic cells. *Biochim Biophys Acta* **1585**, 53–63 (2002).
104. Scott-Hewitt, N. *et al.* Local externalization of phosphatidylserine mediates developmental synaptic pruning by microglia. *The EMBO Journal* **39**, (2020).
105. Sapp, E. *et al.* Early and progressive accumulation of reactive microglia in the Huntington disease brain. *J Neuropathol Exp Neurol* **60**, 161–72 (2001).
106. Savage, J. C. *et al.* Microglial physiological properties and interactions with synapses are altered at presymptomatic stages in a mouse model of Huntington's disease pathology. *J Neuroinflammation* **17**, 98 (2020).
107. Wilton, D. *et al.* Microglia Mediate Early Corticostriatal Synapse Loss and Cognitive Dysfunction in Huntington's Disease Through Complement-Dependent Mechanisms. *bioRxiv* (2021) doi:10.1101/2021.12.03.471180.
108. Djannatian, M. *et al.* Myelination generates aberrant ultrastructure that is resolved by microglia. *Journal of Cell Biology* **222**, (2023).
109. Polyansky, A. *et al.* Phospholipid imbalance impairs autophagosome completion. *The EMBO Journal* (2022) doi:10.15252/embj.2022110771.
110. Qin, Z. H. *et al.* Autophagy regulates the processing of amino terminal huntingtin fragments. *Hum Mol Genet* **12**, 3231–44 (2003).
111. Yamamoto, A., Cremona, M. L. & Rothman, J. E. Autophagy-mediated clearance of huntingtin aggregates triggered by the insulin-signaling pathway. *Journal of Cell Biology* **172**, 719–731 (2006).
112. Fitzner, D. *et al.* Cell-Type- and Brain-Region-Resolved Mouse Brain Lipidome. *Cell Reports* **32**, (2020).
113. Bourbon-Teles, J. *et al.* Myelin Breakdown in Human Huntington's Disease: Multi-Modal Evidence from Diffusion MRI and Quantitative Magnetization Transfer. *Neuroscience* **403**, 79–92 (2019).
114. Di Paola, M. *et al.* Multimodal MRI analysis of the corpus callosum reveals white matter differences in presymptomatic and early Huntington's disease. *Cereb Cortex* **22**, 2858–66 (2012).
115. Faria, A. V. *et al.* Linking white matter and deep gray matter alterations in premanifest Huntington disease. *Neuroimage Clin* **11**, 450–460 (2016).
116. Hobbs, N. Z. *et al.* The progression of regional atrophy in premanifest and early Huntington's disease: a longitudinal voxel-based morphometry study. *J Neurol Neurosurg Psychiatry* **81**, 756–63 (2010).
117. Matsui, J. T. *et al.* Prefrontal cortex white matter tracts in prodromal Huntington disease. *Hum Brain Mapp* **36**, 3717–32 (2015).
118. Odish, O. F. *et al.* Microstructural brain abnormalities in Huntington's disease: A two-year follow-up. *Hum Brain Mapp* **36**, 2061–74 (2015).
119. Oh, S. L. *et al.* Fixel-Based Analysis Effectively Identifies White Matter Tract Degeneration in Huntington's Disease. *Front Neurosci* **15**, 711651 (2021).
120. Paulsen, J. S. Functional imaging in Huntington's disease. *Exp Neurol* **216**, 272–7 (2009).
121. Paulsen, J. S. *et al.* Detection of Huntington's disease decades before diagnosis: the Predict-HD study. *J Neurol Neurosurg Psychiatry* **79**, 874–80 (2008).
122. Phillips, O. *et al.* Tractography of the corpus callosum in Huntington's disease. *PLoS One* **8**, e73280 (2013).
123. Poudel, G. R. *et al.* Longitudinal change in white matter microstructure in Huntington's disease: The IMAGE-HD study. *Neurobiol Dis* **74**, 406–12 (2015).
124. Rosas, H. D. *et al.* Diffusion tensor imaging in presymptomatic and early Huntington's disease: Selective white matter pathology and its relationship to clinical measures. *Movement Disorders* **21**, 1317–1325 (2006).
125. Singh, S., Mehta, H. & Fekete, R. Altered Fractional Anisotropy in Early Huntington's Disease. *Case Rep Neurol* **5**, 26–30 (2013).
126. Sweidan, W., Bao, F., Bozorgzad, N. S. & George, E. White and Gray Matter Abnormalities in Manifest Huntington's Disease: Cross-Sectional and Longitudinal Analysis. *J Neuroimaging* **30**, 351–358 (2020).
127. Tereshchenko, A. *et al.* Brain structure in juvenile-onset Huntington disease. *Neurology* **92**, e1939–e1947 (2019).

872 128. de la Monte, S. M., Vonsattel, J. P. & Richardson, E. P., Jr. Morphometric demonstration of atrophic changes in
873 the cerebral cortex, white matter, and neostriatum in Huntington's disease. *J Neuropathol Exp Neurol* **47**, 516–
874 25 (1988).
875 129. Vonsattel, J. P. & DiFiglia, M. Huntington disease. *J Neuropathol Exp Neurol* **57**, 369–84 (1998).
876 130. O'Brien, J. S. & Sampson, E. L. Lipid composition of the normal human brain: gray matter, white matter, and
877 myelin. *Journal of Lipid Research* **6**, 537–544 (1965).
878 131. Desplats, P. A. *et al.* Glycolipid and ganglioside metabolism imbalances in Huntington's disease. *Neurobiology of*
879 *Disease* **27**, 265–277 (2007).
880 132. Skene, D. J. *et al.* Metabolic profiling of presymptomatic Huntington's disease sheep reveals novel biomarkers.
881 *Scientific Reports* **7**, (2017).
882 133. Benraiss, A. *et al.* A TCF7L2-responsive suppression of both homeostatic and compensatory remyelination in
883 Huntington disease mice. *Cell Reports* **40**, 111291 (2022).
884 134. Dai, J., Bercury, K. K., Ahrendsen, J. T. & Macklin, W. B. Olig1 function is required for oligodendrocyte
885 differentiation in the mouse brain. *J Neurosci* **35**, 4386–402 (2015).
886 135. Lim, R. G. *et al.* Huntington disease oligodendrocyte maturation deficits revealed by single-nucleus RNAseq are
887 rescued by thiamine-biotin supplementation. *Nature Communications* **13**, 7791 (2022).
888 136. Osipovitch, M. *et al.* Human ESC-Derived Chimeric Mouse Models of Huntington's Disease Reveal Cell-Intrinsic
889 Defects in Glial Progenitor Cell Differentiation. *Cell Stem Cell* **24**, 107-122.e7 (2019).
890 137. Bardile, C. F. *et al.* Intrinsic mutant HTT-mediated defects in oligodendroglia cause myelination deficits and
891 behavioral abnormalities in Huntington disease. *Proceedings of the National Academy of Sciences of the United*
892 *States of America* **116**, 9622–9627 (2019).
893 138. Bosio, A., Binczek, E. & Stoffel, W. Functional breakdown of the lipid bilayer of the myelin membrane in central
894 and peripheral nervous system by disrupted galactocerebroside synthesis. *Proceedings of the National*
895 *Academy of Sciences* **93**, 13280–13285 (1996).
896 139. Coetzee, T. *et al.* Myelination in the Absence of Galactocerebroside and Sulfatide: Normal Structure with
897 Abnormal Function and Regional Instability. *Cell* **86**, 209–219 (1996).
898 140. Edvardson, S. *et al.* Mutations in the Fatty Acid 2-Hydroxylase Gene Are Associated with Leukodystrophy with
899 Spastic Paraparesis and Dystonia. *American Journal of Human Genetics* **83**, 643–648 (2008).
900 141. Rattay, T. W. *et al.* FAHN/SPG35: a narrow phenotypic spectrum across disease classifications. *Brain* **142**, 1561–
901 1572 (2019).
902 142. Zöller, I. *et al.* Absence of 2-hydroxylated sphingolipids is compatible with normal neural development but
903 causes late-onset axon and myelin sheath degeneration. *Journal of Neuroscience* **28**, 9741–9754 (2008).
904 143. Pérot, J. B. *et al.* Longitudinal multimodal MRI characterization of a knock-in mouse model of Huntington's
905 disease reveals early gray and white matter alterations. *Human molecular genetics* **31**, 3581–3596 (2022).
906 144. Caron, N. S. *et al.* Mutant Huntingtin Is Cleared from the Brain via Active Mechanisms in Huntington Disease. *J*
907 *Neurosci* **41**, 780–796 (2021).
908 145. Rattray, I. *et al.* Correlations of behavioral deficits with brain pathology assessed through longitudinal MRI and
909 histopathology in the R6/1 mouse model of Huntington's disease. *PLoS One* **8**, e84726 (2013).
910 146. Teo, R. T. Y. *et al.* Structural and molecular myelination deficits occur prior to neuronal loss in the YAC128 and
911 BACHD models of Huntington disease. *Human Molecular Genetics* **25**, 2621–2632 (2016).
912 147. Teo, R. T. Y. *et al.* Impaired Remyelination in a Mouse Model of Huntington Disease. *Molecular Neurobiology* **56**,
913 6873–6882 (2019).
914 148. Jin, J. *et al.* Early white matter abnormalities, progressive brain pathology and motor deficits in a novel knock-in
915 mouse model of Huntington's disease. *Human Molecular Genetics* **24**, 2508–2527 (2015).
916 149. Steventon, J. J. *et al.* Longitudinal in vivo MRI in a Huntington's disease mouse model: Global atrophy in the
917 absence of white matter microstructural damage. *Scientific Reports* **6**, (2016).
918 150. Taghian, T. *et al.* Brain Alterations in Aged OVT73 Sheep Model of Huntington's Disease: An MRI Based
919 Approach. *Journal of Huntington's Disease* 1–16 (2022) doi:10.3233/jhd-220526.
920 151. Phillips, O. *et al.* Deep white matter in Huntington's disease. *PLoS ONE* **9**, (2014).
921

Table 1. Overview of lipid subclass changes at 6, 9, and 12 months

		6-month-old mice			9-month-old mice			12-month-old mice		
Category	Subclass	Species detected	ANOVA p-val	Adj p-val (q), N =36	Species detected	ANOVA p-val	Adj p-val (q), N =24	Species detected	ANOVA p-val	Adj p-val (q), N =29
Glycerophos-pholipids	PC	134	0.7415	1	107	0.2928	0.3267	160	0.4243	0.4627
	PE	152	0.1975	1	154	0.0284*	0.0563	119	0.5653	0.5372
	PS	62	0.1171	1	58	**0.0014**	**0.0125**	25	0.46	0.4627
	PI	19	**0.0189**	0.7144	17	**0.0054**	**0.0168**	34	0.0086*	0.0338*
	MePC	17	0.9859	1	7	0.4901	0.486	15	0.7552	0.6329
	PA	13	0.9596	1	6	0.7008	0.5957	9	0.0025*	0.0184*
	BisMePA	4	0.1589	1	1	**0.0041**	**0.0168**	6	0.2812	0.3647
	dMePE	9	0.195	1	2	0.2041	0.269	0	N/A	N/A
	PG	19	0.6255	1	4	0.4685	0.486	4	0.859	0.6765
	BisMePE	1	0.8072	1	0	N/A	N/A	0	N/A	N/A
	BisMePS	0	N/A	N/A	0	N/A	N/A	2	0.0001*	0.0022*
	CL	22	0.5812	1	0	N/A	N/A	0	N/A	N/A
	PEt	7	0.3261	1	2	0.9792	0.7283	0	N/A	N/A
	PMe	2	0.8695	1	0	N/A	N/A	0	N/A	N/A
	PIP2	2	0.1393	1	0	N/A	N/A	3	0.0161*	0.0394*
	PIP	1	0.7034	1	0	N/A	N/A	0	N/A	N/A
	LPC	30	0.7943	1	10	0.6835	0.5957	7	0.2805	0.3647
	LPE	23	0.9947	1	16	0.6396	0.5957	4	0.0127*	0.035*
	LPS	7	0.9061	1	5	0.211	0.269	2	0.0817	0.1287
	LPI	7	0.7746	1	1	0.1715	0.2551	0	N/A	N/A
	LPG	4	0.8888	1	0	N/A	N/A	0	N/A	N/A
	LdMePE	1	0.4552	1	0	N/A	N/A	0	N/A	N/A
	BiotinylPE	0	N/A	N/A	1	0.8078	0.6554	1	0.0225*	0.0451*
Glycerolipids	TG	107	0.5998	1	44	0.0057*	0.0168*	72	0.0002*	0.0022*
	MGDG	3	0.8693	1	2	**0.0005**	**0.0089**	5	0.0214*	0.0451*
	MGMG	6	0.7537	1	0	N/A	N/A	6	0.0497*	0.0887
	DG	13	0.1381	1	70	0.1174	0.1905	59	0.6614	0.5834
	SQMG	2	0.5986	1	0	N/A	N/A	0	N/A	N/A
	SQDG	1	0.9316	1	0	N/A	N/A	0	N/A	N/A
Sphingolipids	Hex1Cer	0	N/A	N/A	85	0.0243*	0.0542	104	0.4617	0.4627
	CerG1	50	0.5466	1	0	N/A	N/A	0	N/A	N/A
	SM	47	0.6398	1	23	**0.0066**	**0.0168**	36	0.3243	0.3973
	Cer	14	0.9804	1	6	**0.0048**	**0.0168**	21	0.4374	0.4627
	CerP	0	N/A	N/A	0	N/A	N/A	17	0.0035*	0.0193*
	ST	10	0.3977	1	9	0.2283	0.2717	14	0.2176	0.3199
	So	3	0.4465	1	0	N/A	N/A	0	N/A	N/A
	CerPE	0	N/A	N/A	1	0.0766	0.1367	0	N/A	N/A
	phSM	4	0.3619	1	0	N/A	N/A	0	N/A	N/A
	CerG2GNAc1	1	0.5784	1	0	N/A	N/A	0	N/A	N/A
	SPH	0	N/A	N/A	0	N/A	N/A	1	0.775	0.6329
	Hex2Cer	0	N/A	N/A	0	N/A	N/A	1	0.0112	0.035
Sterol Lipids	ChE	1	0.5341	1	1	0.918	0.7124	2	0.9151	0.6958
	ZyE	0	N/A	N/A	0	N/A	N/A	3	0.0092*	0.0338*
Fatty Acyls	FA	2	0.5893	1	0	N/A	N/A	0	N/A	N/A
	AcCa	0	N/A	N/A	0	N/A	N/A	2	0.5847	0.5372
Prenol Lipids	Co	0	N/A	N/A	0	N/A	N/A	1	0.0523	0.0887
	Total	800			632			735		

Table 1. Overview of lipid subclass changes at 6, 9, and 12 months.

Bold text indicates lipid subclasses significantly different between WT and LacQ140 mice ($p<0.05$ or $q<0.05$).
Asterisk (*) indicates lipid subclasses significantly different among other groups ($p<0.05$ or $q<0.05$).
One way ANOVA was conducted followed by Tukey's multiple comparisons test, two-stage linear step-up procedure of Benjamini, Krieger, and Yekutieli, $q<0.05$.

Table 2. Overall comparison of lipidomic results across ages.

Age	# Species detected	# Species different at p<0.05*	# Species different for WT/LacQ140 at p<0.05	# Species different at q<0.05**	# Species different for WT/LacQ140 at q<0.05	# Species recovered with lowering (q<0.05)
6 months	800	9	4	0	0	0
9 months	632	192	72	17	14	14
12 months	735	162	36	72	26	1

***p value for ANOVA; **Adjusted p value determined using Benjamini, Krieger, and Yekutieli procedure**

MAIN FIGURE LEGENDS

Figure 1. Generation of LacQ140 mice and treatment paradigm

(a) The *LacO*/*LacIR*-regulatable HD mouse model (LacQ140) was generated by crossing the *Htt*$^{LacQ140/+}$ mouse to the *Tg*$^{ACTB\text{-}lacI*Scrb}$ mouse [58] as previously described [59]. The default state of the LacQ140 mouse is global repression of m*Htt* due to *Lac* Repressor binding to the *Lac* operators. Administration of IPTG starting from embryonic day 5 (E5) interrupts the binding between the *Lac* repressor and operators, resulting in a de-repressed state, and maximal expression of m*Htt* in LacQ140. All WT mice were Htt$^{LacO+/+}$; b-actin-LacI^{R} tg. **(b)** Mice were fed *ad libitum*; the lactose analog IPTG was provided in drinking water (at 10mM) which de-represses the *LacQ140* allele and keeps normal m*Htt* expression. During embryonic development, m*Htt* expression levels were maintained at normal levels by administering IPTG to pregnant dams starting at embryonic day 5 (E5). IPTG was continuously administered to WT mice. IPTG was administered always (m*Htt* always expressed, LacQ140), withdrawn at 8 months (m*Htt* repressed beginning at 8 months, LacQ140_8M), withdrawn 2 at months (m*Htt* repressed beginning at 2 months, LacQ140_2M), or never administered (m*Htt* always repressed, LacQ140_A). Tissue for each group (except LacQ140_8M) was collected at 6, 9, and 12 months of age.

Figure 2. Analysis of mHTT protein levels in crude homogenates of 6-, 9- and 12-months old mice.

HTT levels were analyzed by capillary immunoassay on equal amounts of protein (0.6 µg) using anti-HTT antibody Ab1 and anti-polyQ antibody MW1 (**a**). Peak area analysis performed using Compass software in 6-month-old mice shows a significant decrease in WT HTT as detected with Ab1 in all LacQ140 mice compared to WT mice ($F(3, 20) = 5.674$, **P=0.0056, One-way ANOVA with Tukey's multiple comparison test, n=6). mHTT levels are significantly lower in LacQ140_2M and LacQ140_A as detected with both Ab1 and MW1 compared to LacQ140 (**a**, Ab1: $F(2, 15) = 11.25$, **P=0.0010, -38% and -43% respectively; MW1: $F(2, 14) = 9.879$, **P=0.0021, -40% and -47% respectively). Peak area analysis in 9-month-old mice shows a significant decrease in WT HTT as detected with Ab1 in all LacQ140 mice compared to WT mice ($F(3, 20) = 34.67$, ****P<0.0001, One-way ANOVA with Tukey's multiple comparison test, n=6). mHTT levels are significantly lower in LacQ140_2M and LacQ140_A, as detected with both Ab1 and MW1, compared to LacQ140 (**b**, Ab1: $F(2, 15) = 10.82$, **P=0.0012, -42% and -52% respectively; MW1: $F(2, 15) = 20.82$, ****P<0.0001, -44% and -43% respectively). Peak area analysis in 12-month-old mice shows a significant decrease in WT HTT as detected with Ab1 in all LacQ140 mice compared to WT mice ($F(4, 25) = 15.81$, ****P<0.0001, One-way ANOVA with Tukey's multiple comparison test, n=6). WT HTT was significantly lower in LacQ140_A compared to LacQ140_8M and LacQ140_2M mice. mHTT levels are significantly lower in LacQ140_A mice, as detected with Ab1, compared to LacQ140 (**c**, Ab1: $F(3, 20) = 5.017$, **P=0.0094, -51%, One-way ANOVA with Tukey's multiple comparison test, n=6). Asterisks on graphs represent Tukey's multiple comparison test, n=6 mice per group (*p<0.05, **p<0.01, ***p<0.001, ****p<0.0001).

Figure 3. HTT protein levels in P1 fractions.

Equal protein (10 µg) from P1 fractions from 6-month-old (**a**) and 12-month-old (**b**) LacQ140 and WT mice were analyzed by western blot for HTT levels with anti-HTT Ab1. No aggregated protein was observed at the top of the gel (arrowhead). Total pixel intensity quantification for each band was measured using ImageJ software and normalized to HDAC1 signal. There was a significant decrease in WT HTT signal in all the treatment conditions for LacQ140 mice compared to WT mice in both **(a)** 6-month-old mice ($F(3, 20) = 40.34$, ****P<0.0001, One-way ANOVA with Tukey's multiple comparison test, n=6) and **(b)** 12-month-old mice ($F(4, 25) = 11.01$, ****P<0.0001 ,One-way ANOVA with Tukey's multiple comparison test, n=6). There were significantly lower levels of mHTT in the 6-month-old LacQ140_A mice compared to LacQ140 (**a,** $F(2, 15) = 8.233$, **P=0.0039, One-way ANOVA with Tukey's multiple comparison test, n=6) but no changes in mHTT levels were detected in the **(b)** 12-month-old LacQ140 mice ($F(3, 20) = 1.137$, P=0.3583, n.s., One-way ANOVA). Equal protein (10 µg) from P1 fractions from 12-month-old LacQ140 and WT mice were analyzed by western blot for HTT levels with anti-HTT S830 (**c**). The S830 antibody detected a smear of HTT signal (bracket) as well as full-length mHTT (arrow). There were significantly lower levels of full length mHTT in the 12-month-old LacQ140_A mice compared to LacQ140 ($F(3, 20) = 3.548$, *P=0.0330, One-way ANOVA with Tukey's multiple comparison test, n=6) and no changes detected in the HTT smear in all LacQ140 mice ($F(3, 20) = 0.9281$,

P=0.4453, n.s., One-way ANOVA). Asterisks on graphs represent Tukey's multiple comparison test, n=6 mice per group (*p<0.05, **p<0.01, ***p<0.001, ****p<0.0001).

Figure 4. Analyses of lipids in crude homogenates LacQ140 caudate putamen by mass spectrometry.
(a) Total lipid intensity detected at 6 months normalized to WT; no significant difference between groups (one-way ANOVA: F(3, 20) = 0.4604, P=0.7130, n.s., n=6). **(b)** Total lipid intensity detected at 9 months normalized to WT; LacQ140 mice have decreased total lipid intensity which is reversed in LacQ140_A mice (one-way ANOVA & Tukey's multiple comparison test: F(3, 20) = 5.474, **P=0.0065, n=6). **(c)** Total lipid intensity detected at 12 months normalized to WT; no significant difference between groups (one-way ANOVA: F (4, 25) = 0.7504, P=0.5671, n.s., n=6). **(d)** Heatmap depicts the lipid subclass composition for WT, LacQ140, and treatment groups at 9 months. Hierarchical clustering was performed across lipid subclasses (rows) and columns (animals) using the one minus Pearson correlation distance metric. ANOVA p-value column indicates lipid subclasses significantly changed between LacQ140 and WT mice in green (p<0.05, One-way ANOVA with Tukey's multiple comparison test, n=6). Lipid subclasses with adjusted p-values (q) < 0.05 LacQ140 vs WT are indicated in purple (q<0.05, two-stage linear step-up procedure of Benjamini, Krieger, and Yekutieli, N=24 lipid subclasses, n=6 mice). Source data and full statistical details can be found in **Additional Files 1, 4, & 5**.

Figure 5. Restoration of dysregulated lipid subclasses with lowering of m*Htt.*
Graphs show relative intensities for lipid subclasses expressed as a percent of total lipid intensity detected (bars = mean, error bars = ± SD). **(a)** PS increased in LacQ140 mice and is reversed in LacQ140_A mice; F(3, 20) = 7.601, **P=0.0014, q=0.0125, **(b)** PI increased in LacQ140 mice and reversed in LacQ140_A mice; F(3, 20) = 5.707, **P=0.0054, q=0.0168, **(c)** BisMePA decreased in LacQ140 mice and is reversed in LacQ140 mice; F(3, 20) = 6.086, **P=0.0041, q=0.0168, **(d)** SM decreased in LacQ140 mice and is reversed in LacQ140_2M and LacQ140_A mice; F(3, 20) = 5.465, **P=0.0066, q=0.0168, **(e)** Cer decreased in LacQ140 mice; F(3, 20) = 5.883, **P=0.0048, q=0.0168, **(f)** MGDG decreased in LacQ140 mice and is reversed in LacQ140_2M and LacQ140_A mice; F(3, 20) = 9.350, ***P=0.0005, q=0.0089. Statistics are one-way ANOVA and asterisks on graphs represent Tukey's multiple comparison test, n=6 mice per group. **(g)** Heatmap shows individual lipid species that comprise each subclass. Hierarchical clustering was performed across individual lipid species (rows) and animals (columns) using the one minus Pearson correlation distance metric. Individual lipid species significantly changed between any group are indicated in green (p<0.05, one-way ANOVA), lipid species significantly changed between LacQ140 and WT are indicated in purple (p<0.05, one-way ANOVA, n=6) and red (q<0.05, one-way ANOVA & two-stage linear step-up procedure of Benjamini, Krieger, and Yekutieli, N=632 lipid species, n=6 mice). Source data and full statistical details can be found in **Additional Files 1, 4, & 5**.

Figure 6. Lipid metabolism and myelin associated transcriptional changes and reversal with m*Htt* lowering.
(a) Dotplot (clusterProfiler) of lipid or myelin related GO BP terms overrepresented (one sided hypergeometric test, padj<0.05) in 6-month LacQ140 downregulated genes (padj<0.05, FC>20%). GeneRatio represents the number of genes associated with each GO term/number of downregulated genes. Dots are sized by count of genes associated with respective terms. **(b)** Gene set enrichment analysis (clusterProfiler) of 6-month LacQ140, LacQ140_2M and LacQ140_A groups compared to WT. All lipid and myelin associated GO BP terms significantly enriched in LacQ140 compared to WT (padj<0.05) are displayed. X axis for each respective group represents the normalized enrichment score (NES) and bars are colored by significance (padj<0.05 = blue, padj>0.05 = tan). Adjusted p-values are displayed adjacent to bars. **(c)** Heatmap shows differentially expressed genes in 6-month-old LacQ140 mice compared to WT (padj<0.05, FC > ±20%). Gene expression is shown as median ratio normalized counts (DESeq2), scaled by respective gene (columns). Bars above the heatmap indicate DEGs reversed with m*Htt* lowering. LacQ140_2M = green, LacQ140_A = purple; padj<0.05, FC > 20% opposite of LacQ140**. (d)** Dotplot of lipid or myelin related GO BP terms overrepresented in 12-month downregulated genes. GO BP terms significantly overrepresented at 6-months (a) are displayed for comparison. 4/9 terms (ensheathment of neurons, axon ensheathment, myelination, and phospholipase C activating G-protein coupled receptor signaling pathway) are significantly overrepresented in 12-month LacQ140 downregulated genes (one sided hypergeometric test, padj < 0.05). **(e)** Gene set enrichment analysis

of LacQ140, LacQ140_8M, LacQ140_2M and LacQ140_A groups compared to WT. GO BP terms enriched at 6-months (b) are displayed for comparison. 8/22 GO BP terms are significantly negatively enriched (padj < 0.05) at 12-months, shown in blue. **(f)** Heatmap shows differentially expressed genes in 12-month-old LacQ140 mice compared to WT (padj<0.05, FC > ±20%). Gene expression is shown as median ratio normalized counts (DESeq2), scaled by respective gene (columns). Bars above the heatmap DEGs reversed with m*Htt* lowering (LacQ140_8M = bottom bar, no reversal, LacQ140_2M = green, LacQ140_A = purple; padj<0.05, FC >20% opposite of LacQ140). GO BP terms associated with genes, fold changes, and exact FDR values can be found in **Additional Files 2 & 3.**

Figure 7. Simplified de novo sphingolipid biosynthesis pathway.
(a) Serine and palmitoyl CoA are condensed by serine palmitoyltransferase (SPT) to generate 3-ketosphinganine. 3-ketophinganine is reduced to dihydrosphingosine by 3-ketodihydrosphingosine reductase (KDSR). Dihydrosphingosine is acetylated by ceramide synthases (CERS) and further desaturated by ceramide desaturase (DEGS) to generate ceramide. Ceramide is the substrate for generation of other sphingolipids (sphingomyelin, galactosylceramide, glucosylceramide, sulfatide, and lactosylceramide). Abbreviations: SGMS = sphingomyelin synthase, SMase = sphingomyelinase, UGT8A = UDP galactosyltransferase 8A, GALC = galactosylceramidase. CST = galactosylceramide sulfotransferase, ARSA = arylsulfatase, GBA = glucosylceramidase, UGCG = UDP-glucose ceramide glucosyltransferase, LacCer synthase = lactosylceramide synthase. **(b)** Biosynthesis of non-hydroxylated sphingolipids. **(c)** Biosynthesis of 2-hydroxy sphingolipids. Fatty acid 2-hydroxylase (FA2H) catalyzes hydroxylation of fatty acids in the C2 position, which can be incorporated into sphingolipid precursors (i.e., dihydroceramide) in the acylation step of de novo synthesis.

Figure 1

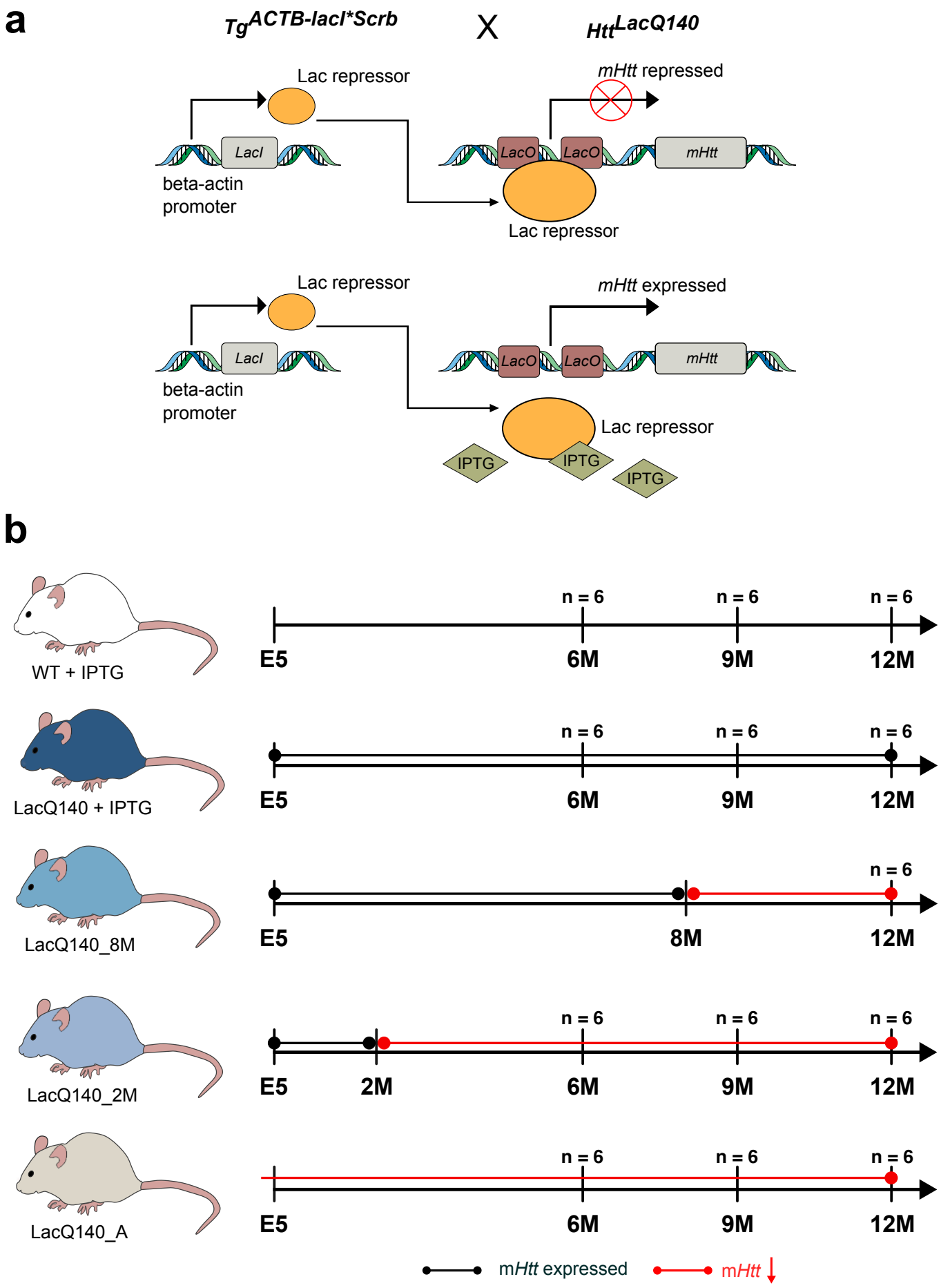
a
Tg ACTB-lacI*Scrb
X
Htt LacQ140
Lac repressor
mHtt repressed
LacI
LacO
LacO
mHtt
beta-actin
promoter
Lac repressor
Lac repressor
mHtt expressed
LacI
LacO
LacO
mHtt
beta-actin
promoter
Lac repressor
IPTG
IPTG
IPTG
b
WT + IPTG
n = 6
n = 6
n = 6
E5
6M
9M
12M
LacQ140 + IPTG
n = 6
n = 6
n = 6
E5
6M
9M
12M
LacQ140_8M
n = 6
E5
8M
12M
LacQ140_2M
n = 6
n = 6
n = 6
E5
2M
6M
9M
12M
LacQ140_A
n = 6
n = 6
n = 6
E5
6M
9M
12M
mHtt expressed
mHtt

Figure 2

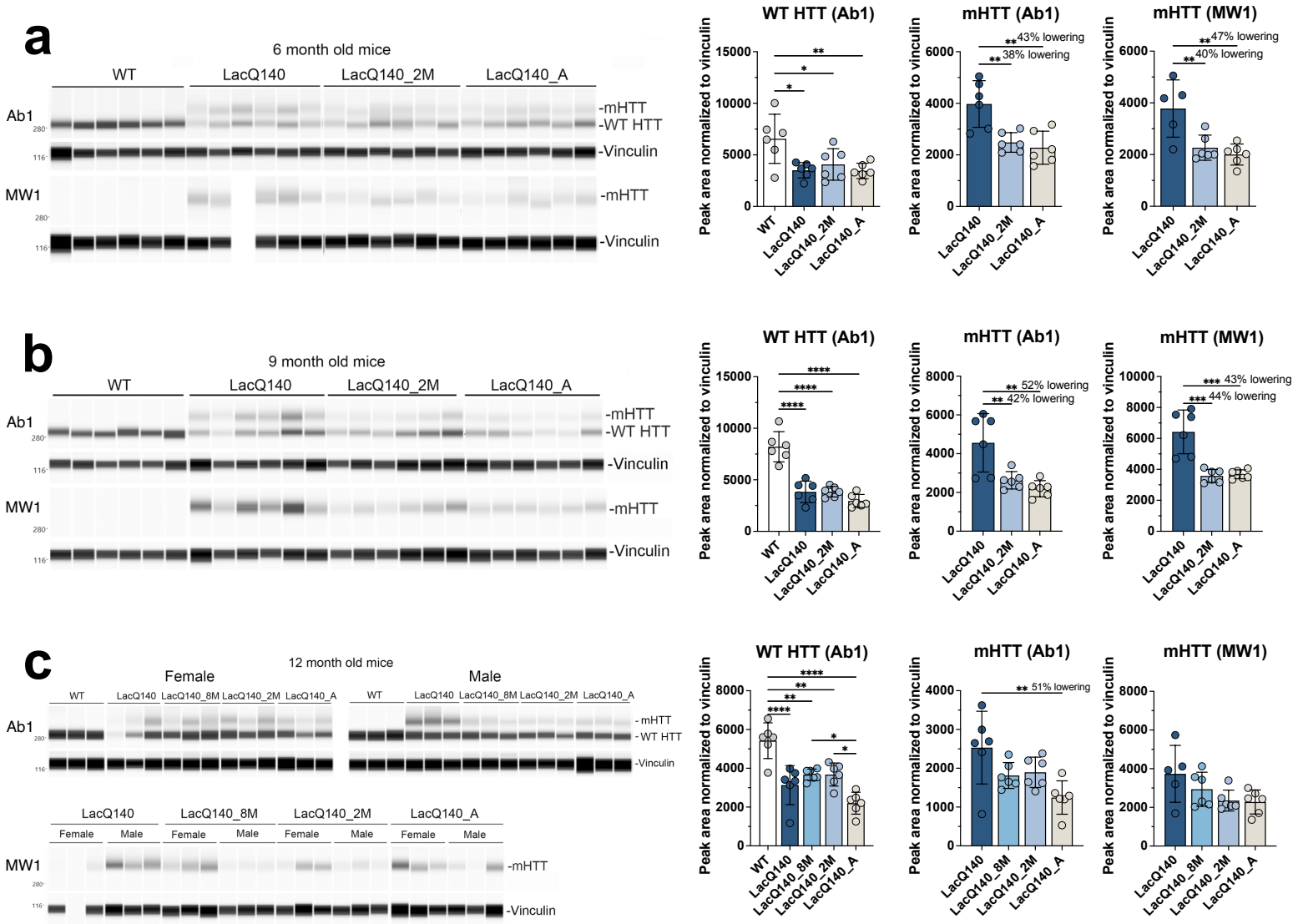
a
6 month old mice
WT
LacQ140
LacQ140_2M
LacQ140_A
Ab1
-mHTT
-WT HTT
-Vinculin
MW1
-mHTT
-Vinculin
WT HTT (Ab1)
mHTT (Ab1)
mHTT (MW1)
Peak area normalized to vinculin
43% lowering
38% lowering
47% lowering
40% lowering
b
9 month old mice
52% lowering
42% lowering
43% lowering
44% lowering
c
12 month old mice
Female
Male
LacQ140_8M
Female
Male
51% lowering

Figure 3

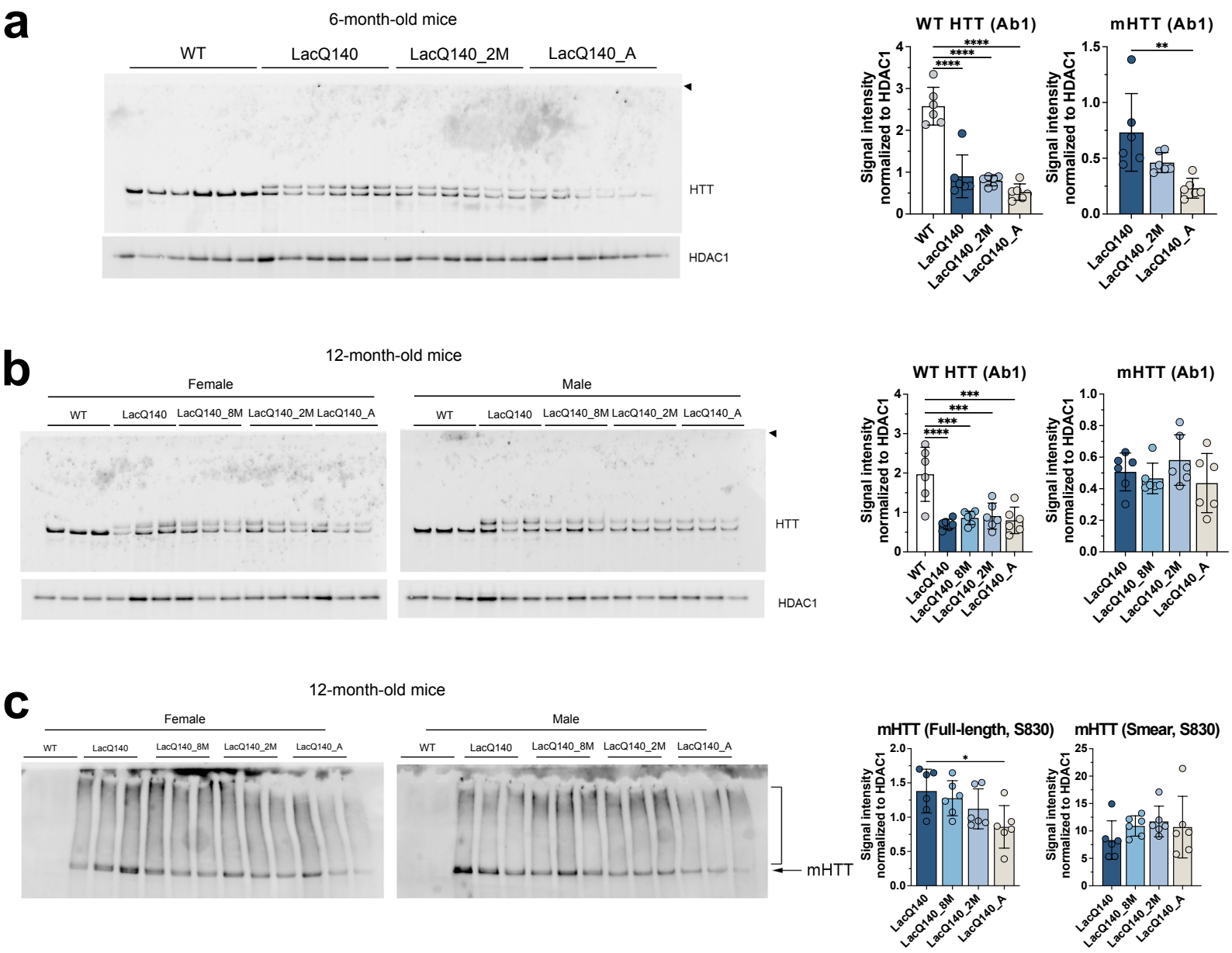
a
6-month-old mice
WT
LacQ140
LacQ140_2M
LacQ140_A
HTT
HDAC1
WT HTT (Ab1)
mHTT (Ab1)
Signal intensity normalized to HDAC1
****
**
b
12-month-old mice
Female
Male
WT
LacQ140
LacQ140_8M
LacQ140_2M
LacQ140_A
HTT
HDAC1
***
c
mHTT
mHTT (Full-length, S830)
mHTT (Smear, S830)
*

Figure 4

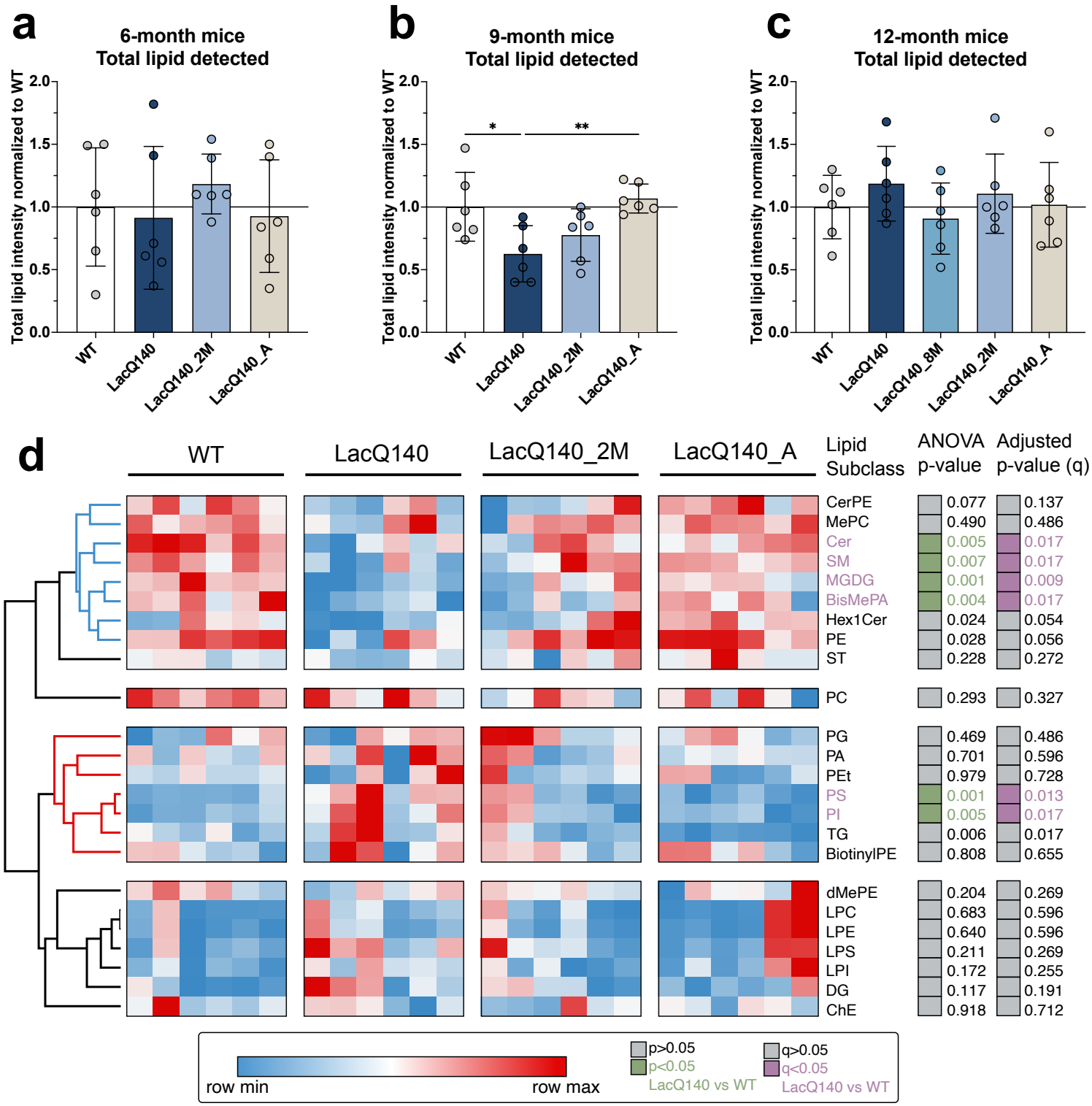
a
6-month mice
Total lipid detected
Total lipid intensity normalized to WT
2.0
1.5
1.0
0.5
0.0
WT
LacQ140
LacQ140_2M
LacQ140_A
b
9-month mice
Total lipid detected
Total lipid intensity normalized to WT
*
**
WT
LacQ140
LacQ140_2M
LacQ140_A
c
12-month mice
Total lipid detected
Total lipid intensity normalized to WT
WT
LacQ140
LacQ140_8M
LacQ140_2M
LacQ140_A
d
WT
LacQ140
LacQ140_2M
LacQ140_A
Lipid Subclass
ANOVA p-value
Adjusted p-value (q)
CerPE 0.077 0.137
MePC 0.490 0.486
Cer 0.005 0.017
SM 0.007 0.017
MGDG 0.001 0.009
BisMePA 0.004 0.017
Hex1Cer 0.024 0.054
PE 0.028 0.056
ST 0.228 0.272
PC 0.293 0.327
PG 0.469 0.486
PA 0.701 0.596
PEt 0.979 0.728
PS 0.001 0.013
PI 0.005 0.017
TG 0.006 0.017
BiotinylPE 0.808 0.655
dMePE 0.204 0.269
LPC 0.683 0.596
LPE 0.640 0.596
LPS 0.211 0.269
LPI 0.172 0.255
DG 0.117 0.191
ChE 0.918 0.712
row min
row max
p>0.05
p<0.05
LacQ140 vs WT
q>0.05
q<0.05
LacQ140 vs WT

Figure 5

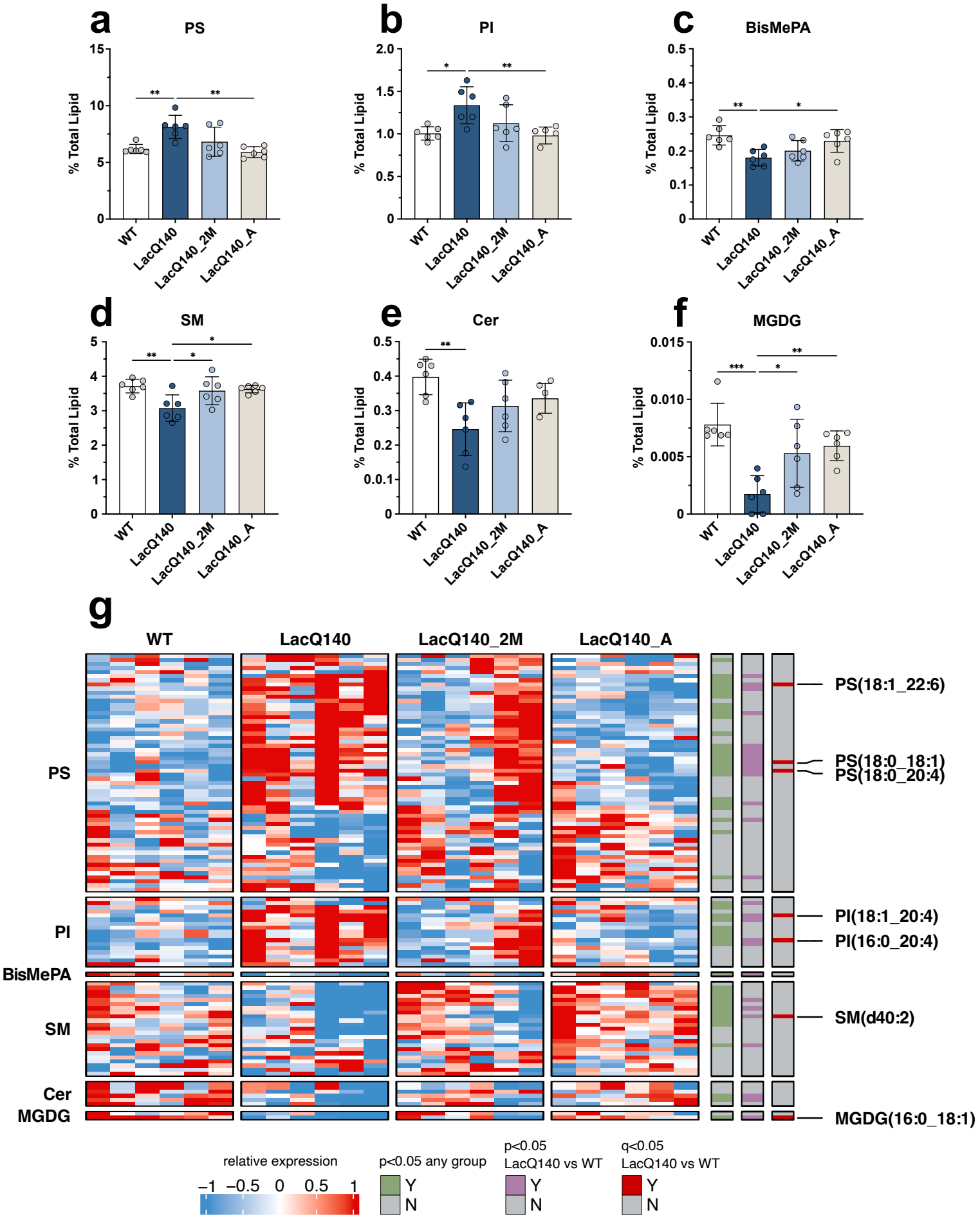
a
PS
b
PI
c
BisMePA
d
SM
e
Cer
f
MGDG
% Total Lipid
WT
LacQ140
LacQ140_2M
LacQ140_A
g
PS
PI
BisMePA
SM
Cer
MGDG
PS(18:1_22:6)
PS(18:0_18:1)
PS(18:0_20:4)
PI(18:1_20:4)
PI(16:0_20:4)
SM(d40:2)
MGDG(16:0_18:1)
relative expression
−1 −0.5 0 0.5 1
p<0.05 any group
Y
N
p<0.05
LacQ140 vs WT
q<0.05
LacQ140 vs WT

Figure 6

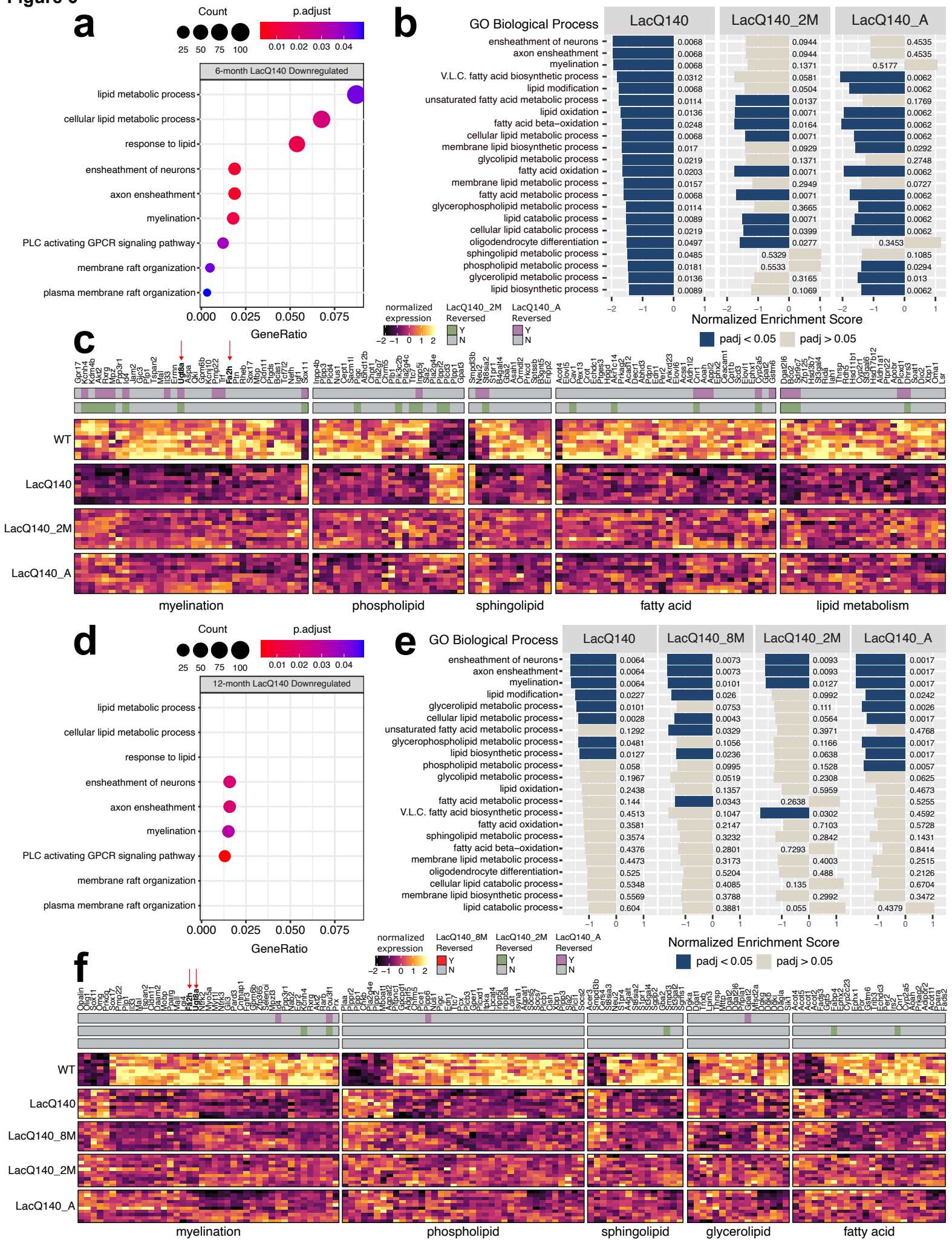
a
Count
p.adjust
25 50 75 100
0.01 0.02 0.03 0.04
6-month LacQ140 Downregulated
lipid metabolic process
cellular lipid metabolic process
response to lipid
ensheathment of neurons
axon ensheathment
myelination
PLC activating GPCR signaling pathway
membrane raft organization
plasma membrane raft organization
0.000 0.025 0.050 0.075
GeneRatio
b
GO Biological Process
LacQ140
LacQ140_2M
LacQ140_A
Normalized Enrichment Score
padj < 0.05
padj > 0.05
c
normalized expression
LacQ140_2M Reversed
LacQ140_A Reversed
WT
LacQ140
LacQ140_2M
LacQ140_A
myelination
phospholipid
sphingolipid
fatty acid
lipid metabolism
d
12-month LacQ140 Downregulated
e
LacQ140_8M
f
glycerolipid

Figure 7

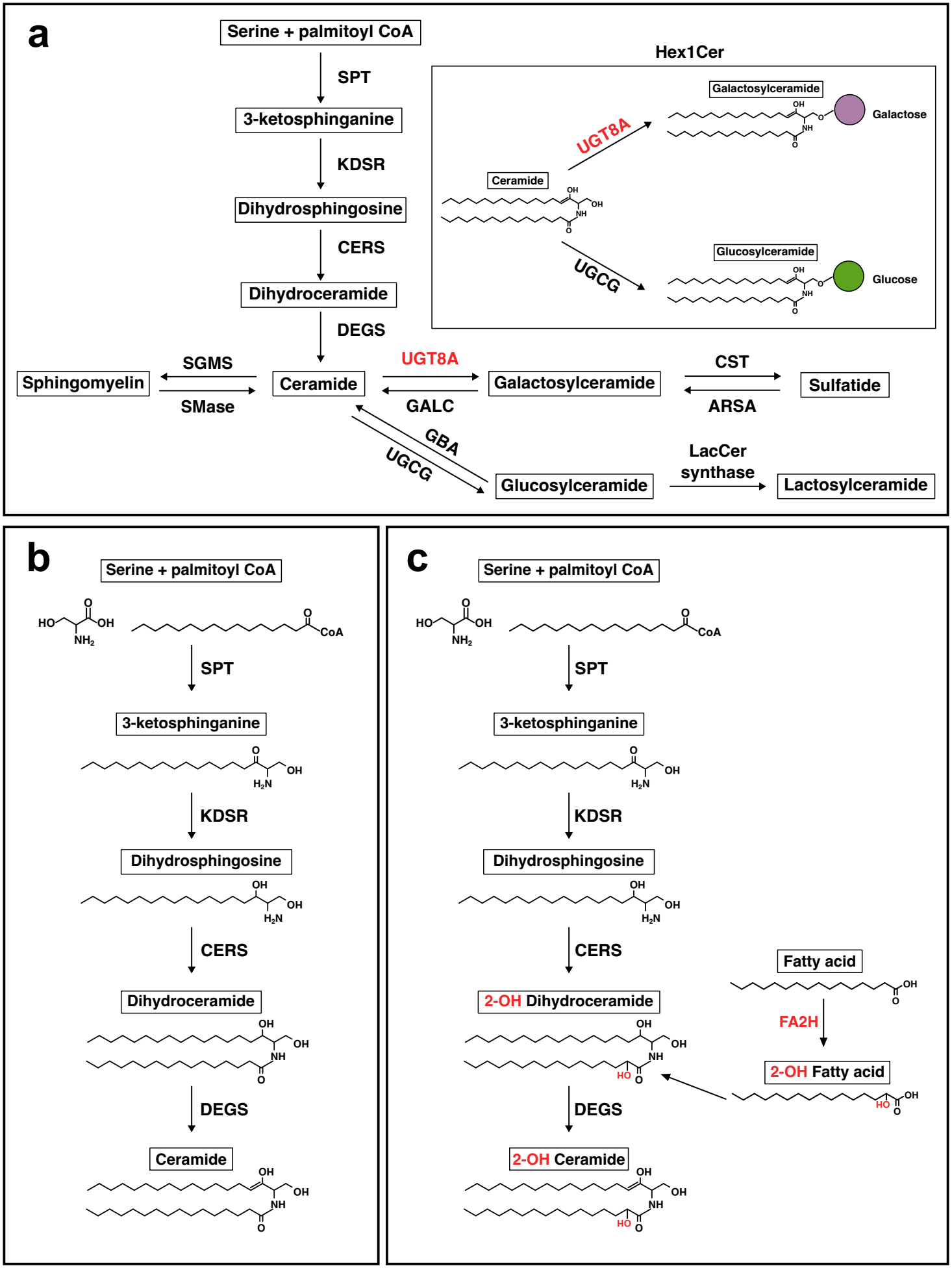
a
Serine + palmitoyl CoA
SPT
3-ketosphinganine
KDSR
Dihydrosphingosine
CERS
Dihydroceramide
DEGS
Hex1Cer
Galactosylceramide
Galactose
UGT8A
Ceramide
UGCG
Glucosylceramide
Glucose
Sphingomyelin
SGMS
SMase
Ceramide
UGT8A
GALC
Galactosylceramide
CST
ARSA
Sulfatide
GBA
UGCG
Glucosylceramide
LacCer synthase
Lactosylceramide
b
Serine + palmitoyl CoA
SPT
3-ketosphinganine
KDSR
Dihydrosphingosine
CERS
Dihydroceramide
DEGS
Ceramide
c
Serine + palmitoyl CoA
SPT
3-ketosphinganine
KDSR
Dihydrosphingosine
CERS
2-OH Dihydroceramide
Fatty acid
FA2H
2-OH Fatty acid
DEGS
2-OH Ceramide

Supplementary Figure 1

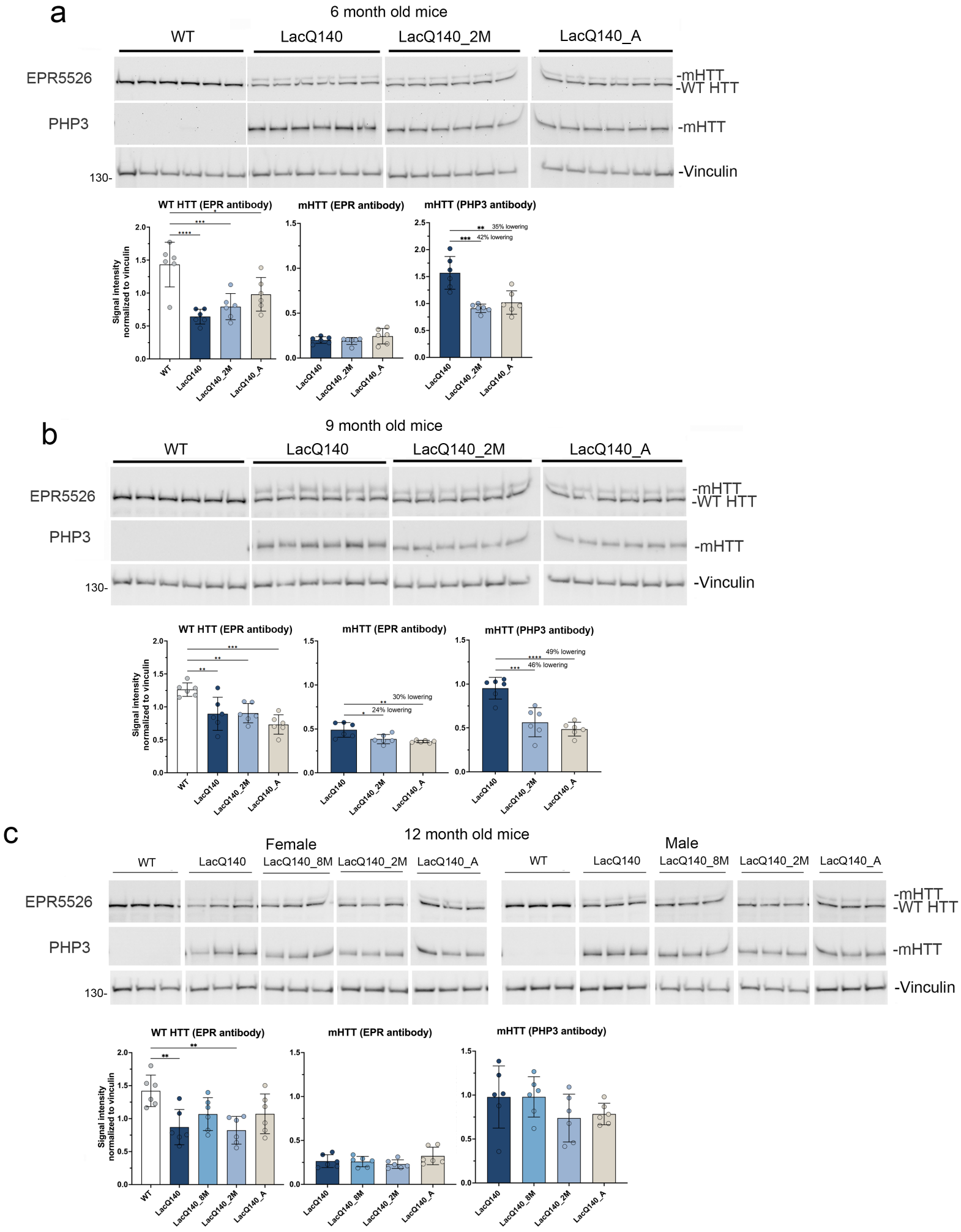

Supplementary Figure 1. Analysis of mHTT protein levels with EPR5526 and PHP3 in crude homogenates of 6-, 9- and 12-months old mice.

HTT levels were analyzed by western blot on equal amounts of protein (10 µg) using anti-HTT antibody EPR5526 and anti-polyQ antibody PHP3. Total pixel intensity quantification for each band measured using ImageJ software in 6-month-old mice shows a significant decrease in WT HTT as detected with EPR5526 in all LacQ140 mice compared to WT mice but no change in mHTT levels (**a**). mHTT levels are significantly lower in LacQ140_2M and LacQ140_A mice as detected with PHP3 compared to LacQ140 (**a**, -42% and -35% respectively, **p<0.01, ***p<0.001, One-way ANOVA with Tukey's multiple comparison test, n=6). Total pixel intensity quantification in 9-month-old mice shows a significant decrease in WT HTT as detected with EPR5526 in all LacQ140 mice compared to WT mice. (**b**). mHTT levels are significantly lower in LacQ140_2M and LacQ140_A mice as detected with EPR5526 and PHP3 compared to LacQ140 (**b**, EPR5526: -24% and -30%, respectively; PHP3: -46% and -49% respectively, *p<0.05, **p<0.01, ***p<0.001, One-way ANOVA with Tukey's multiple comparison test, n=6).Total pixel intensity quantification in 12-month-old mice shows a significant decrease in WT HTT as detected with EPR5526 in LacQ140 and LacQ140_2M compared to WT mice. No changes in mHTT levels as detected with either EPR5526 or PHP3 were observed (**c**).

Supplementary Figure 2

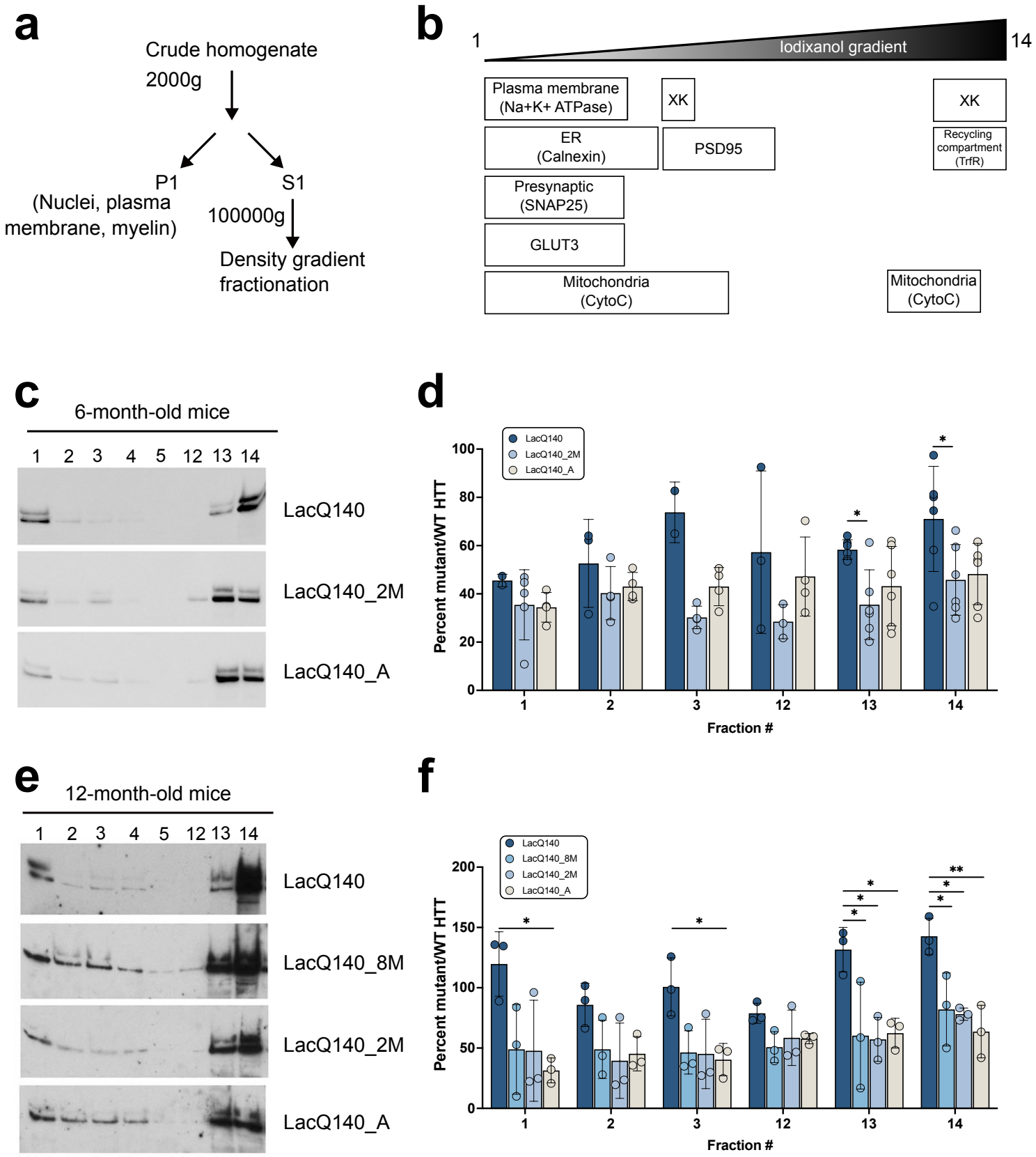

Supplementary Figure 2. Effects of m*Htt* lowering on the subcellular distribution of WT and mHTT protein by density gradient ultracentrifugation.

Diagram depicts the centrifugation strategy for protein samples **(a)**. Schematic shows the approximate location in the fractions of protein markers and the organelles found in these compartments **(b)**. Representative western blot images for equal volumes of fractions 1-5 and 12-14 from 6-month-old mice probed with anti-HTT antibody Ab1 are shown in **(c)**. The remaining images are shown in **Supplementary Figure 3a**. Total pixel intensity quantification for each band measured using ImageJ software is graphed as average percent mutant/WT HTT ± SD for each fraction **(d)**. Since each fraction contains different levels of proteins normally used to control for protein loading, levels of mHTT were normalized to levels of WT HTT which was not repressed/lowered. The ratio mutant/WT HTT is significantly higher in LacQ140 mice compared to LacQ140_2M in fractions 13 and 14 (*$p<0.05$, One-way ANOVA with Tukey's multiple comparison test for each fraction, n=6). Representative western blot images for equal volumes of fractions 1-4 and 11-14 from 12-month-old mice probed with anti-HTT antibody Ab1 are shown in **(e)**. The remaining images are shown in **Supplementary Figure 3c**. Total pixel intensity quantification for each band is graphed as average percent mutant/WT HTT ± SD for each fraction **(f)**. The ratio mutant/WT HTT is significantly higher in LacQ140 compared to LacQ140_8M, LacQ140_2M and/or LacQ140_A mice in fractions 1, 3, 13, and 14 (*$p<0.05$, **$p<0.01$, One-way ANOVA with Tukey's multiple comparison test for each fraction, n=3). Graphs indicate data in fractions where mHTT was detected in at least 3 mice except LacQ140_A fractions 1 and 3 where only 2 mice had detectible mHTT.

Supplementary Figure 3

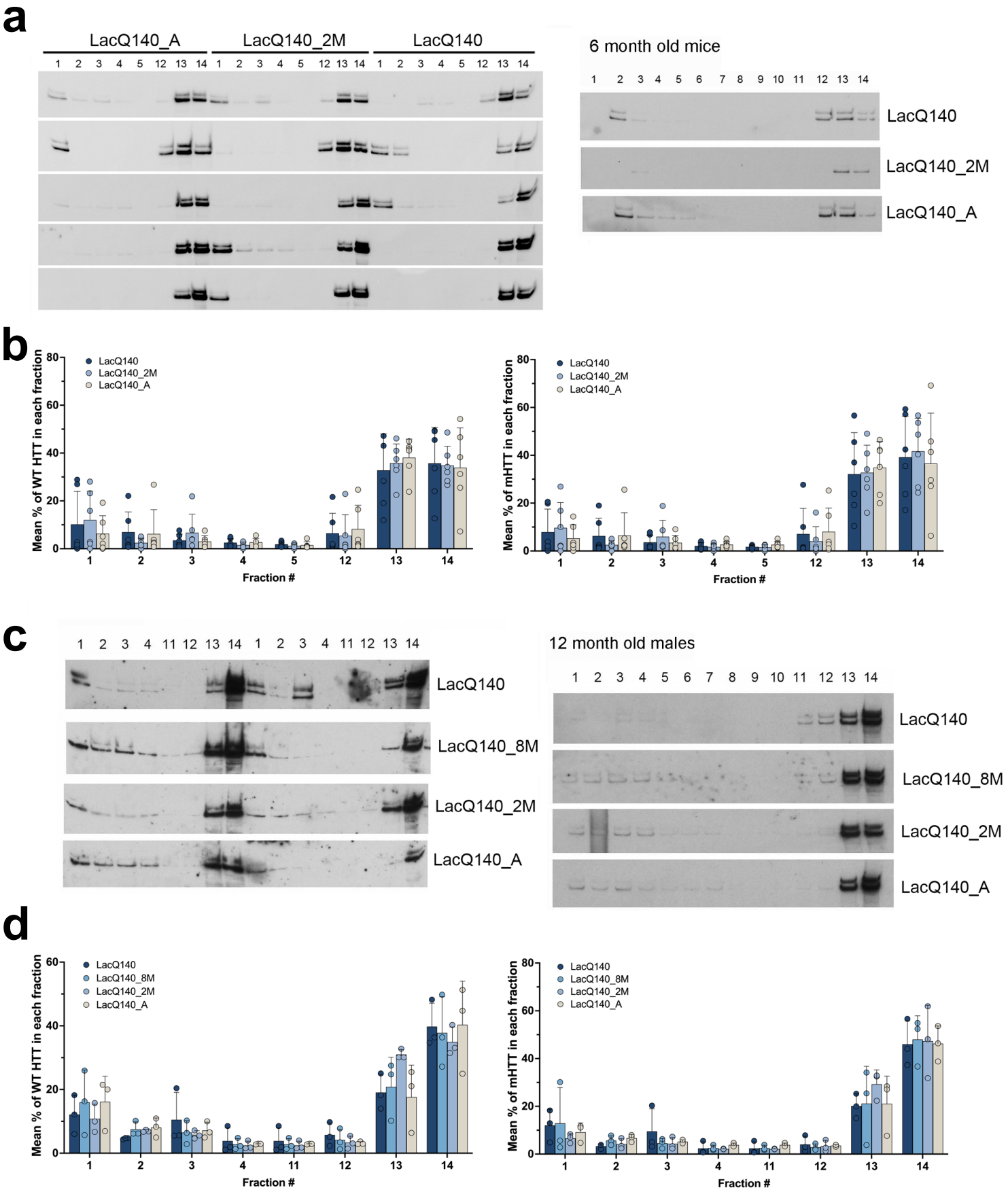

Supplementary Figure 3. Effects of m*Htt* lowering on the subcellular distribution of WT and mHTT.
Western blot images for equal volumes of fractions 1-14 (right blots, each strip is from one mouse) or fractions 1-5 and 12-14 (left blots) from 6-month-old mice probed with anti-HTT antibody Ab1 are shown in **(a)**. Each strip in left blots is a set of 1 mouse per treatment group with the groups labeled at the top of the blots. Total pixel intensity quantification for each band using ImageJ software is graphed as average percent of total HTT signal for each fraction ± SD **(b)**. Representative western blot images for equal volumes of fractions 1-14 (right blots, each strip is from one mouse) or 1-4 and 11-14 (left blots) from 12-month-old mice probed with anti-HTT antibody Ab1 are shown in **(c)**. Each strip in the left blots is from 2 mice per group with the groups labeled on the right. Total pixel intensity quantified for each band using ImageJ software are graphed as average percent of total HTT signal for each fraction ± SD **(d)**. There is no difference in WT or mHTT levels as a percent of total HTT in any fraction with any treatment of LacQ140 mice at 6 or 12 months (One-way ANOVA with Tukey's multiple comparison test for each fraction, n=6 for 6 months and n=3 for 12 months).

Supplementary Figure 4

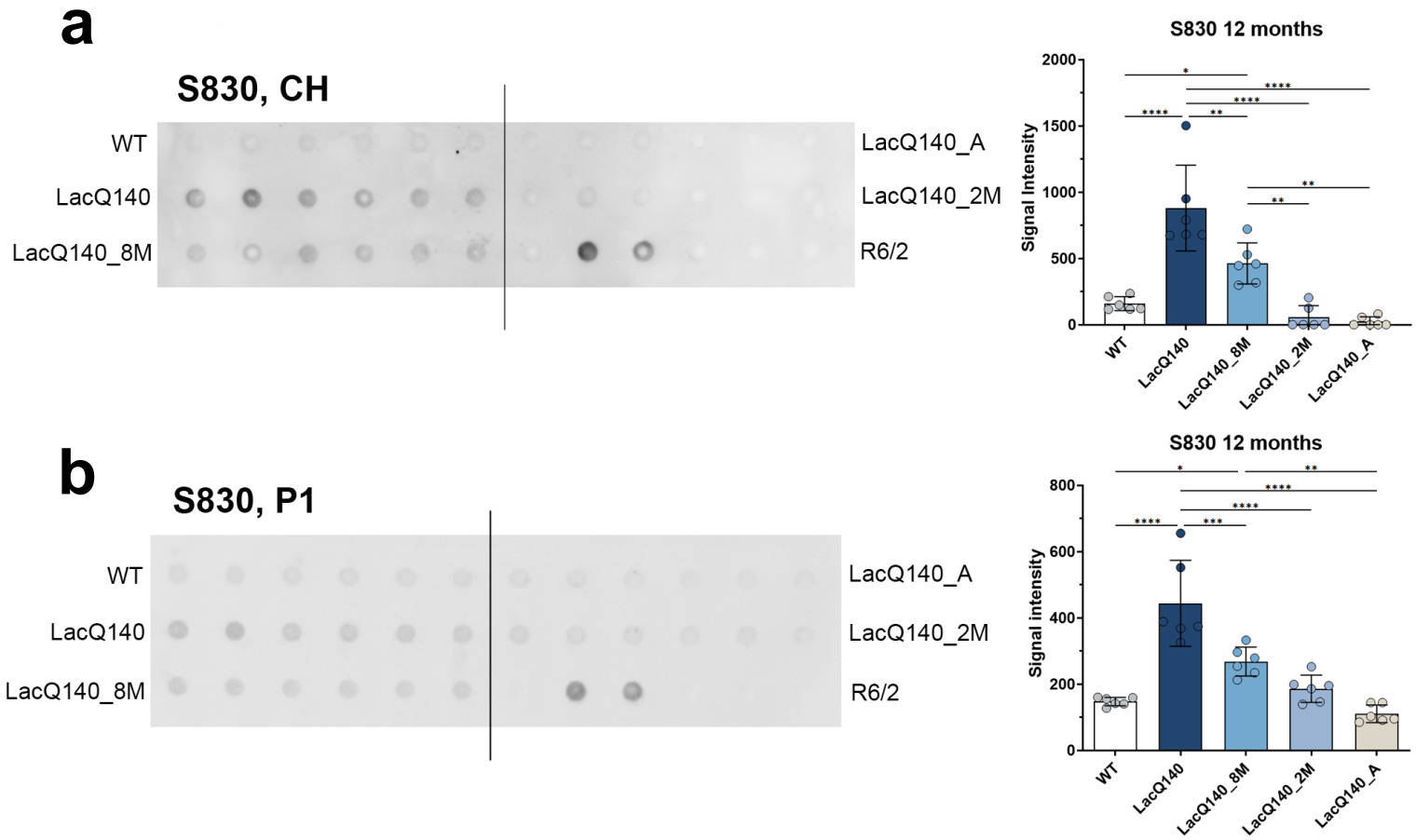

Supplementary Figure 4. HTT levels in crude homogenates and P1 fractions from WT and LacQ140 mice by filter trap assay.

Filter trap assays of 12-month-old crude homogenates **(a)** and P1 fractions **(b)** were probed with S830 antibody. Each dot represents one animal and each of the 6 dots across equals one group which is labeled on the left and right sides. There are 2 dots for the lysates from R6/2 HD mice which have a highly expressing transgene for a small fragment of HTT containing a large CAG repeat (180CAGs) and that accumulate numerous aggregates which have been shown to be retained in the assay and were used as a positive control. There was significantly more signal for aggregated mHTT in the 12-month-old LacQ140 mice compared to WT, LacQ140_8M, LacQ140_2M and LacQ140_A mice (**a**, *$p<0.05$, **$p<0.01$, ****$p<0.0001$, One-way ANOVA with Tukey's multiple comparison test, n=6). In the P1 fractions, there was significantly more signal for aggregated mHTT detected with S830 antibody in the 12-month LacQ140 mice compared to WT, LacQ140_8M, LacQ140_2M and LacQ140_A mice and in LacQ140_8M compared to WT and LacQ140_A mice (**b**, *$p<0.05$, **$p<0.01$, ***$p<0.001$, ****$p<0.0001$, One-way ANOVA with Tukey's multiple comparison test, n=6).

Supplementary Figure 5

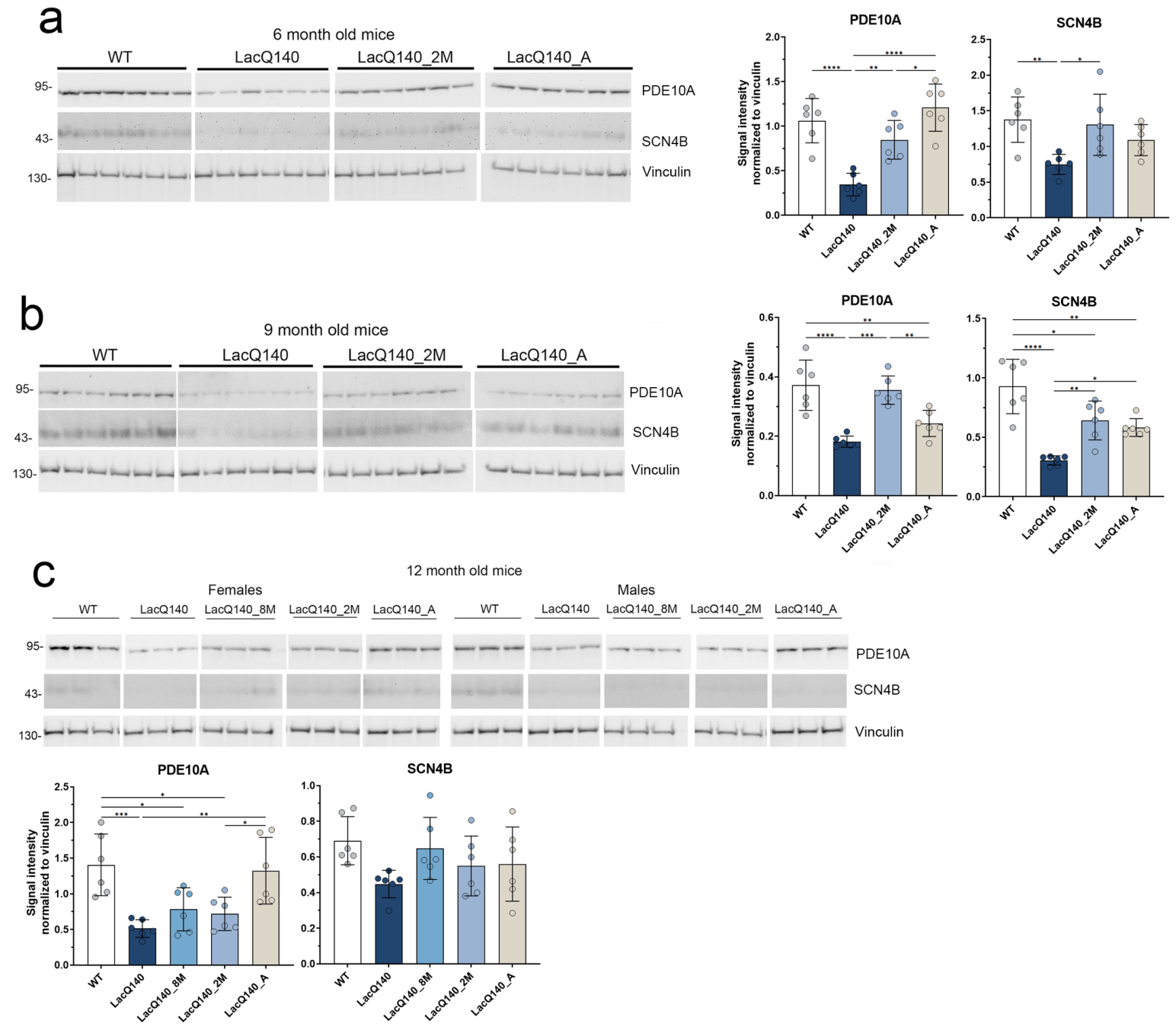

Supplementary Figure 5. Duration of m*Htt* lowering in 6, 9 and 12 months old LacQ140 mice affects levels of PDE10A and SCN4B.

PDE10A and SCN4B levels were analyzed by western blot on equal amounts of protein (10 µg). Total pixel intensity quantification for each band using ImageJ software in 6-month-old mice shows a significant decrease in PDE10A levels in LacQ140 compared to WT mice. There is an increase in PDE10A levels in LacQ140_2M and LacQ140_A mice compared to LacQ140 and no change from WT mice (**a,** *p<0.05, **p<0.01, ****p<0.0001, One-way ANOVA with Tukey's multiple comparison test, n=6). There is a significant decrease in SCN4B levels in LacQ140 compared to WT mice and a significant increase back to WT levels in LacQ140_2M mice. Total pixel intensity quantification in 9-month-old mice shows a significant decrease in PDE10A levels in LacQ140 compared to WT mice. There is an increase in PDE10A levels in LacQ140_2M compared to LacQ140 and no change from WT mice (**b,** **p<0.01, ***p<0.001, One-way ANOVA with Tukey's multiple comparison test, n=6). There is a significant decrease in SCN4B levels in LacQ140 compared to WT mice. There is a significant increase in SCN4B levels in LacQ140_2M and LacQ140_A mice compared to LacQ140 but significantly lower than in the WT mice (**b,** *p<0.05, **p<0.01, ***p<0.001, ****p<0.0001, One-way ANOVA with Tukey's multiple comparison test, n=6). Total pixel intensity quantification in 12-month-old mice shows a significant decrease in PDE10A levels in LacQ140, LacQ140_8M and LacQ140_2M compared to WT mice. There is an increase in PDE10A levels in LacQ140_A mice compared to LacQ140 and LacQ140_2M and no change from WT mice (**c,** *p<0.05, **p<0.01, ***p<0.001, One-way ANOVA with Tukey's multiple comparison test, n=6). There are no changes in SCN4B levels in any of the LacQ140 or WT mice.

Supplementary Figure 6

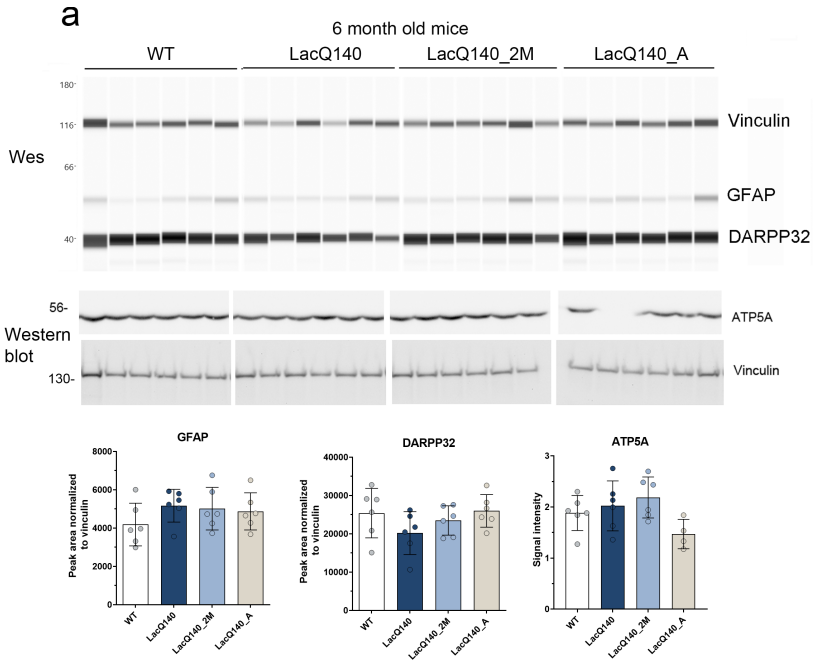

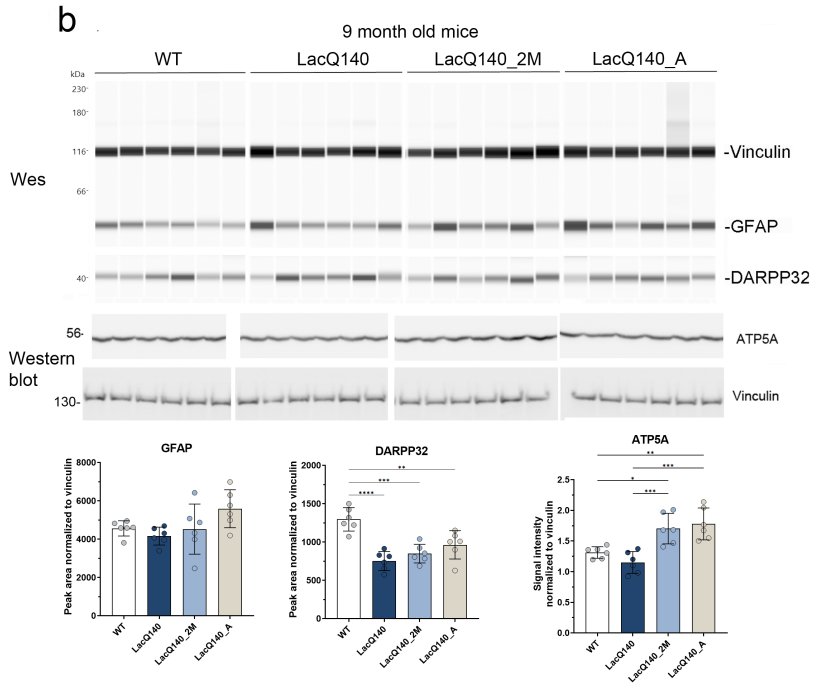

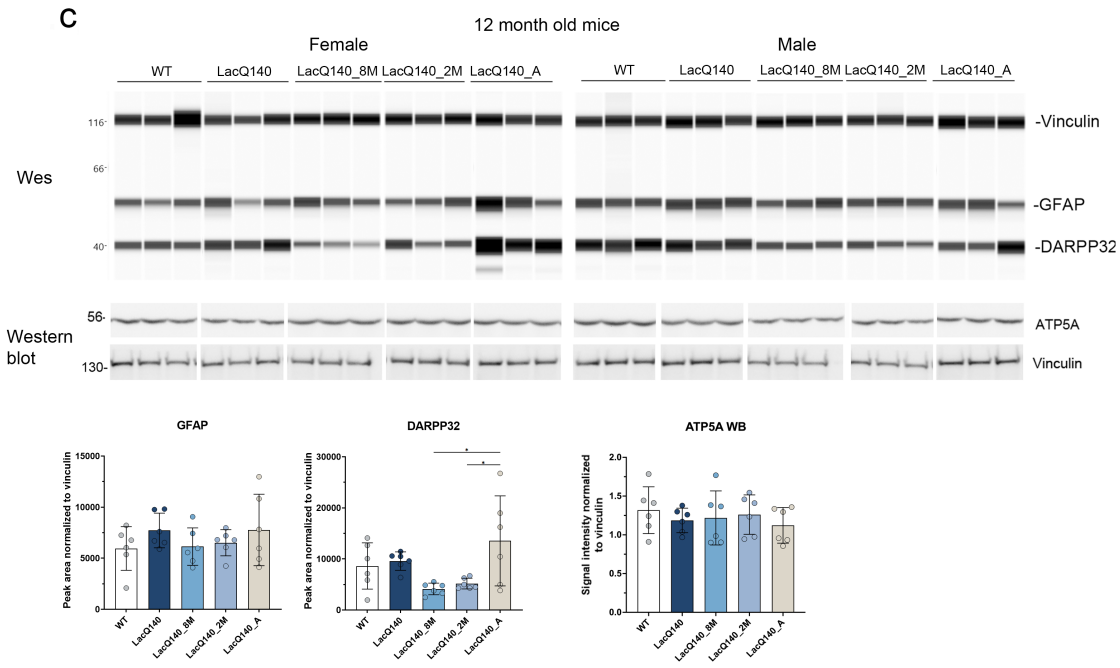

Supplementary Figure 6. Duration of m*Htt* lowering in 6, 9 and 12 months old LacQ140 mice has minimal effects on levels of GFAP, DARPP32 and ATP5A.

GFAP and DARPP32 levels were analyzed by capillary immunoassay on equal amounts of protein (0.6 µg) and ATP5A levels were analyzed by western blot on equal amounts of protein (10 µg). In 6-month-old mice, peak area analysis shows no significant change in GFAP or DARPP32 levels (**a**) and total pixel intensity quantification shows no changes in ATP5A levels in any of the LacQ140 or WT mice (**a**). Peak area analysis in 9-month-old mice shows a significant decrease in DARPP32 levels in all LacQ140 mice compared to WT mice (**b**, **p<0.01, ***p<0.001, One-way ANOVA with Tukey's multiple comparison test, n=6). Total pixel intensity quantification shows ATP5A levels are significantly higher in LacQ140_2M and LacQ140_A mice compared to WT or LacQ140 mice (**b,** *p<0.05, **p<0.01, ***p<0.001, One-way ANOVA with Tukey's multiple comparison test, n=6). Peak area analysis in 12-month-old mice shows no significant change in GFAP levels in LacQ140 or WT mice. There is a significant decrease in DARPP32 levels in LacQ140_8M and LacQ140_2M compared to LacQ140_A mice (**c,** *p<0.05, One-way ANOVA with Tukey's multiple comparison test, n=6). Total pixel intensity quantification for each band using ImageJ software shows no changes in ATP5A levels in any of the LacQ140 or WT mice.

Supplementary Figure 7

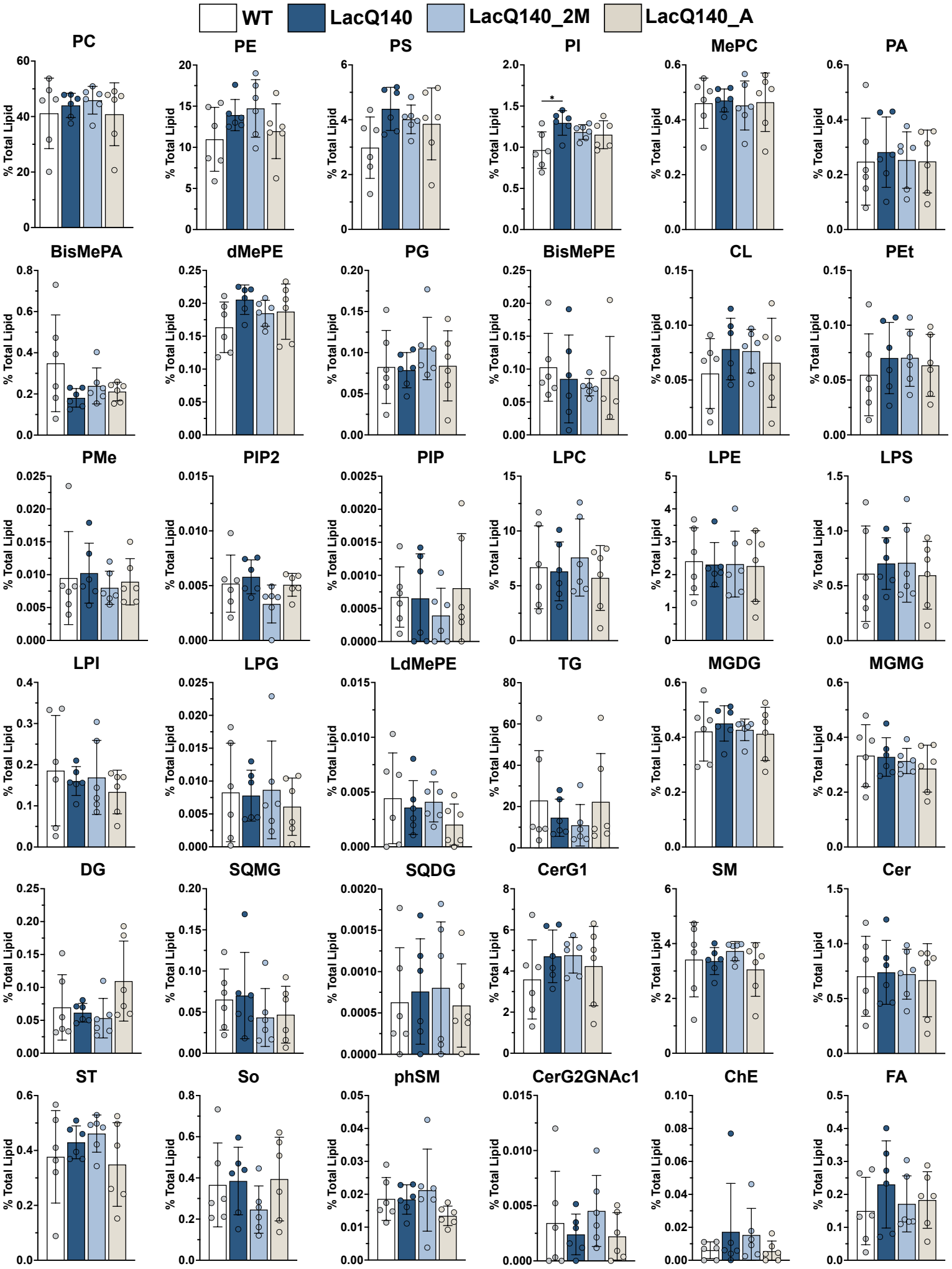

Supplementary Figure 7. Lipid subclasses detected in caudate putamen of 6-month-old mice.
Lipids were extracted and analyzed by LC-MS/MS. Graphs show relative intensities for indicated lipid subclasses expressed as a percent of total lipid intensity per sample for each genotype or treatment group. Plotted values represent summed lipid subclass intensity standardized to total amount of lipid detected in the same sample. Bar charts underneath individual points represent group means and error bars are ± standard deviation. PI was significantly increased in striatum of 6-month-old LacQ140 mice compared to WT mice (One-way ANOVA with Tukey's multiple comparisons test, $F(3, 20) = 4.176$, * $P=0.0189$, $n=6$). This increase is not significant when p-values are adjusted for multiple testing using the Benjamini, Krieger and Yekutieli procedure with a false discovery rate of 5%, ($q = 0.7144$, N=36 subclasses). No changes between groups were found in any other subclasses.

Abbreviations:
Glycerophospholipids: PC = phosphatidylcholine, PE = phosphatidylethanolamine, PS = phosphatidylserine, PI = phosphatidylinositol, MePC = methylphosphocholine, PA = phosphatidic acid, BisMePA = bis-methyl phosphatidic acid, dMePE = dimethyl phosphatidylethanolamine, PG = phosphatidylgylcerol, BisMePE = bis-methyl phosphatidyl ethanolamine, CL = cardiolipin, PEt = phosphatidylethanol, PMe = phosphatidylmethanol, PIP2 = phosphatidylinositol-bisphosphate, PIP = phosphatidylinositol-monophosphate, LPC = lysophosphatidylcholine, LPE = lysophosphatidylethanolamine, LPS = lysophosphatidylserine, LPI = lysophosphatidylinositol LPG = lysophosphosphatidylgylcerol, LdMePE = lysodimethyl phosphatidyl ethanolamine
Glycerolipids: TG = triacylglycerol, MGDG = monogalactosyldiacylglycerol, MGMG = monogalactosylmonoacylglycerol, DG = diacylglycerol, SQMG = sulfoquinovosylmonoacylglycerol, SQDG = sulfoquinovosyldiacylglycerol,
Sphingolipids: CerG1 = simple Glc series, SM = sphingomyelin, Cer = ceramide, ST = sulfatide, So = sphingosine, phSM = sphingomyelin phytosphingosine, CerG2GNAc1 = Simple Glc series
Sterol lipids: ChE = cholesterol ester
Fatty acyls: FA = fatty acid

Supplementary Figure 8

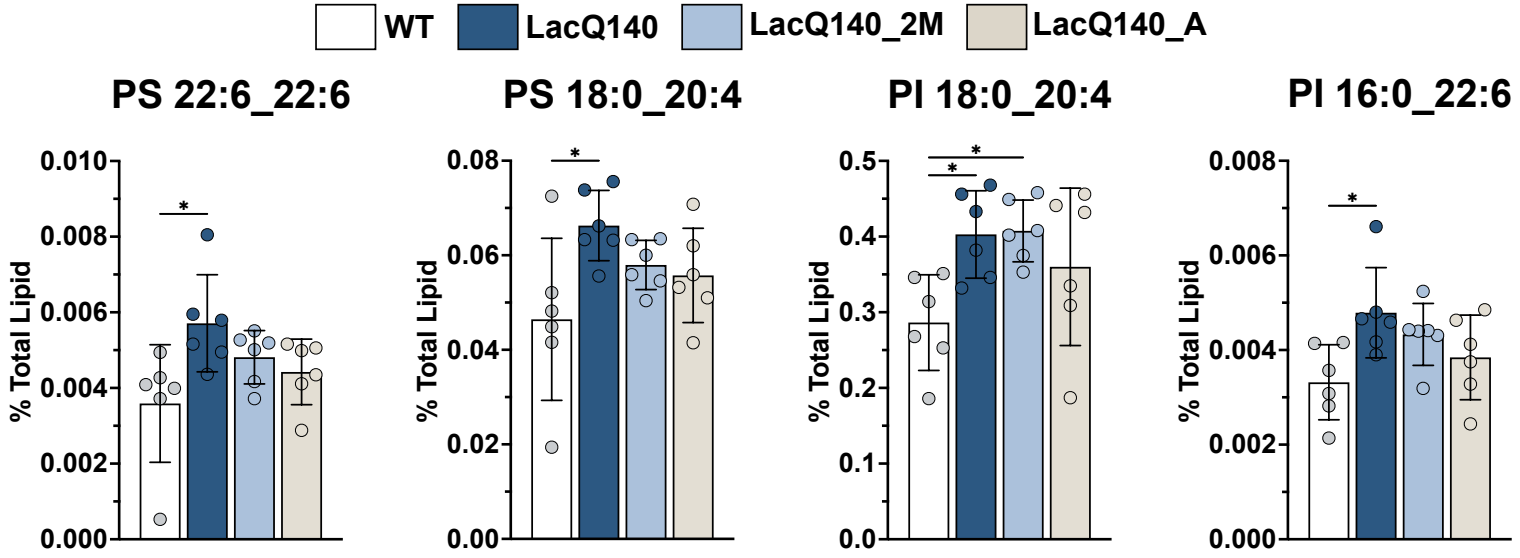

Supplementary Figure 8. Individual lipid species significantly different between 6-month-old LacQ140 and WT mice.

Lipids were extracted and analyzed by LC-MS/MS. Graphs show relative intensities for indicated lipid species expressed as a percent of total lipid intensity per sample for each genotype or treatment group. Plotted values represent individual lipid species intensity standardized to total amount of lipid detected in the same sample. Bar charts underneath individual points represent group means and error bars are ± standard deviation. One-way analysis of variance (ANOVA) was used to evaluate differences in lipid species intensity between groups and Tukey's multiple comparisons test was used for post-hoc pairwise comparisons (n=6 mice per group, *$p < 0.05$, Tukey's multiple comparisons test). To correct for multiple testing over all lipids analyzed, the Benjamini, Krieger and Yekutieli procedure was used with a false discovery rate of 5% (N=800 lipid species), FDR adjusted p-values are reported as q values. No individual species found to be different by one-way ANOVA were significant following correction of p-values. PS 22:6_22:6: $F(3, 20) = 3.812$,*P=0.0260, q=1, ns; PS 18:0_20:4: $F(3, 20) = 3.349$, *P=0.0396, q=1, ns; PI 18:0_20:4: $F(3, 20) = 3.812$, *P=0.0260, q=1, ns; PI 16:0_22:6: $F(3, 20) = 3.466$, *P=0.0356, q=1, ns. Abbreviations: PI = phosphatidylinositol, PS = phosphatidylserine

Supplementary Figure 9

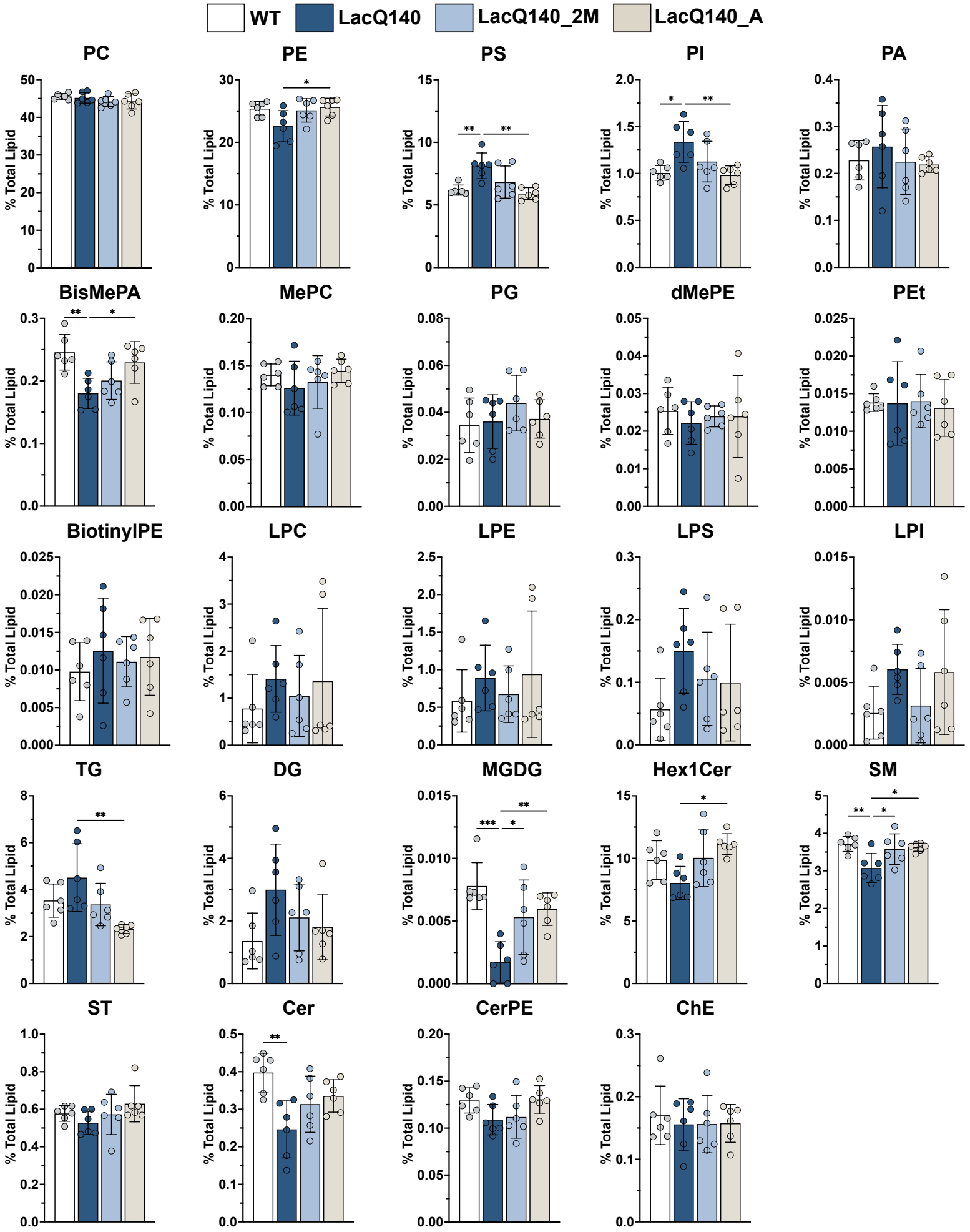

Supplementary Figure 9. Lipid subclasses detected in caudate putamen of 9-month-old mice.
Lipids were extracted and analyzed by LC-MS/MS. Graphs show relative intensities for indicated lipid subclasses expressed as a percent of total lipid intensity per sample for each genotype or treatment group. Plotted values represent summed lipid subclass intensity standardized to total amount of lipid detected in the same sample. Bar charts underneath individual points represent group means and error bars are ± standard deviation. One-way analysis of variance (ANOVA) was used to evaluate differences in lipid subclass intensity between groups and Tukey's multiple comparisons test was used for post-hoc pairwise comparisons (n=6 mice per group, *p < 0.05, **p < 0.01, Tukey's multiple comparisons test). To correct for multiple testing the Benjamini, Krieger and Yekutieli procedure was used with a false discovery rate of 5% (N=24 subclasses) and FDR adjusted p-values are reported as q values. PS: F(3, 20) = 7.601, **P=0.0014, q=0.0125, PI: F(3, 20) = 5.707, **P=0.0054, q=0.0168, BisMePA: F(3, 20) = 6.086, **P=0.0041,q=0.0168, SM: F(3, 20) = 5.465, **P=0.0066, q=0.0168, Cer: F(3, 20) = 5.883, **P=0.0048, q=0.0168, MGDG: F(3, 20) = 9.350 , ***P=0.0005, q=0.0089. PE, TG and Hex1Cer were unchanged between LacQ140 and WT groups but had changes among other treatment groups (PE: F(3, 20) = 3.717, *P=0.0284, q=0.0563, ns, TG: F(3, 20) = 5.637, **P=0.0057, q=0.0168, Hex1Cer: F(3, 20) = 3.891, *P=0.0243, q=0.054, ns).

Abbreviations:
Glycerophospholipids: PC = phosphatidylcholine, PE = phosphatidylethanolamine, PS = phosphatidylserine, PI = phosphatidylinositol, PA = phosphatidic acid, BisMePA = bis-methyl phosphatidic acid, MePC = methylphosphocholine, PG = phosphatidylgylcerol, dMePE = dimethyl phosphatidylethanolamine, PEt = phosphatidylethanol, BiotinylPE = biotinyl-phosphoethanolamine, LPC = lysophosphatidylcholine, LPE = lysophosphatidylethanolamine, LPS = lysophosphatidylserine, LPI = lysophosphatidylinositol
Glycerolipids: TG = triacylglycerol, DG = diacylglycerol, MGDG = monogalactosyldiacylglycerol
Sphingolipids: Hex1Cer = monohexosylceramide, SM = sphingomyelin, ST = sulfatide, Cer = ceramide, CerPE = ceramide phosphorylethanolamine
Sterol lipids: ChE = cholesterol ester

Supplementary Figure 10

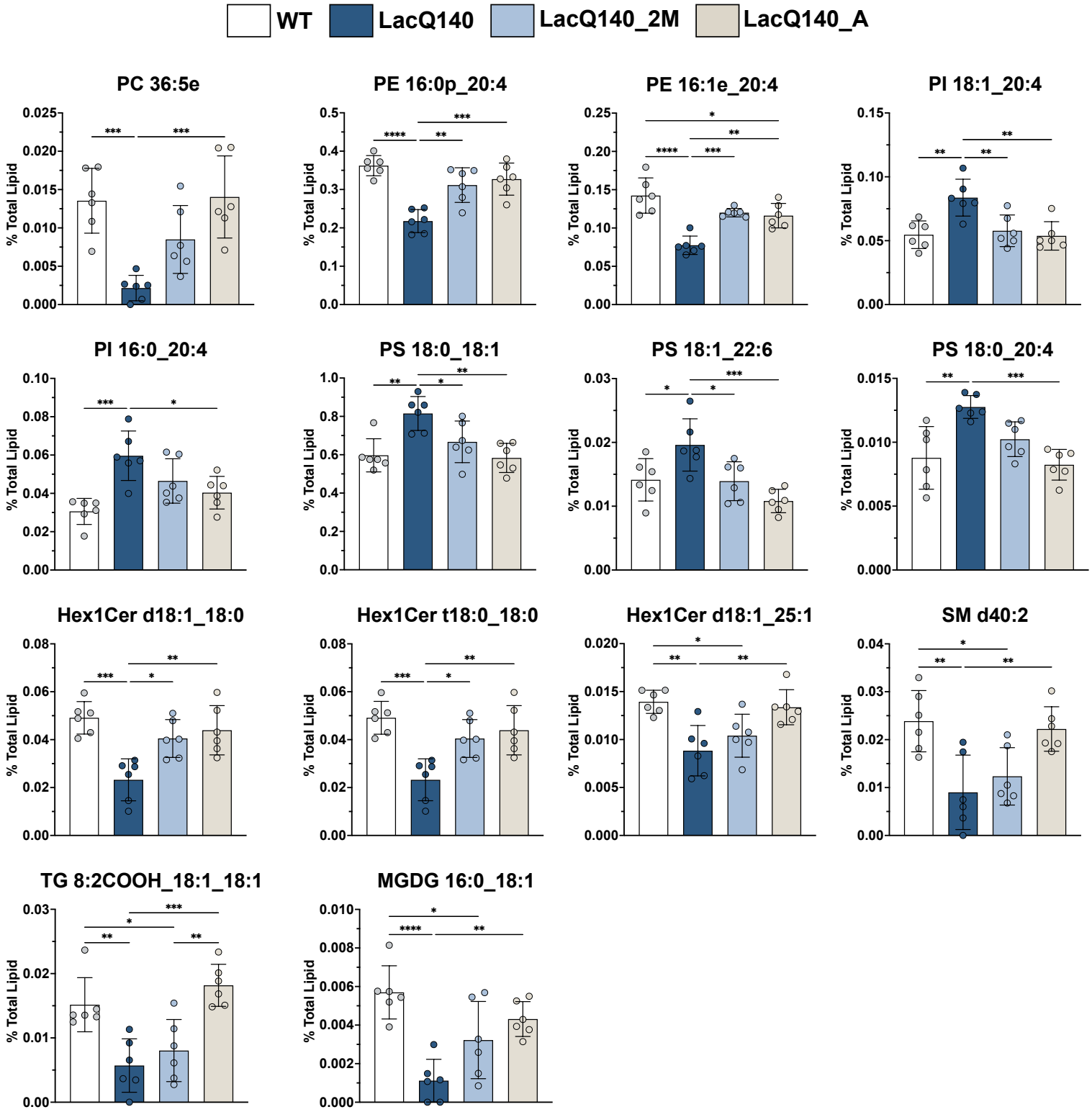

Supplementary Figure 10. Individual lipid species significantly changed between 9-month-old LacQ140 and WT mice.

Lipids were extracted and analyzed by LC-MS/MS. Graphs show relative intensities for indicated lipid species expressed as a percent of total lipid intensity per sample for each genotype or treatment group. Plotted values represent individual lipid species intensity standardized to total amount of lipid detected in the same sample. Bar charts underneath individual points represent group means and error bars are ± standard deviation. One-way analysis of variance (ANOVA) was used to evaluate differences in lipid species intensity between groups and Tukey's multiple comparisons test was used for post-hoc pairwise comparisons (n=6 mice per group, *p < 0.05, **p < 0.01, ***p < 0.001, ****p < 0.0001, Tukey's multiple comparisons test). To correct for multiple testing over all lipids analyzed, the Benjamini, Krieger and Yekutieli procedure was used with a false discovery rate of 5% (N=632 lipid species), FDR adjusted p-values are reported as q values. PC 36:5e: F(3, 20) = 10.68, ***P=0.0002, q=0.02, PE 16:1e_20:4: F(3, 20) = 18.14, ****P<0.0001, q=0.003, PE 16:0p_20:4: F(3, 20) = 16.97, ****P<0.0001, q=0.003, PI 18:1_20:4: F(3, 20) = 8.086, **P=0.0010, q=0.041, PI 16:0_20:4: F(3, 20) = 8.449, ***P=0.0008, q=0.039, PS 18:0_18:1: F(3, 20) = 8.226, ***P=0.0009, q=0.041, PS 18:1_22:6: F(3, 20) = 7.916, **P=0.0011, q=0.042, PS 18:0_20:4: F(3, 20) = 9.739, ***P=0.0004, q=0.023, Hex1Cer d18:1_18:0: F(3, 20) = 10.37, ***P=0.0002, q=0.02, Hex1Cer t18:0_18:0: F(3, 20) = 10.35, ***P=0.0003, q=0.02, Hex1Cer d18:1_25:1: F(3, 20) = 8.440, ***P=0.0008, q=0.039, SM d40:2: F(3, 20) = 8.052, **P=0.0010, q=0.041, TG 8:2COOH_18:1_18:1: F(3, 20) = 11.98, ***P=0.0001, q=0.017, MGDG 16:0_18:1: F(3, 20) = 11.28, ***P=0.0002, q=0.019.

Abbreviations:

Glycerophospholipids: PC = phosphatidylcholine, PE = phosphatidylethanolamine, PI = phosphatidylinositol, PS = phosphatidylserine

Sphingolipids: Hex1Cer = monohexosylceramide, SM = sphingomyelin

Glycerolipids: MGDG = monogalactosyldiacylglycerol, TG = triacylglycerol

Supplementary Figure 11

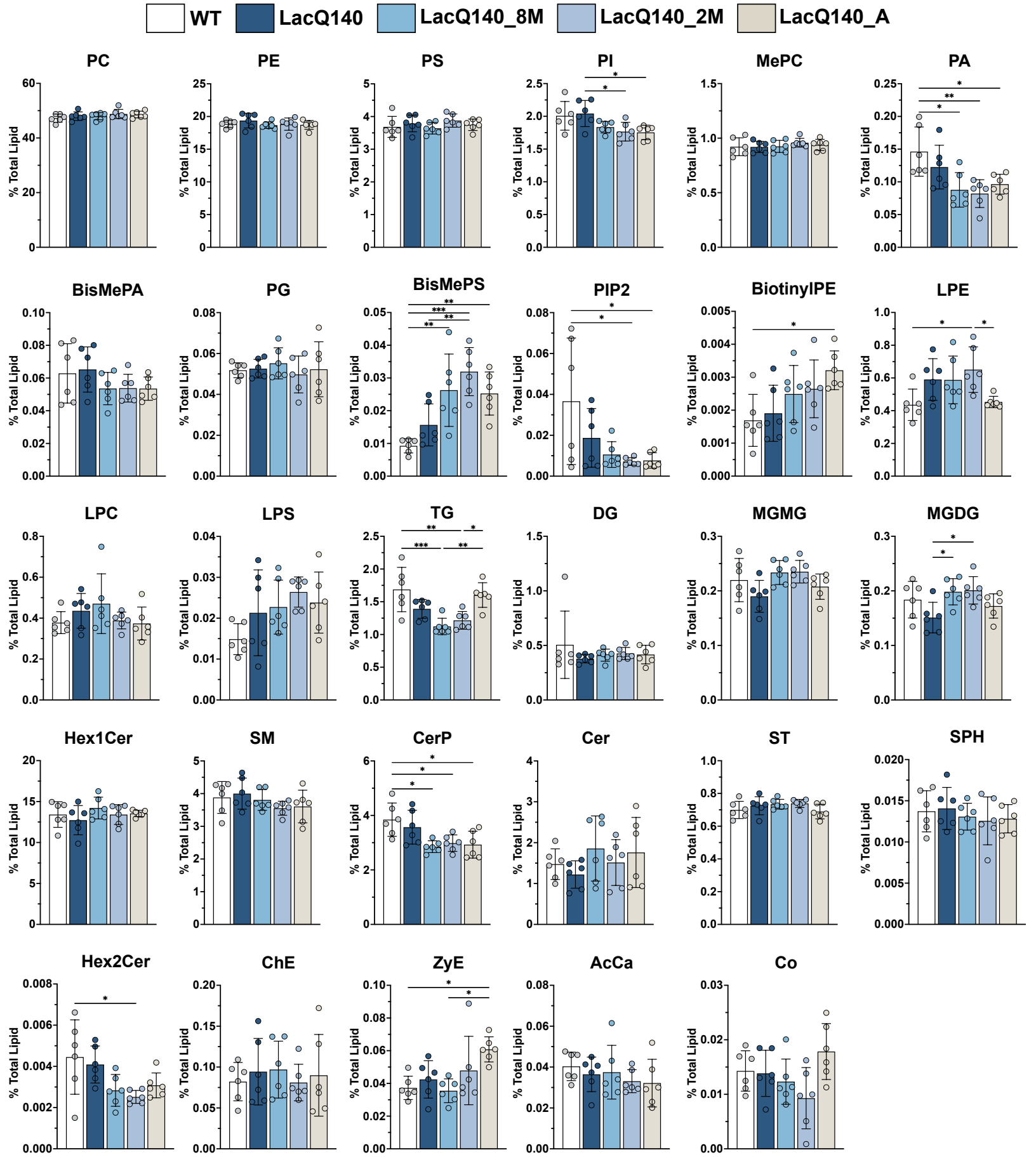

Supplementary Figure 11. Lipid subclasses detected in caudate putamen of 12-month-old mice.
Lipids were extracted and analyzed by LC-MS/MS. Graphs show relative intensities for indicated lipid subclasses expressed as a percent of total lipid intensity per sample for each genotype or treatment group. Plotted values represent summed lipid subclass intensity standardized to total amount of lipid detected in the same sample. Bar charts underneath individual points represent group means and error bars are ± standard deviation. One-way analysis of variance (ANOVA) was used to evaluate differences in lipid subclass intensity between groups and Tukey's multiple comparisons test was used for post-hoc pairwise comparisons (n=6 mice per group, *p < 0.05, **p < 0.01, ***p < 0.001, Tukey's multiple comparisons test). To correct for multiple testing the Benjamini, Krieger and Yekutieli procedure was used with a false discovery rate of 5% (N=29 subclasses), FDR adjusted p-values are reported as q values. PI: F(4, 25) = 4.316, **P=0.0086, q=0.0338, PA: F(4, 25) = 5.537, **P=0.0025, q=0.0184, BisMePS: F(4, 25) = 9.308, ****P<0.0001, q=0.0022, PIP2: F(4, 25) = 3.743, *P=0.0161, q=0.0394, BiotinylPE: F(4, 25) = 3.446, *P=0.0225, q=0.0451, LPE: F(4, 25) = 3.957, *P=0.0127, q=0.035. TG: F(4, 25) = 8.593, ***P=0.0002, q=0.0022, MGMG: F(4, 25) = 2.765, *P=0.0497, q=0.0887, ns, MGDG: F(4, 25) = 3.491, *P=0.0214, q=0.0451. CerP: F(4, 25) = 5.185, **P=0.0035, q=0.0193, Hex2Cer: F(4, 25) = 4.076, *P=0.0112, q=0.035, ZyE: F(4, 25) = 4.256, **P=0.0092, q= 0.0338.

Abbreviations:
Glycerophospholipids: PC = phosphatidylcholine, PE = phosphatidylethanolamine, PS = phosphatidylserine, PI = phosphatidylinositol, MePC = methylphosphocholine, PA = phosphatidic acid, BisMePA = bis-methyl phosphatidic acid, PG = phosphatidylgylcerol, BisMePS = bis-methylphosphatidylserine, PIP2 = phosphatidylinositol-bisphosphate, BiotinylPE = biotinyl-phosphoethanolamine, LPE = lysophosphatidylethanolamine, LPC = lysophosphatidylcholine, LPS = lysophosphatidylserine
Glycerolipids: TG = triacylglycerol, DG = diacylglycerol, MGMG = monogalactosylmonoacylglycerol, MGDG = monogalactosyldiacylglycerol
Sphingolipids: Hex1Cer = monohexosylceramide, SM = sphingomyelin, CerP = ceramide phosphate, Cer = ceramide, ST = sulfatide, SPH = sphingoid base, Hex2Cer = dihexosylceramide
Sterol lipids: ChE = cholesterol ester, ZyE = zymosterol
Fatty acyls: AcCa = acyl carnitine
Prenol lipids: Co = coenzyme

Supplementary Figure 12

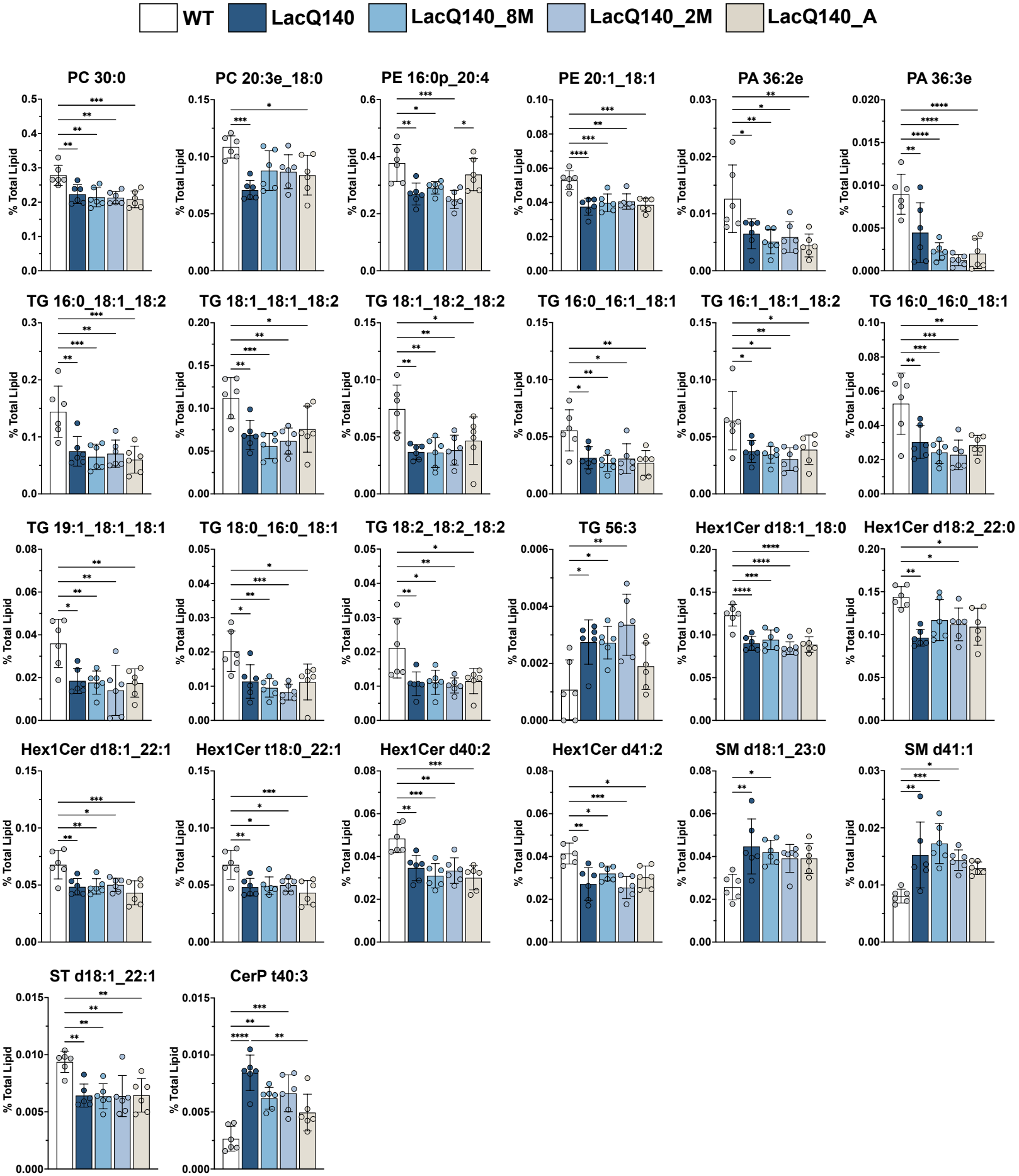

Supplementary Figure 12. Individual lipid species significantly changed between 12-month-old LacQ140 and WT mice.

Lipids were extracted and analyzed by LC-MS/MS. Graphs show relative intensities for indicated lipid species expressed as a percent of total lipid intensity per sample for each genotype or treatment group. Plotted values represent individual lipid species intensity standardized to total amount of lipid detected in the same sample. Bar charts underneath individual points represent group means and error bars are ± standard deviation. One-way analysis of variance (ANOVA) was used to evaluate differences in lipid species intensity between groups and Tukey's multiple comparisons test was used for post-hoc pairwise comparisons (n=6 mice per group, *p < 0.05, **p < 0.01, ***p < 0.001, ****p < 0.0001, Tukey's multiple comparisons test). To correct for multiple testing over all lipids analyzed, the Benjamini, Krieger and Yekutieli procedure was used with a false discovery rate of 5% (N=735 lipid species), FDR adjusted p-values are reported as q values. PC 30:0: F(4, 25) = 7.601, ***P=0.0004, q=0.0132, PC 20:3e_18:0: F(4, 25) = 5.567, **P=0.0024, q=0.0327, PE 16:0p_20:4: F(4, 25) = 7.879, ***P=0.0003, q=0.0114, PE 20:1_18:1: F(4, 25) = 10.36, ****P<0.0001, q=0.0038, PA 36:2e: F(4, 25) = 5.630, **P=0.0023, q=0.0327, PA 36:3e: F(4, 25) = 13.27, ****P<0.0001, q=0.0007, TG 16:0_18:1_18:2: F(4, 25) = 8.357, ***P=0.0002, q=0.0094, TG 18:1_18:1_18:2: F(4, 25) = 7.113, ***P=0.0006, q=0.0182, TG 18:1_18:2_18:2: F(4, 25) = 6.249, **P=0.0013, q=0.0272, TG 16:0_16:1_18:1: F(4, 25) = 5.794, **P=0.0019, q=0.0306, TG 16:1_18:1_18:2: F(4, 25) = 4.983, **P=0.0043, q=0.0438, TG 16:0_16:0_18:1: F(4, 25) = 7.833, ***P=0.0003, q=0.0114, TG 19:1_18:1_18:1: F(4, 25) = 6.060, **P=0.0015, q=0.0272, TG 18:0_16:0_18:1: F(4, 25) = 6.726, ***P=0.0008, q=0.0217, TG 18:2_18:2_18:2: F(4, 25) = 5.352, **P=0.0030, q=0.0345, TG 56:3: F(4, 25) = 6.109, **P=0.0014, q=0.0272, Hex1Cer d18:1_18:0: F(4, 25) = 14.49, ****P<0.0001, q=0.0005, Hex1Cer d18:2_22:0: F(4, 25) = 5.594, **P=0.0023, q=0.0327, Hex1Cer d18:1_22:1: F(4, 25) = 6.637, ***P=0.0009, q=0.0219, Hex1Cer t18:0_22:1: F(4, 25) = 6.181, **P=0.0013, q=0.0272, Hex1Cer d40:2: F(4, 25) = 9.257, ****P<0.0001, q=0.0058, Hex1Cer d41:2: F(4, 25) = 7.880, ***P=0.0003, q=0.0114, SM d18:1_23:0: F (4, 25) = 5.007, **P=0.0042, q=0.0438, SM d41:1: F(4, 25) = 6.980, ***P=0.0006, q=0.0197, ST d18:1_22:1: F (4, 25) = 6.263, **P=0.0012, q=0.0272, CerP t40:3: F (4, 25) = 14.26, ****P<0.0001, q=0.0005.

Abbreviations:

Glycerophospholipids: PC = phosphatidylcholine, PE = phosphatidylethanolamine, PA = phosphatidic acid

Glycerolipids: TG = triacylglycerol

Sphingolipids: Hex1Cer = monohexosylceramide, SM = sphingomyelin, ST = sulfatide, CerP = ceramide phosphate

Supplementary Figure 13

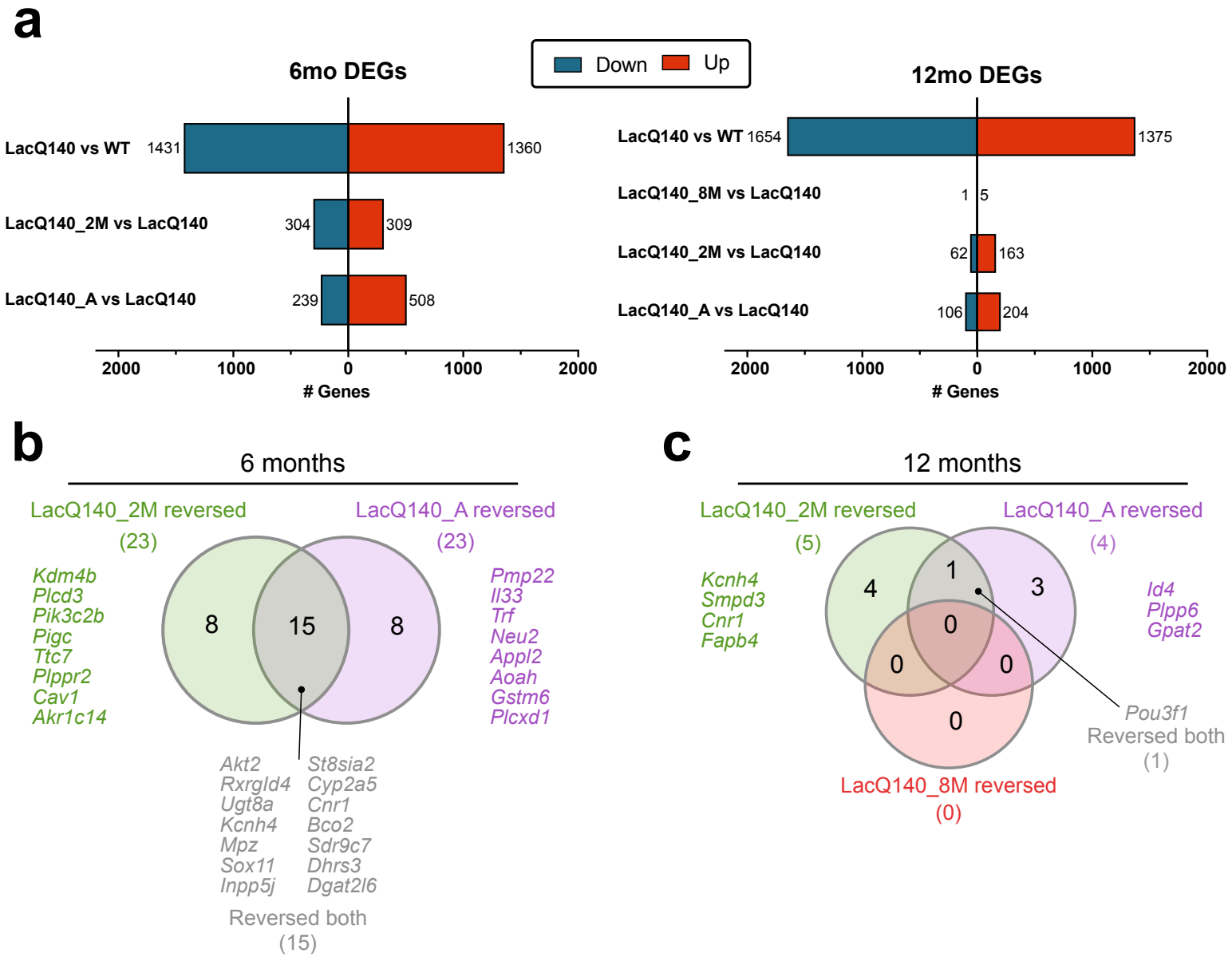

Supplementary Figure 13. DEGs, reversed genes in 6- and 12-month-old LacQ140 mice

(a) Bar chart shows number of differentially expressed genes (DEGs) at 6-months (left) and 12-months (right). Total number of DEGs in LacQ140 mice (upregulated: red and downregulated: blue) are shown in the top bar; lower bars show number of DEGs in mice with mHtt repression (LacQ140_8M, LacQ140_2M, LacQ140_A) compared to LacQ140 mice (i.e., genes "reversed" with m*Htt* repression). **(b)** Venn diagram depicts genes "reversed" at 6-months for each respective m*Htt* repression group as shown in **Figure 6c**. **(c)** Venn diagram depicts genes "reversed" at 12-months for each respective m*Htt* repression group as shown in **Figure 6f**.